ENGINEERING AND ARCHITECTURAL SCIENCES

Theory, Current Researches and New Trends/2021

Editor

Assoc. Prof. Dr. Meruyert KAYGUSUZ

ISBN: 978-9940-46-069-3

IVPE DOO

Cetinje 2021

ENGINEERING AND ARCHITECTURAL SCIENCES

Theory, Current Researches and New Trends/2021

Editor

Assoc. Prof. Dr. Meruyert KAYGUSUZ

Editor
Assoc. Prof. Dr. Meruyert KAYGUSUZ

First Edition •© May 2021 /Cetinje-Montenegro

ISBN • 978-9940-46-069-3

© copyright All Rights Reserved

web: www.ivpe.me

Tel. +382 41 234 709

e-mail: office@ivpe.me

Cetinje, Montenegro

PREFACE

Science and technology based on scientific research is developing day by day and affects our lives considerably. Thanks to research, many innovative ideas and products have been developed. The world of science is finding solutions to many problems through research. All countries and economies today are placing more emphasis on research in order to improve quality and provide a competitive advantage in every field.

Academic studies from different disciplines in the fields of engineering and architecture are presented in this book. I believe that these studies shared with the scientific world will constitute an important resource for students, researchers, academics and people from the sector, and will be useful for future research.

I would like to thank all the authors who gave support with their studies, shared their valuable knowledge and contributed with their research in the relevant discipline. I also wish to thank IVPE Publishing House, who created this international book for the dissemination of new information.

CONTENTS

CHAPTER I

Burak GÖKSU & Süleyman Aykut KORKMAZ & Emrah ERGİNER

SHIP WIND RESISTANCE PREDICTION: A CASE-BASED APPROACH **1**

CHAPTER II

Ceyda BİLGİÇ & Şafak BİLGİÇ

VARIOUS INDUSTRIAL APPLICATIONS OF SELF-CLEANING AND MULTIFUNCTIONAL SURFACES ……**23**

CHAPTER III

Ceyda BİLGİÇ & Şafak BİLGİÇ

THERMAL AND STRUCTURAL ANALYSIS OF GEOPOLYMERS DERIVED FROM INDUSTRIAL WASTE MATERIALS ….……**38**

CHAPTER IV

Gabriella FEDERER-KOVACS & Hani Al KHALAF & Nagham Al-Haj MOHAMMED & Tolga DEPCI

REASONS AND RESOLUTIONS OF TRAPPED ANNULAR PRESSURE ……**56**

CHAPTER V

F. Demet AYKAL & Meltem ERBAŞ ÖZİL

THE EVALUATION ON WATER STRUCTURE IN MARDIN HISTORICAL MADRASAHS ……**79**

CHAPTER VI

Gülferah ÇORAPÇIOĞLU & Sabit OYMAEL

SUSTAINABLE URBAN RENEWAL PROCESS AND ASBESTOS FACTOR …...……**96**

CHAPTER VII

Keziban CALIK & Coskun FIRAT

A COMPREHENSIVE OPTICAL LOSS ANALYSIS OF A LINEAR FRESNEL REFLECTOR-PHOTOVOLTAIC HYBRID SYSTEM WITH COMPUTER AIDED DESIGN ...……109

CHAPTER VIII

Özgür KARADAŞ & Binnur KAPTAN & İsmail YILMAZ

AROMATIC COMPOUNDS OF PROTEOLYSIS AND LIPOLYSIS ORIGIN OCCURRING DURING FERMENTATION IN MEAT PRODUCTS .....……129

CHAPTER IX

Seher GÜZELÇOBAN MAYUK & Elif ÖZER YÜKSEL & N. Özge ESENER & Gizem ASLAN & Merve ÖZDOĞAN & Çetin SÜALP

BUILDING SCIENCE I EXPERIENCES AS AN APPLIED COURSE ON EMERGENCY REMOTE TEACHING (ERT) OF ARCHITECTURE ……...……147

CHAPTER X

Sibel BAYAR & Ercan AKAN

RISK ANALYSIS IN MARITIME LOGISTICS OPERATION PROCESS BY APPLYING DEMATEL METHOD .....……160

REFEREES

Prof. Dr. Rıdvan Karapınar, Burdur Mehmet Akif Ersoy University

Assoc. Prof. Dr. Ahmet Talat İnan, Marmara University

Assoc. Prof. Dr. Fazilet Koçyiğit, Amasya University

Assoc. Prof. Dr. Meruyert Kaygusuz, Pamukkale University

Assoc. Prof. Dr. Berrin Şahin Diri, Mimar Sinan Güzel Sanatlar University

CHAPTER I

SHIP WIND RESISTANCE PREDICTION: A CASE-BASED APPROACH

Burak GÖKSU

(Ph. D. Candidate); Dokuz Eylul University, Izmir, Turkey, e-mail: burak.goksu@deu.edu.tr
Orcid No: 0000-0002-6152-0208

Süleyman Aykut KORKMAZ

(Ph. D. Candidate); Dokuz Eylul University, Izmir, Turkey, e-mail: aykut.korkmaz@deu.edu.tr
Orcid No: 0000-0001-5972-6971

K. Emrah ERGİNER

(Asst. Prof. Dr.); Dokuz Eylul University, Izmir, Turkey, e-mail: emrah.erginer@deu.edu.tr
Orcid No: 0000-0002-2227-3486

1. Introduction

The naval architects, shipyards, and ship designers increase the ships' design performance by using the derivatives that the customer requests have traditionally determined. All these concerns shall comply with the environmental protection regulations, which stringent highly today (Tupper, 2013). This process's main idea is to reveal the product that will bring together customer demand and international regulatory rules. In the sea trials performed after launching the ships, the most efficient fuel consumption is expected at the requested service speed. As an excellent musical performance observed where all the instruments are played in harmony in a harmonious symphony, the hull and upper structure design's compatibility plays a significant role according to ship resistance. The more appropriate ship design is derived from a design spiral vital for commercial ships to have a minimum fluid resistance while visually pleasing and considering all the related marine/industrial rules and regulations.

In the fluid environment consisting of air and water, the most significant resistance force that prevents a ship's navigation is caused by contact with seawater (Larsson and Leif, 1990). Although the air density is less than water, there is a resistance affecting a ship's superstructure, dragged by air. Generally, air resistance is mostly calculated using empirical equations rather than fluid dynamics calculations (Van He et al., 2016). Compared to the total resistance value, the low air resistance value can be neglected to prevent time loss in both towing tank tests and computational fluid dynamics (CFD) calculations. However, for ships with large superstructures such as container ships, LNG (liquefied natural gas) carriers, and car-ferries, wind can affect the air resistance acting on the vessel and cause trimming and heeling (Seok and Park, 2020).

Among the resistance components of a ship in a real environment, the wave and air resistance are the most important and the two largest added resistance components in value. Therefore, the prediction of the added resistance and ship speed loss in real environmental conditions is necessary to evaluate the effect of operational requirements on ship performance (Feng et al., 2010).

As Seok and Park experienced calculating a container ship's air resistance with and without superstructure concerning the issue mentioned above. Therefore, numerical simulations were performed to compare the total resistance, trim, and sinking of an 8000 TEU container ship. The simulation conditions were verified by comparison with the study results of the KCS (KRISO Container Ship) hull form under five different speed conditions (Froude number (Fr) 0.165, 0.192, 0.219, 0.247, and 0.274) in the model scale. Under the specified speed conditions, air resistance was calculated to vary between 1% and 5% of the ship's resistance. Where the Fr is 0.192 or less, the air resistance is relatively low, indicating that the results have been verified (Seok and Park, 2020).

As Kim et al. proposed a reliable methodology for estimating the loss of speed of the S175 container ship in certain sea conditions of wind and waves. A verification study was conducted by comparing simulations of various wave conditions with existing experimental data. After the verification study in regular waves, calm water resistance is calculated, and the ship speed loss is estimated using the developed methodology. Considering the relevant wave parameters and wind speed corresponding to the Beaufort scale, added resistance and results from wind and irregular waves were compared with other researchers' simulation results. Finally, the effect of variance in ship speed and ship speed loss has been investigated (Kim et al., 2017).

Shigunov exerted that "*The added power software combines added resistance and drift forces and moments in irregular waves with wind forces and moments, calm-water maneuvering forces and moments, rudder and propeller forces, and propulsion and engine model and provides associated resistance and power as well as changes in ship propulsion in waves*" (Shigunov, 2018).

A new procedure was presented to predict speed reduction and fuel consumption of a ship at real sea conditions. While wind resistance, fouling effect, and other resistance components are ignored due to their relatively small and temporary nature, the additional resistance from waves is taken into account in Feng et al. due to the predominance (Feng et al., 2010).

The importance of wind resistance in land vehicles can be seen from the scientific and industrial applications. However, considering the forces that create resistance against a marine vehicle's navigation, the effect of seawater is relatively high compared to air. Thus, the air resistance is either neglected or considered to be at a specific rate according to the water's resistance. However, the significance of wind resistance increases in ships with higher superstructures than other ships, such as the ferry examined in this study. Besides, the predominance of the west wind in the car-ferry's voyage zone and the fact that this wind comes at a vertical angle to the side of the ship during the round trip voyage emphasizes this study's necessity.

Similar studies have been conducted in the literature; however, the review within the scope we examine and observe has a few types of research about the wind resistance of a car-ferry. When the ships' added resistance was taken into account, and the results of the studies examined above were assessed, it was observed that the additional power required for the air resistance was not negligible compared to the calm water power demand. On the other hand, if the main engine cannot supply further power, the ship navigation will be slower than the calm water state. When similar studies on this subject were reviewed, it was concluded that the rest of the study should include ship resistance components and their calculation methods. Afterward, the geometrical properties and the towing tank test results of the case car-ferry are presented. Subsequently, the ferry's voyage line has been introduced, and the problem definition has been done. Air resistance values of the departure and arrival voyage have been predicted and the results have been tabulated separately. Finally, the result values have been discussed according to the importance of air drag force in total resistance has been emphasized, especially for ships with large superstructures.

2. Aim and scope of the work

In this study, added air resistance calculations were conducted considering the Izmir Bay wind data's annual average. However, the case ship's hull is a displacement type double-ended ferry, and the Holtrop-Mennen method is utilized for a general overview to derive the reference resistance value. This prediction method is the most commonly used one for the conventional cargo ship, a displacement type of hull in the shipbuilding preliminary design process. Nowadays, the CFD software usage, which enables fluid dynamics calculations to be conducted with advanced computers, has generated rapid and cost-effective results. The bare hull resistance values used in this study are directly taken from the towing tank experiments held at the ITU Ata Nutku laboratory for the ferry's hull structure. These calculations have been conducted according to the report (Bal et al., 2014). At the towing tank tests, the absence of the superstructure of the car-ferry, the exposure of the beam sides of the ship to the wind at real conditions; considering the annual average wind data in the service area of the ferry, reveals the necessity of this study. Generally, the total ship resistance is being calculated without the effect of the superstructure. Indeed, the calculations have been done with the ship's superstructure, which is closer to the real conditions as the ferry will be affected by the real average wind condition for a round trip voyage. In this way, more precise fuel consumption will be calculated, informing the ship operator much better. Besides, using a ship with a superstructure in a towing tank test will be insufficient to calculate the wind resistance. Since the car-ferry structure's lateral area is considerably large and the wind blowing from the beam side requires additional wind resistance to be measured independently. This study has some constraints as Izmir Bay's sea conditions are assumed as calm water with no current, and the car-ferry has no periodic motion like roll and sway due to the wind condition.

3. Ship resistance and components

Ship propulsion systems are used to provide the voyage at the desired service speed by transferring the force to the hull in the opposite direction of external drag forces (Lewis, 1989). One of the main tasks of a naval architect is to be able to design the appropriate propulsion system by estimating the resistance of a ship, such as stability control, strength calculation, and maneuverability tests. Most of the resistance analyses are performed to measure the drag force required for the vessel to navigate in calm water. The resistance force in the most general form consists of viscous resistance and wave resistance (Molland et al., 2011). Viscous

resistance is the resistive component that represents the energy losses caused by the viscosity of the water. Wave resistance means the lost energy that forms the wave system that surrounds the ship. However, in addition to these two components under restricted calculation conditions: wave breaking resistance, appendage resistance, roughness resistance, air and wind resistance, steering resistance such components effect preventing the voyage of the ship (Molland et al., 2011). In a preliminary analysis, the calculation of viscous and wave resistance components is carried out due to these two components' dominances. As mentioned above, an estimated percentage of the added resistance is required to predict the overall sum effect, even if the resistance components listed above have relatively less impact than the viscous and the wave resistance (Seok & Park, 2020). Calculation of other resistance components is needed for case-based precise measurements (Schultz, 2007). It is required to know the geometry of the ship's superstructure to calculate the wind resistance and the real wind velocity, and the direction of the voyage zone (Nguyen et al., 2017).

4. Ship resistance prediction methods

It has been mentioned about the effects of environmental conditions on the ship resistance in the seas. However, the approximate estimation of these forces' magnitudes makes it possible to design each ship's propulsion system. This prediction method was initially created based on similar vessels to consider the historical development of the ship design process. Today, it is made on a project basis with the convenience of technology and is mentioned below sections.

4.1. Holtrop-Mennen method

The Holtrop-Mennen method was introduced in the late 1970s and early 1980s (Holtrop, 1984; Holtrop and Mennen, 1982) and developed based on regression analysis to calculate resistance and propulsion by data gathered from random model ships and full-scale data. The applicability of the method is illustrated with equations (1), (2), and (3) (Birk, 2019):

$$Fr \leq 0.45 \tag{1}$$

$$0.55 \leq C_p \leq 0.85 \tag{2}$$

$$3.9 \leq L/B \leq 9.5 \tag{3}$$

where Fr Froude number, C_p prismatic coefficient based on L_{WL}, L length in the waterline, and B molded beam.

The reason for adding this part is to enlighten the researchers reading this chapter without any knowledge of the ship resistance literature. It is the well-known preliminary design estimate for resistance and propulsion since its simplicity, ease to adopt computer software, and ease of calculation (Bassam, 2017). The method calculates the total resistance in equation (4) by dividing it into subcategories as frictional resistance R_F, appendage resistance R_{APP}, wave resistance R_W, the additional pressure resistance of bulbous bow near the water surface R_B, the additional pressure resistance due to transom immersion R_{TR}, and model-ship correlation resistance R_A (Holtrop, 1984).

$$R_{total} = (1 + k_1)R_F + R_{APP} + R_W + R_B + R_{TR} + R_A \quad (4)$$

where $(1 + k_1)$ is the form factor describing viscous resistance of a ship with R_F.

Components of total resistance are calculated as Reynolds and Froude numbers for the specified service speeds as shown in equations (5) and (6), respectively.

$$Re = v_s L/\gamma \quad (5)$$

$$Fr = v_s/\sqrt{g\,L} \quad (6)$$

where v_s ship speed, g gravitational acceleration, L length of waterline, Re Reynolds number, and γ kinematic viscosity of a fluid.

On the other hand, wind resistance has a remarkable effect on total ship resistance on the mentioned ships (LNG carriers, car-ferries, container ships) and should be added to total ship resistance calculations as R_{WL} as shown in equation (7).

$$R_{total} = (1 + k_1)R_F + R_{APP} + R_W + R_B + R_{TR} + R_A + R_{WL} \quad (7)$$

4.2. Model testing in a towing tank

Model experiments are carried out by towing a model of a particular scale of the case ship. The scaled ship model in the towing tank is connected to the towing carriage that runs on two rails along both sides of the tank (Demirel, 2012).

According to William Froude's theory, ship resistance consists of two parts. The first is the ship's residual resistance, and the other is the friction resistance (Froude, 1888).

To accurately estimate the real ship resistance using model experiments, based on the assumption that the ship and the model have a dynamic similarity. Thus, the Froude number and Reynolds number of the vessel and model must be the same. However, it is impossible to preserve both the Froude number and Reynolds number in practice. Only Froude numbers are equalized by using the missing dynamic similarity. According to the ITTC 2017 method (ITTC, 2017), the total resistance coefficient (C_{TS}) of a ship without bilge keels is defined as for equation (8).

$$C_{TS} = (1 + k)C_{FS} + \Delta C_F + C_A + C_W + C_{AA} \quad (8)$$

where:
k is the form factor determined from the resistance test,
C_{FS} is the frictional resistance coefficient of the ship defined according to the ITTC-1957 model-ship correlation line,
ΔC_F is the roughness allowance,
C_A is the correlation allowance,
C_W is the wave resistance coefficient obtained from resistance tests and,
C_{AA} is the air resistance coefficient in full scale.

4.3. Estimation of the added air resistance

When examining the effect of wind on a moving body, it should be well known what the "apparent velocity" concept means. V_s is the ship velocity, V_w is the real wind velocity is represented in equation (9) and V_a is the apparent wind velocity. In this way, the ship is expressed as if it were standing, and the "steady-state" condition is created by obtaining V_a for the solution of the air resistance estimation problem (Molland et al., 2011).

$$\overrightarrow{V_a} = \overrightarrow{V_w} - \overrightarrow{V_s} \quad (9)$$

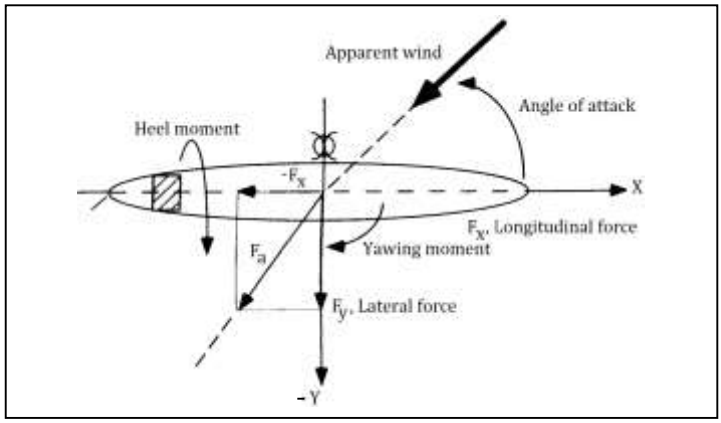

Figure 1 Coordinate system, forces, and moments (Blendermann, 1994).

The Cartesian coordinate system is chosen as shown in Figure 1 to describe forces, moments, and the ship's directions. x direction faces to the ship's bow, and y direction faces to the port side as well. Longitudinal force F_x occurs horizontally on the $x - axis$ and the ship's longitudinal area A_L which is affected by the wind is on this axis. Similarly, lateral force F_y and the ship's frontal area A_F are also on the $y - axis$. Wind forces are only regarded in the $xy - plane$. Vertical forces that occur on the $z - axis$ may contribute to the roll motion of the ship (Blendermann, 1994), but this is not in the scope of this research. General aerodynamic force calculation is expressed in equation (10).

$$F = \frac{1}{2} \times \rho_a \times A \times V^2 \times C \quad (10)$$

where, ρ_a is the density of air, A is the surface area perpendicular to the airflow, V is the velocity magnitude of the airflow, and C is the form factor related to the perpendicular area.

It can be inferred from equation (10) that the magnitude of air resistance depends on the size and shape of the ship's superstructure and the apparent wind velocity vector. According to the wind tunnel test results, it is stated that the drag force of a superstructure of a ship is based on the frontal area (A_F) located in the fore and aft direction of the ship (Molland et al., 2011). The air resistance of a vessel is generally calculated by taking a determined

percentage of the hull resistance. The reason for this, the air drag force is commonly a small portion of the total resistance.

ITTC recommends that, if there is an absence of detailed information about the structure of the ship model, air drag force F_{AA} may be approximated from equations (11) and (12) (Molland et al., 2011).

$$C_{AA} = 0.001 \times \frac{A_F}{S} \tag{11}$$

$$F_{AA} = C_{AA} \times \frac{1}{2} \times \rho \times S \times V^2 \tag{12}$$

where C_{AA} is the air drag coefficient, ρ is seawater density, S is the ship's hull wetted area, and V is the ship speed.

4.4. Computational fluid dynamics method

The scientists have studied the flow characteristics around the ships by solving Reynolds averaged Navier-Stokes equations (RANS) with advanced computers (Ozdemir et al., 2016). In this way, RANS equations used with the appropriate turbulence model have become an indispensable part of the shipbuilding process. The CFD analysis is performed using the finite volume method (FVM) by generating a suitable mesh structure under 3-dimensional, incompressible, turbulent, viscous, time-dependent, and multi-phase (air and water) flow conditions. Nowadays, RANS approaches are also applied to different ships, such as submarines, or multi-hull ships such as catamarans and trimarans (Dogrul et al., 2020).

5. Ship particulars and towing tank test results

The case ship in this study has a capacity of 71 cars and 450 passengers and has two main engines, one at each end of the hull, with a total power of $2 \times 1685\ kW$. Full head service speed is 14 knots, and it has a maneuvering speed of 4 knots. After the car-ferry design process was completed, (Bal et al., 2014) conducted ship resistance prediction tests at the ITU Ata Nutku towing tank. The characteristics of the ship and the model is shown in Table 1.

Table 1 Ship particulars and loading condition of the car-ferry and the model (Bal et al., 2014).

Model Number	M391		**Scale (λ)** 17.5	
Loading Condition	Δ=1318.049 ton		**Model**	**Ship**
Overall Length	L_{OA}	(m)	4.194	73.400
Waterline Length	L_{WL}	(m)	4.155	72.720

Wetted Surface Length	L_{WS}	(m)	4.155	72.720
Breadth (max)	B	(m)	0.994	17.400
Draught	$T_{midship}$	(m)	0.157	2.750
Draught (Aft)	T_A	(m)	0.157	2.750
Draught (Fore)	T_F	(m)	0.157	2.750
Displacement Volume	∇	(m^3)	0.240	1285.9
Displacement	Δ	(ton)	0.240	1318.05
Wetted Surface Area	A_{WS}	(m^2)	2.885	883.53
Block Coefficient	C_B		0.421	0.421
Prismatic Coefficient	C_P		0.559	0.559
Midship Coefficient	C_M		0.754	0.754
Waterplane Area Coefficient	C_{WP}		0.681	0.681
Longitudinal Center of Buoyancy	LCB	(m) (+ fore)	2.097	36.701
Longitudinal Center of Floatation	LCF	(m) (+ fore)	2.097	36.699
Service Speed	V_S	(m/s, knot)	1.72 m/s	14 knots

* Seawater density for the full-scale ship is taken as 1025 kg/m^3

Due to the similarity of the Froude number (Fr) in towing tank experiments, the model tests are performed at lower speeds to find the total resistance at the actual speed of the ship. The primary concern here is that the ship's total resistance coefficients and the model are the same. The values related to tank tests are shown in Table 2. V_s and V_m are velocities of ship and model respectively. R_{TM}(towing) is the resistance force that occurs on the ferry model during the tank experiments. R_{TS}(towing) is the ship total resistance force and R_{TS}(H&M) is total resistance value, which is calculated from the Holtrop-Mennen method as seen in equation 4. The added resistance due to the appendages has not been considered in the calculations in Table 2.

Table 2 Towing tank test results for the given loading condition of the car-ferry and the model (Bal et al., 2014).

Fr	V_S (knot)	V_M (m/s)	R_{TS}(towing) (kN)	R_{TS}(H&M) (kN)	R_{TM}(towing) (N)
0.135	7.0	0.86	19.63	15.99	5.22
0.154	8.0	0.98	24.81	20.68	6.57
0.173	9.0	1.11	30.33	26.25	8.00
0.193	10.0	1.23	37.09	32.8	9.70
0.212	11.0	1.35	45.98	40.8	11.82
0.231	12.0	1.48	57.75	50.75	14.49
0.250	13.0	1.60	75.19	63.59	18.21
0.270	14.0	1.72	95.67	80.04	22.52
0.279	14.5	1.78	108.25	89.50	25.10
0.289	15.0	1.84	122.28	98.96	27.96

6. Definition of the case study

For all the resistance calculations, a car-ferry navigates between Üçkuyular and Bostanlı piers (in Izmir Bay) with an average of 20 voyages per day assigned as the case ship. In this logistic process, this liner ferry serving back and forth between Üçkuyular-Bostanlı as ten voyages in one direction. Figure 2 shows a google maps representation of the Üçkuyular-Bostanlı voyage and Izmir Bay's statistical wind data.

Figure 2 Definition of Üçkuyular-Bostanlı voyage and wind statistics (Korkmaz and Cerit, 2016; Maps, 2020; Windfinder, 2020).

The monthly statistical data taken from "*windfinder.com"* depending on wind direction and velocity for the Izmir Bay, which will be used in predictions for the car-ferry's air resistance, is shown in Figure 3.

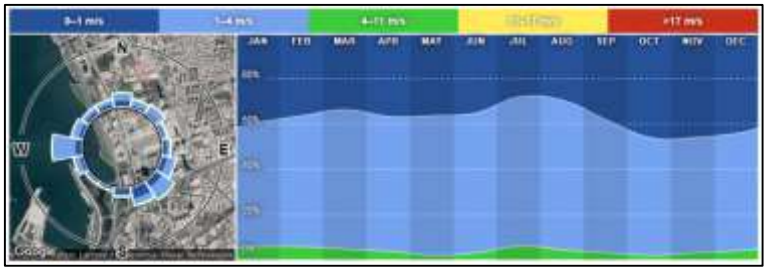

Figure 3 The monthly average wind data of Izmir Bay (Windfinder, 2020).

As shown in Figure 3, the prevailing wind is from the west direction in the range of 1-4 m/s most of the year in Izmir Bay. In this study, all calculations have been conducted with the parameter as 4 m/s west wind. The purpose of the orientation between the 4 m/s west wind and the ship's motion was encountered through the voyage. As shown in Figure 2, due to the angle between "ship's forward direction" and "wind direction", analyses have been made by the components of the true wind velocity of 4 m/s.

6.1. References and fundamentals of the computations

Computational Fluid Dynamics (CFD) model with a steady Reynolds averaged Navier-Stokes (RANS) approach, and $k-\varepsilon$ turbulence model has been utilized to reveal the air resistance of the car-ferry under the 4 m/s west wind. Defining the coordinate system is the first step for the CFD calculations and their analysis. The forward direction of the ferry for Üçkuyular-Bostanlı and Bostanlı-Üçkuyular voyages have been accepted as $+x$-direction and the port side of the ship as the $+y$-direction. To determine the direction of the wind relative to the vessel, the x and y-direction components of the west wind force have been evaluated independently. According to the definition of the $+x$ and $+y$ directions as aforementioned, the wind velocity's component on the $x-axis$ will occur on the ship's forward, while the wind component on the $y-axis$ will emerge as the heeling force. Thus, due to the summation of velocity vectors in the same axes, a reduction to two velocity components is achieved as input parameters for the CFD analysis.

Figure 4. CFD analysis control volume for Üçkuyular-Bostanlı voyage.

All the CFD analyses have been performed by the STAR-CCM+ software and divided into two sections as departure and arrival routes, which simplifies the assessment of the results. The definition of the control volume for the Üçkuyular-Bostanlı voyage to perform calculations is shown in Figure 4.

The "bottom" surface of the control volume, parallel to the $xy - plane$, represents the seawater-air boundary. The bottom surface has been defined as the "slip wall" to neutralize the boundary layer. The port side is where the wind blows, and the starboard side is the flow outlet area. These are defined respectively as "velocity inlet" and "pressure outlet" type. The "fore" and "aft" boundaries of the control volume are the "symmetry" faces, and their extensions are described as affectless. Finally, the "top" surface has been determined as the "velocity inlet", to prevent the formation of the boundary layer and ensure the continuity of the uniform flow in the wind flow direction.

6.2. Grid system

After defining the model geometry's boundary conditions in the CFD analysis, creating the "trimmer mesh" type structure of the control volume is performed and shown in Figure 5. In this way, the virtual experiment model is divided into finite-sized pieces, and the problem is tried to be solved with Reynolds-averaged Navier-Stokes (RANS) equations. However, in the solution of the problem, the size of these finite elements (cells) and in which structure they connect to each other (triangle, quadrilateral, pyramid, tetrahedron, etc.) is of great importance (Hefny and Ooka, 2009).

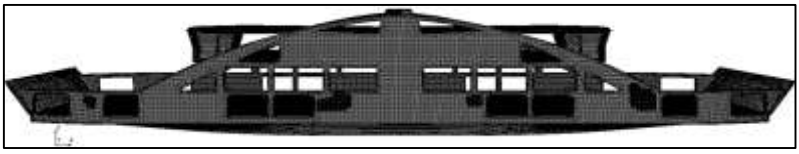

Figure 5 The mesh structure of the car-ferry on the 3D view

Since the analysis process has been completed by utilizing RANS equations in each cell, the "mesh" structure's suitability for problem-solving is controlled by some parameters. The thresholds of these parameters and the values obtained are listed in Table 3.

Table 3 Mesh structure output parameters of the control volume.

Quality thresholds	***Required***	***Attained***
Face Validity	1.000000 (min)	1.000000
Cell Quality	0.000010 (min)	0.048148
Face Planarity	0.700000 (min)	0.715931
Volume Change	0.011000 (max)	0.007499
Skewness	0.089000 (min)	0.097396

The “surface control” definition has been made as a feature of the CFD analysis software on all surfaces shown in Figure 5, and 6 “prism layers” have been assigned to calculate the wind force affecting the upper structure of the ferry more precisely. The form obtained by taking a section from the ferry center plane to show the mentioned above in detail is shown in Figure 6. The control volume consists of a total of 11,045,990 Cells, 32,945,631 Faces and 11,751,460 Vertices.

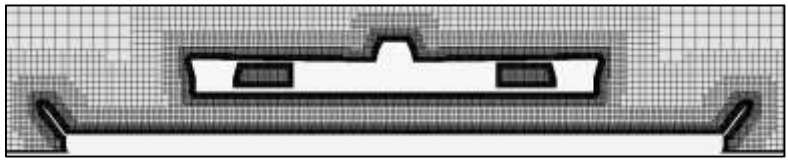

Figure 6 The mesh structure of the car-ferry in the center plane.

7. Results

After defining the CFD analysis’s boundary conditions and obtaining the proper mesh structure, the analysis has been run in the next stage. All calculations performed in this study are steady-state solutions. Investigations could be done under different conditions and in different situations. The study has been carried out within limits specified here. The results in this section are derived from some limitations. These are:

- The sea state is calm water (no current and no wave),
- The wind state is predominant wind direction and velocity,
- Car-ferry is not affected by external forces; there is no deviation from the navigation and not any dynamic ship movement,
- The ship is navigating in full load capacity (at design draft).

As shown in Figure 7, including the cases where ship speeds are different, the problem has been converged at a minimum of 10-3 residual values accuracy after approximately 1000th iteration. However, more than 1000 solution iterations were used to validate the accuracy of the solutions. The graph showing the residual values in Figure 7 belongs to the Üçkuyular-Bostanlı voyage under the real wind speed of 4 m/s from the west and ship speed of 10 knots.

The turbulence model $k-\varepsilon$ has some calculation parameters, as seen in the legend of Figure 7. The “Tdr” indicates the turbulent dissipation rate, and the “Tke” is for the turbulent kinetic energy, as seen below. Figure 7 contains residual values indicating the difference in calculations between

the two iterations related to RANS equations such as Continuity, X-momentum, Y-momentum, and Z-momentum.

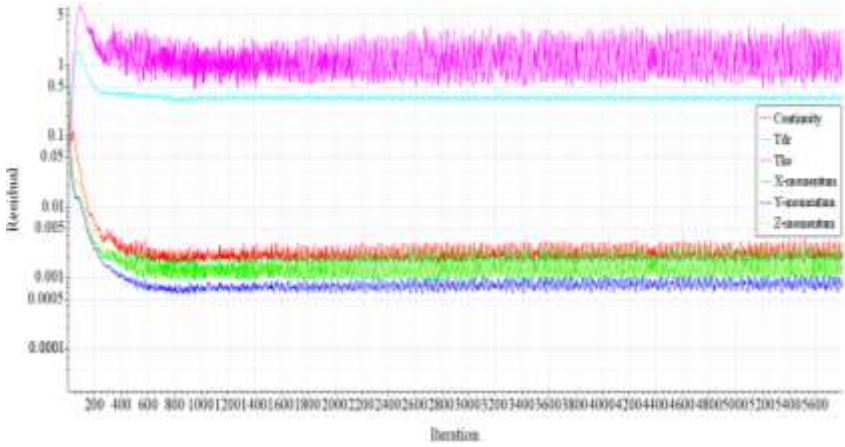

Figure 7 CFD calculation residual values of the Üçkuyular-Bostanlı voyage (V_s= 10 knots, V_w= 4 m/s west).

According to the technical data of the ferry, it is seen that the maximum speed is 15 knots. The round-trip voyages with the 1-knot speed intervals and 9.5 knots service speed have been used for calculations to predict the added wind resistance of the ship.

A total of 32 analyses have been conducted under 4 m/s wind conditions, 16 of which are for the Üçkuyular-Bostanlı voyage, and the remaining belong to the Bostanlı-Üçkuyular. Results of all the performed analyses are indicated in Table 4 and Table 5. The towing tank resistance values between 1-6 knots have been derived from test results' interpolation between 7-15 knots.

Table 4 CFD analysis results for wind resistance of Üçkuyular-Bostanlı voyage.

Ship speed (+x)		***Real wind speed (m/s)***		***Apparent wind speed (m/s)***		***Wind force [N]***	
knot	*m/s*	*x axis*	*y axis*	*x axis*	*y axis*	*x axis*	*y axis*
15	7.716	1.6269	-3.65	-6.0891	-3.65	-6,504	-19,058
14	7.2016	1.6269	-3.65	-5.5747	-3.65	-5,610	-18,070
13	6.6872	1.6269	-3.65	-5.0603	-3.65	-4,885	-17,102
12	6.1728	1.6269	-3.65	-4.5459	-3.65	-4,228	-15,702
11	5.6584	1.6269	-3.65	-4.0315	-3.65	-3,373	-14,211

10	5.144	1.6269	-3.65	-3.5171	-3.65	-2,674	-13,099
9.5	4.8868	1.6269	-3.65	-3.2599	-3.65	-2,431	-12,352
9	4.6296	1.6269	-3.65	-3.0027	-3.65	-2,226	-11,754
8	4.1152	1.6269	-3.65	-2.4883	-3.65	-1,789	-10,981
7	3.6008	1.6269	-3.65	-1.9739	-3.65	-1,220	-10,207
6	3.0864	1.6269	-3.65	-1.4595	-3.65	-757	-9,895
5	2.572	1.6269	-3.65	-0.9451	-3.65	-644	-9,724
4	2.0576	1.6269	-3.65	-0.4307	-3.65	-339	-9,565
3	1.5432	1.6269	-3.65	0.0837	-3.65	-42	-9,576
2	1.0288	1.6269	-3.65	0.5981	-3.65	293	-9,515
1	0.5144	1.6269	-3.65	1.1125	-3.65	508	-9,483

Table 5. CFD analysis results for wind resistance of Bostanlı-Üçkuyular voyage.

Ship speed (+x)		***Real wind speed (m/s)***		***Apparent wind speed (m/s)***		***Wind force [N]***	
knot	*m/s*	*x axis*	*y axis*	*x axis*	*y axis*	*x axis*	*y axis*
15	7.716	-1.6269	3.65	-9.3429	3.65	-14,225	25,475
14	7.2016	-1.6269	3.65	-8.8285	3.65	-12,840	24,400
13	6.6872	-1.6269	3.65	-8.3141	3.65	-11,545	23,345
12	6.1728	-1.6269	3.65	-7.7997	3.65	-10,195	22,381
11	5.6584	-1.6269	3.65	-7.2853	3.65	-9,083	21,390
10	5.144	-1.6269	3.65	-6.7709	3.65	-7,914	20,361
9.5	4.8868	-1.6269	3.65	-6.5137	3.65	-7,358	19,838
9	4.6296	-1.6269	3.65	-6.2565	3.65	-6,846	19,315
8	4.1152	-1.6269	3.65	-5.7421	3.65	-5,864	18,367
7	3.6008	-1.6269	3.65	-5.2277	3.65	-5,131	17,356
6	3.0864	-1.6269	3.65	-4.7133	3.65	-4,438	16,186
5	2.572	-1.6269	3.65	-4.1989	3.65	-3,739	14,586
4	2.0576	-1.6269	3.65	-3.6845	3.65	-2,906	13,463
3	1.5432	-1.6269	3.65	-3.1701	3.65	-2,360	12,111
2	1.0288	-1.6269	3.65	-2.6557	3.65	-2,015	11,158
1	0.5144	-1.6269	3.65	-2.1413	3.65	-1,418	10,528

According to the definitions mentioned above, the negative values in the "$x-axis$" column of the wind force values in Table 4 imply the drag force, since the direction of motion of the ship in the direction of $+x$ for the Üçkuyular-Bostanlı voyage. The negative force values in the "$y-axis$" column of Table 4 mean that the ship tends to heel towards the starboard side. As in Table 4, for the Bostanlı-Üçkuyular voyage, the ship also navigates in the $+x$-direction, and the $+y$-direction indicates the port side of the vessel. Real wind state prevents the ship's forward motion since all of the wind force values as seen in the "$x-axis$" column of Table 5 are negative; also, the "$y-axis$" column values enforce the ship to the port side. The fact that ship wind resistance calculations have been

achieved from the literature and transformed into an empirical form as equation (12) shows that wind force's effect on ship resistance cannot be neglected. The added wind resistance forces, that calculated by both CFD and ITTC recommendation, for the Üçkuyular-Bostanlı and Bostanlı-Üçkuyular voyages are shown in Table 6 to compare each other. In this study, only the force component of the wind in the forward direction of the ship, that is, on the $x - axis$, is considered. For this reason, negative ones among the values shown in Table 6 have a slowing effect on the car-ferry, while positive ones do not create added resistance since the ship is in the voyage direction. As shown in Table 7, the bare hull resistance values are indicated as "towing tank resistance" values. As mentioned in Table 2, the results of the towing tank tests performed by (Bal et al., 2014) are the bare hull resistance values used to estimate the case-based total resistance calculations of the ferry used in this study.

Table 6 Comparison of the results of air resistance prediction methods.

Ship speed (+x)		***Üçkuyular-Bostanlı voyage***		***Bostanlı-Üçkuyular voyage***		***Average***	***Average***
		ITTC method	***CFD method***	***ITTC method***	***CFD method***	***ITTC method***	***CFD method***
knot	*m/s*	*[N]*	*[N]*	*[N]*	*[N]*	*[N]*	*[N]*
15	7.716	-3,539	-6,504	-3,539	-14,225	-3,539	-10,364.5
14	7.2016	-3,083	-5,610	-3,083	-12,840	-3,083	-9,225
13	6.6872	-2,659	-4,885	-2,659	-11,545	-2,659	-8,215
12	6.1728	-2,265	-4,228	-2,265	-10,195	-2,265	-7,211.5
11	5.6584	-1,903	-3,373	-1,903	-9,083	-1,903	-6,228
10	5.144	-1,573	-2,674	-1,573	-7,914	-1,573	-5,294
9.5	4.8868	-1,420	-2,431	-1,420	-7,358	-1,420	-4,894.5
9	4.6296	-1,274	-2,226	-1,274	-6,846	-1,274	-4,536
8	4.1152	-1,007	-1,789	-1,007	-5,864	-1,007	-3,826.5
7	3.6008	-771	-1,220	-771	-5,131	-771	-3,175.5
6	3.0864	-566	-757	-566	-4,438	-566	-2,597.5
5	2.572	-393	-644	-393	-3,739	-393	-2,191.5
4	2.0576	-252	-339	-252	-2,906	-252	-1,622.5
3	1.5432	-142	-42	-142	-2,360	-142	-1,201
2	1.0288	63	293	63	-2,015	63	-861
1	0.5144	16	508	16	-1,418	16	-455

Table 7 Total resistance calculations for Üçkuyular-Bostanlı voyage.

Ship speed (+x)		***Towing tank resistance (bare hull)***	***Holtrop-Mennen res. (bare hull)***	***CFD wind + Towing tank res.***	***CFD wind / Towing tank res. ratio***	***Empiric wind + Towing tank res.***	***Empiric wind / Towing tank res.***
knot	*m/s*	*[N]*	*[N]*	*[N]*	*%*	*[N]*	*%*
15	7.716	-122,280	-98,960	-128,784	5.32	-125,819	2.89
14	7.2016	-95,670	-80,044	-101,280	5.86	-98,753	3.22
13	6.6872	-75,190	-63,586	-80,075	6.50	-77,849	3.54
12	6.1728	-57,750	-50,754	-61,978	7.32	-60,015	3.92

11	5.6584	-45,980	-40,800	-49,353	7.34	-47,883	4.14
10	***5.144***	***-37,090***	***-32,800***	***-39,764***	***7.21***	***-38,663***	***4.24***
9.5	4.8868	-33,710	-29,370	-36,141	7.21	-35,130	4.21
9	4.6296	-30,330	-26,250	-32,556	7.34	-31,604	4.20
8	4.1152	-24,810	-20,680	-26,599	7.21	-25,817	4.06
7	3.6008	-19,630	-15,990	-20,850	6.22	-20,401	3.93
6	3.0864	-15,204	-11,935	-15,961	4.98	-15,770	3.72
5	2.572	-12,106	-8,460	-12,750	5.32	-12,500	3.25
4	2.0576	-9,640	-5,560	-9,979	3.52	-9,892	2.61
3	1.5432	-7,676	-3,240	-7,718	0.55	-7,818	1.84
2	1.0288	-6,112	-1,520	-5,819	4.79	-6,049	1.03
1	0.5144	-4,867	-415	-4,359	10.44	-4,851	0.32

All calculations and reference values executed for the Üçkuyular-Bostanlı voyage in Table 7 are also valid for the opposite voyage (Bostanlı-Üçkuyular) in Table 8.

Table 8 Total resistance calculations for Bostanlı-Üçkuyular voyage.

Ship speed (+x)		***Towing tank resistance***	***Holtrop-Mennen res.***	***CFD wind + Towing tank res.***	***CFD wind / Towing tank res. ratio***	***Empiric wind + Towing tank res.***	***Empiric wind / Towing tank res.***
knot	*m/s*	*[N]*	*[N]*	*[N]*	*%*	*[N]*	*%*
15	7.716	-122,280	-98,960	-136,505	11.63	-125,819	2.89
14	7.2016	-95,670	-80,044	-108,510	13.42	-98,753	3.22
13	6.6872	-75,190	-63,586	-86,735	15.35	-77,849	3.54
12	6.1728	-57,750	-50,754	-67,945	17.65	-60,015	3.92
11	5.6584	-45,980	-40,800	-55,063	19.75	-47,883	4.14
10	5.144	-37,090	-32,800	-45,004	21.34	-38,663	4.24
9.5	4.8868	-33,710	-29,370	-41,068	21.83	-35,130	4.21
9	4.6296	-30,330	-26,250	-37,176	22.57	-31,604	4.20
8	4.1152	-24,810	-20,680	-30,674	23.64	-25,817	4.06
7	3.6008	-19,630	-15,990	-24,761	26.14	-20,401	3.93
6	3.0864	-15,204	-11,935	-19,642	29.19	-15,770	3.72
5	2.572	-12,106	-8,460	-15,845	30.89	-12,500	3.25
4	2.0576	-9,640	-5,560	-12,546	30.15	-9,892	2.61
3	1.5432	-7,676	-3,240	-10,036	30.75	-7,818	1.84
2	1.0288	-6,112	-1,520	-8,127	32.97	-6,049	1.03
1	0.5144	-4,867	-415	-6,285	29.14	-4,851	0.32

8. Conclusion

In this study, a significant difference between the bare hull resistance values calculated by the Holtrop-Mennen method and the towing tank resistance values is observed. Since the hull form of the ferry is a soft multi-chine type, in the empirical resistance prediction equation of Holtrop-Mennen, the effect of the reference ships with the conventional round bilge hull type is seen. The towing tank tests and the CFD analysis are performed with advanced computer technology in such studies as this. Since carrying on the towing tank tests with the wind taken into account is

not practicable and feasible, a ship's total resistance is tried to be calculated by evaluating the superstructure resistance by the CFD analysis.

Within this research scope, wind resistance has been tried to be predicted with CFD analysis, and also, the empirical ITTC formulas are for comparison. It was accepted that the ferry's average cruising speed is 10 knots, and the predominant wind is blowing from the west direction at a speed of 4 m/s. Direction and velocity magnitudes of apparent wind to be used in CFD and empirical calculations are determined within these assumptions. The average added wind resistance of the round trip of the ship was calculated by CFD method as 14.27% (Bostanlı-Üçkuyular 21.34% and Üçkuyular-Bostanlı 7.21%) of the calm water resistance. According to the ITTC recommendation, this result was calculated as 4.24%. Since the calculation method recommended by ITTC aims to provide preliminary information, the importance of case-based analysis in such cases becomes evident. Besides, since the wind resistance affecting the ship is directly affected by the ship's superstructure, it has been decided that CFD analysis is necessary for situations where the superstructure, such as the ferry, is considerable.

Considering the financial and environmental impacts of fossil fuel consumption and evolving more restricted rules/regulations enforced by the organizations, it is distinguished that the daily fuel consumption of a ferry, which makes 20 voyages per day and its superstructure is unwieldy compared to other ships, increases by 14.27 percent. Therefore, the aerodynamic resistance calculation of the superstructure of a vessel is vital for shipping operations. It can be concluded that wind tunnel tests have become a necessity in the technical specifications of the container ship, ferry, and car-carrier ships, where the effect of their superstructures on the total resistance is crucial.

The ship's main engine power's determination process combines the calm water resistance by using the towing tank tests, empirical formulas, and CFD analysis. The sea margin between 15-30% of the calm water resistance is generally added to a ship's calm water resistance. Considering the ship's life cycle, if overall maintenance is not performed correctly, its total performance will deteriorate, which will trigger the vessel not to reach the desired service speed and fuel consumption values. Even if the sea margin is taken into account for calculating the main engine power for the ferry examined in this study as 30%, 14.27% of it will be composed of only wind resistance. As mentioned before, added resistance acting on ships has components such as wave breaking resistance, appendage resistance, roughness resistance, air and wind resistance, steering resistance. This study shows that the added wind resistance calculation with the CFD analysis is crucial that the added sea margin of 30% is not sufficient for this kind of unwieldy ship.

The restrictions mentioned above can be amended with future studies as; route and service speed optimization, sea trial tests for comparison with the study data, and comparing this theoretical study by calculating a 0-10 years old ferry.

Acknowledgement

We are thankful for the software support on this study to the Yıldız Technical University, Department of Naval Architecture and Marine Engineering.

References

Bal, Ş., Danışman, D. B., Kanıpek, Z. and Delen, C. (2014). *Çift Başlı Feribot Teknesi Model Deneyleri ve Analizi*. Istanbul.

Bassam, A. (2017). *Use of voyage simulation to investigate hybrid fuel cell systems for marine propulsion*.

Birk, L. (2019). Holtrop and Mennen's Method. In *Fundamentals of Ship Hydrodynamics* (pp. 611–627). Chichester, UK: John Wiley & Sons, Ltd. https://doi.org/10.1002/9781119191575.ch50

Blendermann, W. (1994). Parameter identification of wind loads on ships. *Journal of Wind Engineering and Industrial Aerodynamics*, *51*(3), 339–351. https://doi.org/10.1016/0167-6105(94)90067-1

Demirel, Y. K. (2012). *Yüzey Kirliliğinin Gemi Direnci Üzerindeki Etkisinin İncelenmesi*. Fen Bilimleri Enstitüsü, İstanbul. Retrieved from https://polen.itu.edu.tr/handle/11527/4257

Dogrul, A., Song, S. and Demirel, Y. K. (2020). Scale effect on ship resistance components and form factor. *Ocean Engineering*, *209*, 107428. https://doi.org/10.1016/j.oceaneng.2020.107428

Feng, P. Y., Ma, N. and Gu, X. C. (2010). Long-term prediction of speed reduction due to waves and fuel consumption of a ship at actual seas. In *Proceedings of the International Conference on Offshore Mechanics and Arctic Engineering - OMAE* (Vol. 4, pp. 199–208). Shanghai: American Society of Mechanical Engineers Digital Collection. https://doi.org/10.1115/OMAE2010-20308

Froude, W. (1888). *The Resistance of Ships*. US Government Printing Office.

Hefny, M. M. and Ooka, R. (2009). CFD analysis of pollutant dispersion around buildings: Effect of cell geometry. *Building and Environment*, *44*(8), 1699–1706. https://doi.org/10.1016/j.buildenv.2008.11.010

Holtrop, J. (1984). A Statistical Re-Analysis of Resistance and Propulsion Data.

Holtrop, J. and Mennen, G. G. (1982). An Approximate Power Prediction Method. *International Shipbuilding Progress*, *29*, 166–170. Retrieved from https://trid.trb.org/view.aspx?id=423662

ITTC. (2017). *ITTC-Recommended Procedures and Guidelines ITTC-Recommended Procedures and Guidelines Register 0.0 Register*.

Kim, M., Hizir, O., Turan, O., Day, S. and Incecik, A. (2017). Estimation of added resistance and ship speed loss in a seaway. *Ocean Engineering*, *141*, 465–476. https://doi.org/10.1016/j.oceaneng.2017.06.051

Korkmaz, S. A. and Cerit, A. G. (2016). Applications of Fuel Cell Technologies in Ships and A System Dynamics Approach. In *The Second Global Conference on Innovation in Marine Technology and the Future of Maritime Transportation* (pp. 42–56). Muğla-Bodrum.

Larsson, L. and Leif, B. (1990). A method for resistance and flow prediction in ship design.

Lewis, E. V. (Ed.). (1989). *Principles of Naval Architecture Second Revision*. Jersey: Sname.

Maps, G. (2020). Google maps. Retrieved August 19, 2020, from https://www.google.com/map

Molland, A. F., Turnock, S. R. and Hudson, D. A. (2011). *Ship Resistance and Propulsion*. Cambridge: Cambridge University Press. https://doi.org/10.1017/CBO9780511974113

Nguyen, T. V., Shimizu, N., Kinugawa, A., Tai, Y. and Ikeda, Y. (2017). Numerical studies on air resistace reduction methods for a large container ship with fully loaded deck-containers in oblique winds. In *In MARINE VII: proceedings of the VII International Conference on Computational Methods in Marine Engineering* (pp. 1040–1051). CIMNE. Retrieved from https://upcommons.upc.edu/handle/2117/332151

Ozdemir, Y. H., Cosgun, T., Dogrul, A. and Barlas, B. (2016). A numerical application to predict the resistance and wave pattern of KRISO container ship. *Brodogradnja: Teorija i Praksa Brodogradnje i Pomorske Tehnike*, *67*(2), 47–65. https://doi.org/10.21278/brod67204

Schultz, M. P. (2007). Effects of coating roughness and biofouling on ship resistance and powering. *Biofouling*, *23*(5), 331–341. https://doi.org/10.1080/08927010701461974

Seok, J. and Park, J.-C. (2020). Comparative Study of Air Resistance with and without a Superstructure on a Container Ship Using Numerical Simulation. *Journal of Marine Science and Engineering*, *8*(4), 267. https://doi.org/10.3390/jmse8040267

Shigunov, V. (2018). Numerical Prediction of Added Power in Seaway.

Journal of Offshore Mechanics and Arctic Engineering, *140*(5). https://doi.org/10.1115/1.4039955

Tupper, E. C. (2013). *Introduction to naval architecture*. Butterworth-Heinemann.

Van He, N., Mizutani, K. and Ikeda, Y. (2016). Reducing air resistance acting on a ship by using interaction effects between the hull and accommodation. *Ocean Engineering*, *111*, 414–423. https://doi.org/10.1016/j.oceaneng.2015.11.023

Windfinder. (2020). windfinder. Retrieved August 19, 2020, from https://www.windfinder.com/#12/38.4244/27.1029/2020-07-11T09:00Z

CHAPTER II

VARIOUS INDUSTRIAL APPLICATIONS OF SELF-CLEANING AND MULTIFUNCTIONAL SURFACES

Ceyda BİLGİÇ

(Assoc. Prof. Dr.); Eskişehir Osmangazi University, Eskişehir, Turkey
e-mail: cbilgic@ogu.edu.tr, Orcid No: 0000-0002-9572-3863

Şafak BİLGİÇ

(Asst. Prof. Dr.); Eskişehir Osmangazi University, Eskişehir, Turkey
e-mail: safakb@ogu.edu.tr, Orcid No: 0000-0002-9336-7762

1. Introduction

After millions of years of slow evolution and natural selection, the majority of organisms have developed perfect multifunctional surfaces to adapt to their living environment. In nature, some animals and plants have a surface with special wettability (Darmanin and Guittard, 2015; Zhang et al., 2012). For example, lotus leaves grow in the silt but not imbrued because of their self-cleaning property; (Zorba et al., 2008) water strider is able to walk and jump on water; (Gao and Jiang, 2004; Hu et al., 2003) red rose petals show high adhesive force to water droplet and can capture droplets; (Feng et al., 2008) the rain drops and dew are inclined to slide along the leaf vein and finally toward the root of a rice leaf, helping the rice to survive; (Feng et al., 2002; Wu et al., 2011) butterfly can even fly in the rain because the directional adhesion of the butterfly wing allows it to shake raindrops off; (Zheng et al., 2007) mosquito eyes have the antifog ability, ensuring an unimpaired view in humid conditions where the mosquitoes usually live; (Gao et al., 2007) desert beetle can harvest fog by its shell in the arid desert; (Parker et al., 2001) and gecko feet have multifunctions of superhydrophobicity, high adhesion, and reversible adhesion.

It is found that all of these unique wettabilities are caused by the combined effect of both different hierarchical surface microstructures and chemical compositions, verifying the unification and coordination of structure and performance. Inspired by the above phenomena, a high amount of artificial functional surfaces with special wettability has been designed and prepared, and those surfaces have been widely used in our lives (Tian et al., 2014; Wen et al., 2015; Su et al., 2016; Yong et al.,

2015; Yao et al., 2011; Liu et al., 2010). In fact, the study of underwater superoleophobicity was also originated from the revelation of the antioil function of fish scales. Compared to the seabirds that are endangered by oil pollution during a spill accident, fish can keep their body clean in the same oil-polluted water. In 2009, Liu and co-workers discovered the underlying mechanism of the antioil ability of fish body, which comes from the underwater superoleophobicity of the fish scales (Liu et al., 2009). The fish body is completely covered by well-aligned fan-like scales. Fish scale is made up of hydrophilic calcium protein, phosphate, and a thin layer of mucus.

Huang et al, have used multi-scale nano-/micro-roughness structures to construct self-cleaning surfaces (Huang et al., 2013). The presence of the hydrophobic silica nanoparticles enables the increase of the water contact angle. Moreover, the nanoscale roughness reduces adhesion forces between the water drop and the surface. This phenomenon is behind the dramatic decrease of the contact angle hysteresis which is about 85% between smooth particles and particles with nanoscale roughness. This effect improves the self-cleaning properties. The surface repellency against liquids with low surface tension should be evaluated to broaden its application fields (e.g. anti-fingerprint application).

Zhao and Law designed an amphiphobic directional micro-grooved surface (Zhao and Law, 2012). The as-prepared surface was characterized by re-entrant morphology and low surface energy. Different wetting behaviors in the parallel and orthogonal directions to surfaces grooves were found. Although both directions exhibited amphiphobic property, the wetting was more favorable in the parallel direction. Besides, liquid drops were found to be more mobile in the parallel direction (sliding angles between 4° and 8°) than in the orthogonal direction (sliding angles between 23° and 34°). The comparison of the anisotropic grooved surfaces with isotropic patterned pillar structures proved that self-cleaning is more important in the parallel direction of the grooved surfaces than in the random pillar arrays. Also, the directional textured surfaces were expected to be mechanically robust than pillar array surfaces. These performances are interesting for self-cleaning applications and robust super-repellency of water and oil.

Huovinen et al. have presented a simple and swift mass fabrication procedure to produce superhydrophobic and self-clean polymer surfaces without chemical modification (Huovinen et al., 2012). The prepared surfaces exhibit higher super-hydrophobicity and superior mechanical robustness compared to the hierarchical micro-nanostructures. The mechanical robustness was evaluated by the press and wear tests. The

contact angle measured on the micro-microstructure was greater than 150° even after tests, which demonstrates the durability of the super-hydrophobicity. However, the micro-nano structured surface lost its super-hydrophobicity after pressure was applied. Such surfaces can be suitable for anti-fingerprint function since super-hydrophobicity will be retained after being pressed by a finger. But, wetting behavior against organic liquids should be studied.

Recently, self-cleaning surfaces have attracted significant attention since it is highly desirable in many important applications; for example, since the surface is more wettable to water than to oil, it can be used as a detergent-free cleaning surface where water can easily replace the oil contaminants and push the oils away. A Self-cleaning surface can reduce the consumption of detergents that are made from petroleum. Therefore, it can save energy and protect the environment from detergent-related pollution, which are current environmental challenges. It can also be used as an anti-fogging surface, which is crucial for eyeglasses, camera lenses, automobiles, and medical instruments such as infrared microscopes (Howarter and Youngblood, 2007; Howarter and Youngblood, 2008).

This article exemplifies the importance of applications of self-cleaning and multifunctional materials. Self-cleaning surfaces are becoming an integral part of our daily life because of their utility in various applications such as windows, solar panels, cement, paints, etc. Various categories of materials for the fabrication of hydrophilic, hydrophobic, oleophobic, amphiphobic, and multifunctional surfaces and their synthesis routes have been discussed. Furthermore, different natural organisms exhibiting self-cleaning behavior have been analyzed and the fundamentals of self-cleaning attributes such as water contact angle, surface energy, contact angle hysteresis, etc. Self-cleaning surfaces with excellent water repellence and good mechanical properties are in high demand. However, producing such surfaces with resistance to mechanical abrasion and environmental weathering remains a key challenge.

2. Self-cleaning surfaces

Nelumbo nucifera (the lotus plant) is considered to be an embodiment of purity in Asian religions. The dirt-resistant property of the lotus leaf has made the researchers investigate its miracle effect in detail. Randomly distributed micro-papillae of about 5-9 μm in diameter enclosed by fine nanostructured branches of 120 nm in diameter was observed. The presence of such surface structures and epicuticular wax crystalloids made its surface highly superhydrophobic with small sliding angles. Thus the dirt particles are carried away by the rolling spherical water droplets, an intrinsic process called self-cleaning or lotus effect.

The chemical composition and the geometrical structure of solid surfaces govern the wettability (Feng et al., 2004). The angle measured through the droplet at the intervention of three phases - solid, liquid, and vapor, is referred to as the water contact angle (WCA) (Lafuma and Quere, 2003).

A self-cleaning surface is defined as a surface that is able to keep itself clean through the natural phenomenon without involving manual work. The Hydrophobic or hydrophilic phenomenon is the most used approach for self-cleaning surface treatment (Ragesh et al., 2014). Hydrophobic surfaces clean the dirt based on the formation of water droplets that roll away with dirt while hydrophilic surfaces clean the dirt through the formation of sheeting water that carries away dirt. In recent years, photocatalysis is also used to photo decompose the contaminants on the building surface so that the contaminants deposited from the polluted air change to washable and mineralized compounds (Cassar et al., 2003).

Since most in-air superoleophobic surfaces usually have superhydrophobicity, so such superamphiphobic surfaces also have a self-cleaning ability like ordinary superhydrophobic surfaces. The concept of the self-cleaning behavior of superamphiphobic surfaces with low liquid adhesion. Compared with a general surface, the water/oil droplet on a superamphiphobic surface shows a quasi-spherical shape. If a water/oil droplet is placed on a slightly tilted superamphiphobic surface, the droplet can easily roll away. Similar to the lotus leaf having the self-cleaning ability (Ragesh et al., 2014; Nishimoto and Bhushan, 2013; Yong et al., 2014; Zorba et al., 2008; Zhang, et al., 2012; Ge et al., 2015) during the Rolling process, the droplet will adhere and remove the foreign dirt particles on the material surface because it is easier for dust particles to stick to the liquid droplet than to the solid substrate. In this way, superamphiphobic surfaces can be kept clean. In contrast, liquid droplets just pass over the dust on the normally flat surface, leaving the dust particles behind. Underwater superoleophobic materials with ultralow oil adhesion also have an excellent self-cleaning function (Wu et al., 2011; Zhang et al., 2015).

Sun et al. prepared gecko foot-like hierarchical microstructures made of Polydimethylsiloxane (PDMS) by combining photolithography and soft lithography (Sun et al., 2008). After subsequent oxygen plasma treatment, the rough surface showed extreme underwater superoleophobicity. A soya bean oil droplet was deliberately put onto the surface as a pollutant in an air environment. The oil quickly adhered and wetted the sample surface. Interestingly, just by immersing the polluted sample into the water, the oil was completely removed, whereas the oil

on the untreated flat region was still retained; i.e., the oil was not washed away. This result revealed that underwater superoleophobic surfaces have a strong self-cleaning ability. Although both the underwater superoleophobic surface and superhydrophobic lotus leaf have self-cleaning functions, their self-cleaning abilities are caused by different physical mechanisms. Water droplets can easily roll away on a lotus leaf while taking away the dust particles on the leaf (Ragesh et al., 2014; Yong et al., 2014; Mazumder et al., 2014; Zorba et al., 2008; Zhang et al., 2012). However, the self-cleaning effect of the underwater superoleophobic surface originates from its intrinsic superhydrophilicity, since oil can be removed by the water injection (Nishimoto and Bhushan, 2013). Besides the surface tension of the water/oil/air interface, there is another main hydrophilic force to push the oil contamination out of the solid microstructures (Wu et al., 2011). A higher level of hydrophilicity usually results in a stronger hydrophilic force. Once the oil-polluted sample is gradually immersed in water, the water is injected into the rough microstructures and pushes the oil out, resulting in the oil impurity being cleared.

3. Multifunctional Surfaces

Multifunctional surfaces, as the name suggests have a wide range of potential applications with a greater degree of control and scalability. Multiple properties can be encompassed into such surfaces such as scratch-resistance, self-cleaning property, anti-icing, self-healing, anti-reflective property, etc. Lee et al. used a simple dip-coating technique to fabricate multifunctional polymer surfaces in an aqueous solution of dopamine (Lee et al., 2007). To biomimic the adhesive proteins in mussels, a thin film of polydopamine was developed using dopamine self polymerization. These films were used for a range of substrates like polymers, ceramics, noble metals, oxides, etc. An additional layer could be deposited using secondary reactions such as electrode-less metallization for depositing metal films, macromolecule grafting for bio-inert and bioactive surfaces, etc Wei et al. used oxidant-induced polymerization to synthesize polydopamine coatings which can be prepared in acidic/neutral/alkaline aqueous media (Wei et al., 2010). Such coatings are found to be multifunctional as well as material-independent. Inspired by the moth eyes which are antireflective and the cicada wings which are superhydrophobic in nature, Sun et al. tried to biomimic both these functionalities by fabricating multifunctional optical surfaces (a template technique) (Sun et al., 2008). Using the soft-lithography process, fluoropolymer nipple arrays are created which are subwavelength-structured. The enhancement of both anti-reflective and hydrophobic functionalities is done by the utilization of fluoropolymers. An

experiment and modeling have been done to study the effect of size and crystalline ordering of the replicated nipples on the antireflective property. Such surfaces find extensive applications in antireflection self-cleaning surfaces. Dingremont et al. tried to combine both physical vapor deposition and nitriding treatment in synthesizing multifunctional surfaces which made the coating to withstand higher loads, thus improving their mechanical strength (Dingremont et al., 1995). To synthesize biomedical surfaces, layer-by-layer assembly finds a great deal, which is also shown for local drug delivery systems. But such hydrophobic drugs have a drawback of poor loading capacity (Dingremont et al., 1995). New synthesis methods have been developed to combine both oleophobic and hydrophilic characters in coatings to overcome the limitation of thermodynamic surface energetics. Such smart surfaces possess different functional groups with favorable and unfavorable interactions with polar and non-polar liquids, respectively (Liu et al., 2013). In such smart surfaces, intercalation of oleophobic and hydrophilic constituents occurs. Oleophobic character is obtained when the interface, in presence of oil droplets gets occupied by a low-surface energy component. Nevertheless, due to the hydrophilic components, water molecules penetrate through such surfaces. Recently spray casting technique of nanoparticle-polymer suspensions on various substrates was used to fabricate nanocomposite coatings that encompass both superhydrophilicity and superoleophobicity (Yang et al., 2012). Such a dual character is due to the combined cooperation of oleophobic-hydrophilic groups for hierarchical surface structures. Fluorinated groups in high surface concentration occupied the interface in the presence of oil indicating the superoleophobic nature of the surfaces. Due to the surface molecular re-arrangement induced by water, water molecules could penetrate through these surfaces. Oleophobic-hydrophilic polymers with stimuli responses are a great venture for the fabrication of next-generation anti-fogging and self-cleaning coatings (Howarter and Youngblood, 2007; Howarter and Youngblood, 2008).

Smart materials like stimuli-responsive polymers on porous materials are a new attempt for oil/water separation. Inspired by the self-cleaning lotus effect, Zhang et al. have fabricated polyurethane foam that encompasses both superhydrophobicity and superhydrophilicity (Zhang et al., 2013). The as-prepared foam floats easily on water due to its low density, lightweight, and superhydrophobicity. Multifunctional properties are demonstrated by the foam-like material in oil/water separation, super-repellency towards corrosive liquids, and self-cleaning. Such a low-cost process is promising for the design of multifunctional foams that can be used for oil-spill clean-up in larger areas.

4. Industrial applications of self-cleaning and multifunctional materials

Inspired by the “lotus effect”, superhydrophobic wetting behavior is usually used to achieve a self-cleaning surface, which can remain free from dirt and grime (Nakajima et al., 2000; Fürstner, et al., 2005; Blossey, 2003). However, most of these surfaces will lose self-cleaning capability if the surface is ruined with oil contaminants due to its oleophilicity. To solve this problem, a surface that is more wettable to water than to oil can be used as the next generation self-cleaning surface (Howarter and Youngblood, 2008). On this oleophobic/hydrophilic surface, water itself can wash the oil away and no detergent is required; therefore, this surface can also be called a detergent-free self-cleaning surface. Howarter and Youngblood investigated the self-cleaning capability of simultaneously oleophobic/hydrophilic surfaces (Howarter and Youngblood, 2007). Oil and water dyed with red color were sequentially placed on the surface. After a little bit of tilting the substrate, all the oil droplets were displaced by water and were washed away from the glass slides. They also performed comparable experiments with hydrophobic-modified and clean glass slides. The oil droplets stayed on these two substrates and could not get washed away by water only. Brown et al. carried out a similar experiment to demonstrate the self-cleaning capability of glass slide modified with oleophobic/hydrophilic coating (Brown et al., 2014). Hexadecane on the coated glass slide could be rinsed away with water, leaving a clean surface. Moreover, Pan et al. extended the substrate from glass slides to cotton fabrics that are highly desired for the self-cleaning property in our daily life, and a good self-cleaning property was observed (Pan et al., 2014).

Self-cleaning surfaces have a large number of applications in everyday life, agriculture, industry, and military industries. Recently, many methods and strategies have been used to fabricate self-cleaning surfaces (Blossey, 2003; Liu and Jiang, 2011; Fürstner et al., 2005). Many of the self-cleaning coatings such as glasses, tiles, and tissues have been industrialized. Self-cleaning surfaces could be made using superhydrophobic surfaces.

The self-cleaning property of the superhydrophobic surface is necessary to prevent the degradation of efficiency of solar cells because the snow or dust can easily detach from the surfaces. The superhydrophobic coating was applied to solar cells with a dimension of 22 x 24 cm by Choi and Huh to investigate the effect of superhydrophobic surface on light to electricity efficiency of solar cells, and the results revealed that the short-current densities and open-circuit

voltages (Choi and Huh, 2010). The overall enhancement in energy conversion efficiency of solar cells with the superhydrophobic surface was about 10% against the solar cells with the normal surface. The self-cleaning property of the superhydrophobic surface was applied to the solar cells by Park et al. (Park et al., 2011). The experimental results revealed that the self-cleaning property of a superhydrophobic surface was helpful to maintain the efficiency of the solar cells at a high level, and the efficiency was recovered from 6.56% to 9.78% after the cleaning process.

Recently, silica substrates were used to construct superhydrophilic surfaces along with anti-reflective and antifogging properties. The presence of surface multiscale structures comprising hexagonally non-close-packed nanonipples covering micro-ommatidia was observed in the compound eyes of mosquitoes. Soft lithography technique was used to create an artificial compound eye with superhydrophobicity and anti-fogging properties that mimic mosquito compound eyes (Gao et al., 2007). Anti-reflection property is also found in insect wings for camouflage. Superhydrophobic antireflective self-cleaning properties were found in the wings of cicada (Lee et al., 2004; Zhang et al., 2006) Self-cleaning and anti-reflective properties were combined to form so-called multifunctional optical coatings (Xie et al., 2008; Sun et al., 2008; Min et al., 2008). Such coatings are used in glass modules for photovoltaic applications to enhance its efficiency by repelling the dust and dirt molecules and transmitting almost all the light incident on it.

As the demand for multi-functional materials with special wettability is increasing, currently, many researchers and engineers are interested in designing and fabricating superoleophobic surfaces that have a broad range of applications. Superoleophobic surfaces, both in air and in water, including anti-oil ability, (Pan et al., 2014; Liu and Jiang, 2011; Liu et al., 2015) self-cleaning, (Wu et al., 2011; Zhang et al., 2015; Artus, et al., 2006), oil/water separation, (Xue et al., 2014; Wen et al., 2015; Bixler and Bhushan, 2014; Zheng et al., 2010; Zhao and Law, 2012; Su et al., 2016; oil droplet manipulation, (Wu et al., 2011; Zhang et al., 2015; Yong et al., 2014; Zhang et al., 2013; Kavalenka et al., 2014; Zhang et al., 2012) chemical shielding, (Pan et al., 2014) anti-blocking, (Wu et al., 2011; Yong et al., 2014) liquid microlens array, (Lopes et al., 2013) oil capture, (Cui et al., 2011) bioadhesion, (Su et al., 2016) guiding the movement of an oil droplet, (Kavalenka et al., 2014; Ragesh et al., 2014) and floating on oil (Brown, et al., 2014; Ge et al., 2015).

In nature, the lotus leaf can float stably on the water surface, even with a heavy frog resting on it. The lotus leaf self-cleaning ability, but

also enhances its loading capacity; i.e., it is the superhydrophobicity of the upper surface that endows the lotus leaf with a very large loading capacity (Yong et al., 2014). The former keeps the lotus leaf clean, while the latter lets the lotus leaf floating on the water surface and its upper surface always faces the sky. Both effects benefit its growth by allowing it to receive more sunlight and maximizing photosynthesis.

5. Conclusions

In this study, recent researches and developments of self-cleaning surfaces and their applications have been presented. The attractive properties of self-cleaning surfaces, such as freezing time delay, ice-accumulation preventing, reducing ice adhesion strength, are discussed. Durability is one of the most important factors that determine the practical application of self-cleaning surfaces, which are influenced by many factors, e.g., temperature and corrosivity. Self-cleaning materials can find many applications in industries, e.g., using superhydrophobic surface to retard the frost or ice formation on the surfaces of heat exchangers and prolong the duration of the ice slurry generation, using self-cleaning surface to enhance the heat transfer performances of boiling and condensation, using superhydrophobic/superhydrophilic surfaces for drag reduction, and so on. Such applications are of positive significance for energy-saving and performance improvement. Although self-cleaning surfaces have been subjected to intensive investigations, it is apparent that further investigations are still necessary for both fundamental and applicational aspects, for examples, the fabrication process of superhydrophobic surface needs to be simplified; the durability and robustness are necessary to be improved for the practical applications; the fluid flow and heat transfer characteristics and mechanisms on superhydrophobic/ superhydrophilic surfaces or in the channels with self-cleaning surfaces are different from those for normal surfaces and both experimental and theoretical research are indispensable.

Smart self-cleaning surfaces are those which respond to external influences such as electric field, temperature, light, etc. Researchers are inspired by nature’s boundless kaleidoscopic effects and they try to biomimic them to create artificial structures almost close to nature’s phenomenon. Self-cleaning surfaces basically comprise of hydrophobic and hydrophilic surfaces. It is already being reflected in our daily life like the silver nano-coated clothes, waterproof paints, shoes, umbrellas, etc. Potential coatings that possess various real applications such as oleophobic surfaces, amphiphobic surfaces, and multifunctional surfaces have also been studied. The multifunctional surface is an open area where further research can be motivated. It will find immense applications in the

glass industry, medical field (drug-targeting, self-healing), solar cells, etc. New synthesis and surface modification routes need to be developed which can provide excellent adhesion and strength for the surfaces on the substrates used. Other areas of investigation will probably be the study of the toxicity of such surfaces, so that it can be applied safely in real applications like water purification membranes, self-repair-, self-healing and self-lubricating coatings, etc. Even though a large research focus is going in for the fabrication of such coatings, these synthesis routes need to be developed which are cost-effective but without compromising the quality.

Acknowledgments

This study is part of the project (2020-3139) supported by the Research Fund of Eskişehir Osmangazi University.

References

Artus, G.R.J., Jung, S., Zimmermann, J., Gautschi, H. P., Marquardt, K., Seeger, S., (2006), Silicone nanofilaments and their application as superhydrophobic coatings, *Advanced Materials*, 18, 2758-2762.

Bixler G.D., Bhushan B., (2014), Rice- and butterfly-wing effect inspired self-cleaning and low drag micro/nanopatterned surfaces in water, oil, and air flow, *Nanoscale*. 2014, 6, 76-96.

Blossey, R., (2003), Self-cleaning Surfaces-Virtual Realities. *Nature Materials*, 2, 5, 301-306.

Brown, P.S., Atkinson, O.D.L.A., Badyal, J.P.S., (2014), Ultrafast oleophobic-hydrophilic switching surfaces for antifogging, self-cleaning, and oil-water separation, *ACS Applied Materials & Interfaces*, 6, 7504-7511.

Cassar, L., Pepe, C., Pimpinelli, N., Tognon, G., Guerrini, G.L., Amadelli, R., (2003), White cement for architecture concrete, possessing the photocatalytic properties, in: *Proceedings of the 11th International Congress on the Chemistry of Cement*, Durban, 2003, pp.2012-2021.

Choi S.J., Huh S.Y., (2010), Direct structuring of a biomimetic anti-reflective, selfcleaning surface for light harvesting in organic solar cells. *Macromolecules Rapid Communication*, 31(6), 539-544.

Cui, J.P., Zhou, F., Wang, Q.H., Wu, D., Li, D.H., (2011) Transflective blue phase liquid crystal display using an etched in-plane switching structure, *Journal of Display Technology*, 7(7), 398-401.

Darmanin, T., Guittard, F., (2015), Superhydrophobic and superoleophobic properties in nature**,** *Materials Today,* 18(5*),* 273-285.

Dingremont, N., Bergmann, E., Collignon, P., Michael, H., (1995), Optimization of duplex coatings built from nitriding and ion plating with continuous and discontinuous operation for construction and hot working steels, *Surface Coatings Technology*, 1995, 72(3), 163-168.

Feng, L., Li, S., Li, Y., Li, H., Zhang, L., Zhai, J., Song, Y., Liu, B., Jiang, L., Zhu, D., (2002) Super-hydrophobic surfaces: from natural to artificial, *Advanved Materials, 14*, 1857-1860.

Feng, L., Zhang, Y., Xi, J., Zhu, Y., Wang, N., Xia, F., Jiang, L., (2008), Petal effect: a superhydrophobic state with high adhesive force, *Langmuir,* 24, 4114-4119.

Feng, X., Feng, L., Jin, M., Zhai, J., Jiang, L., Zhu, D., (2004), Reversible Super-hydrophobicity to Super-hydrophilicity Transition of Aligned ZnO Nanorod Films, *Journal of American Chemical Society,* 126(1), 62-63.

Fürstner, R., Barthlott, W., Neinhuius, C., Walzel, P., (2005), Wetting and self-cleaning properties of artificial superhydrophobic surfaces, *Langmuir*, 21, 956-961.

Ge, D., Yang, L., Wang, C., Lee, E., Zhang Y., Yang, S., (2015), A multi-functional oil-water separator from a selectively pre-wetted superamphiphobic paper, *Chemical Communication*, 51, 6149-6152.

Gao X., Jiang L., (2004), Biophysics: water-repellent legs of water striders, *Nature*, 432, 36-37.

Gao, X., Yan, X., Yao, X., Xu, L., Zhang, K., Zhang, J., Yang, B., Jiang, L., (2007), The Dry-Style Antifogging Properties of Mosquito Compound Eyes and Artificial Analogues Prepared by Soft Lithography, *Advanced Materials,* 19(17), 2213-2217.

Hu, D.L., Chan B., Bush, J.W.M., (2003), The hydrodynamics of water strider locomotion, *Nature, 424*, 663-666.

Huang, Y.F., Huang, C., Zhong, Y.L., Yi, S.P., (2013), Preparing superhydrophobic surfaces with very low contact angle hysteresis, *Surface Engeneering*, 2013, 29(8), 633-636.

Huovinen, E., Hirvi, J., Suvanto, M., Pakkanen, T.A., (2012), Micro-micro hierarchy replacing micro-nano hierarchy: a precisely controlled way to produce wear-resistant superhydrophobic polymer surfaces, *Langmuir*, 2012, 28 (41), 14747-14755.

Howarter, J.A, Youngblood, J.P., (2007), Self-Cleaning and Anti-Fog Surfaces via Stimuli-Responsive Polymer Brushes, *Advanved Materials*, 19(22), 3838-3843.

Howarter, J.A., Youngblood, J.P., (2008), Self-Cleaning and Next Generation Anti-Fog Surfaces and Coatings, *Macromolecules Rapid Communication*, 29(6), 455-466.

Kavalenka, M.N., Hopf, A., Schneider, M., Worgull, M., Hölscher, H., (2014), Wood-based microhaired superhydrophobic and underwater superoleophobic surfaces for oil/water separation, *RSC Advances*, 4, 31079-31083.

Lafuma, A., Quere, D., (2003), Superhydrophobic States, *Nature Materials*, 2, 457-460.

Lee, W., Jin M. K., Yoo, W. C., Lee, J. K., (2004), Nanostructuring of a polymeric substrate with well-defined nanometer-scale topography and tailored wettability, *Langmuir*, 20 (18), 7665-7669.

Lee, H., Dellatore, S.M., Miller, W.M., Messersmith, P.B., (2007), Mussel-inspired surface chemistry for multifunctional coatings, *Science*, 318, 426-430.

Liu, K., Yao, X., Jiang, L., (2010), Recent developments in bio-inspired special wettability, *Chemical Society Review*, 39(10), 3240-3255.

Liu K, Jiang L., (2011), Bio-inspired design of multiscale structures for function integration, *Nano Today*, 6, 155-175.

Liu, K., Tian, Y., Jiang, L., (2013), Bio-inspired superoleophobic and smart materials: design, fabrication, and application. *Progrees Material Science*, 58(4), 503-564.

Liu, M., Wang, S., Wei, Z., Song, Y., Jiang, L., (2009), Bioinspired design of a superoleophobic and low adhesive water/solid interface, *Advanved Materials*, 21(6), 665-669.

Liu, M., Zheng, Y., Zhai, J., Jiang, L., (2010), Bioinspired super-antiwetting interfaces with special liquid-solid adhesion, *Accounts of Chemical Research*, 43(3), 368-377.

Liu S., Liu X., Latthe, S.S., Gao L., An S., Yoon S.S., Liu B., Xing R., (2015) Self-cleaning transparent superhydrophobic coatings through simple sol-gel processing of fluoroalkylsilane. *Applied Surface Science*, 351, 897-903.

Lopes, D. M., Ramos, S. M. M., Oliveira, L. R., Mombach, J. C. M. (2013), Cassie-Baxter to Wenzel state wetting transition: a 2D numerical simulation. *RSC Advances*, 3, 24530-24534.

Mazumder, P., Jiang, Y., Baker, D., Carrilero, A., Tulli, D., Infante, D., Hunt A.T., Pruneri, V., (2014), Superomniphobic, transparent, and antireflection surfaces based on hierarchical nanostructures, *Nano Letters*, 14, 4677-4681.

Min, W.L., Jiang B., Jiang, P., (2008), Bioinspired self-cleaning antireflection coatings, *Advanced Materials*, 20, 3914-3918.

Nakajima A., Hashimoto K., Watanabe T., (2000), Transparent superhydrophobic thin films with self-cleaning properties, *Langmuir*, 16, 7044-7047.

Nishimoto S., Bhushan, B., (2013) Bioinspired self-cleaning surfaces with superhydrophobicity, superoleophobicity, and superhydrophilicity, *RSC Advances*, 3, 671-690.

Pan, S., Guo R., Xu, W., (2014) Durable superoleophobic fabric surfaces with counterintuitive superwettability for polar solvents, *AIChE Journal*, 60(8), 2752-2756.

Park Y.B., Im, H., Im, M., Choi Y.K., (2011), Self-cleaning effect of highly water-repellent microshell structures for solar cell applications, *Journal of Materials Chemistry*, 21(3), 633-636.

Parker, A.R., Lawrence, C.R., (2001), Water capture by a desert beetle, *Nature*, 414, 33-34.

Ragesh, P., Ganesh, V.A., Naira, S.V., Nair, A.S., (2014) A review on 'self-cleaning and multifunctional materials', *Journal of Materials Chemistry A*, 2(36), 14773-14797.

Su, B., Tian, Y., Jiang, L., (2016), Bioinspired Interfaces with Superwettability: From Materials to Chemistry, *Journal of American Chemical Society*, 138(6), 1727-1748.

Sun, C.H., Gonzalez, A., Linn, N. C., Jiang P., Jiang, B., (2008), Templated biomimetic multifunctional coatings, *Applied Physics Letters*, 92, 051107(1-3).

Tian, Y., Su, B., Jiang, L., (2014), Interfaces: Interfacial Material System Exhibiting Superwettability, *Advanced Materials*, 26(40), 6872-6872.

Wei, Q., Zhang, F., Li, J., Li, B., Zhao, C., (2010), Oxidant-induced dopamine polymerization for multifunctional coatings, *Polymer Chemistry*, 1, 1430-1433.

Wen, L., Tian, Y., Jiang, L., (2015), Bioinspired Super-Wettability from Fundamental Research to Practical Applications, *Angewande Chemie International Edition*, 54(11), 3387-3389.

Wu, D., Wu, S.Z., Chen, Q.D., Zhao, S., Zhang, H., Jiao, J., Piersol, J.A., Wang, J.N., Sun H.B., Jiang, L., (2011), Facile creation of hierarchical PDMS microstructures with extreme underwater superoleophobicity for anti-oil application in microfluidic channels, *Lab on a Chip*, 11, 3873-3879.

Xie, G.Y., Zhang, G.M., Lin, F., Zhang, J., Liu Z.F., Mu, S.C., (2008), The fabrication of subwavelength anti-reflective nanostructures using a bio-template, *Nanotechnology*, 2008, 19, 095605 (1-5).

Xue, Z., Cao, Y., Liu, N., L. Feng L., Jiang, L., (2014), Special wettable materials for oil/water separation, *Journal of Materials Chemistry A*, 2, 2445-2460.

Yang, J., Zhang, Z., Xu, X., Zhu, X., Men, X., Zhou, X., (2012), Superhydrophilic-superoleophobic coatings, *Journal of Materials Chemistry*, 22, 2834-2837.

Yao, X., Song, Y., Jiang, L., (2011), Applications of Bio-Inspired Special Wettable Surfaces, *Advanced Materials*, 23(6), 719-734.

Yong, J.L., Yang, Q., Chen, F., Zhang, D., Farooq, U., Du, G., Hou, X., (2014), A simple way to achieve superhydrophobicity, controllable water adhesion, anisotropic sliding, and anisotropic wetting based on femtosecond-laser-induced line-patterned surfaces, *Journal of Materials Chemistry A*, 2, 5499-5507.

Yong, J.L., Chen, F., Yang, Q., Hou, X., (2015), Femtosecond laser controlled wettability of solid surfaces, *Soft Matter*, 11, 8897-8906.

Zhang, E., Cheng, Z., Lv, T., Li, L., Liu, Y., (2015), The design of underwater superoleophobic Ni/NiO microstructures with tunable oil adhesion, *Nanoscale*, 7, 19293-19299.

Zhang, G. M., Zhang, J., Xie, G.Y., Liu, Z.F., Shao, H.B., (2006), Cicada wings: a stamp from nature for nanoimprint lithography, *Small*, 2, 1440-1443.

Zhang, X., Li, Z., Liu K., Jiang, L., (2013), Bioinspired multifunctional foam with self-cleaning and oil/water separation, *Advanced Functional Materials*, 23(22), 2881-2886.

Zhang, Y., Chen, Y., Shi, L., Li J., Guo, Z., (2012) Recent progress of double-structural and functional materials with special wettability, *Journal of Materials Chemistry*, 22, 799-815.

Zhang, Y.L., Chen, Q.D., Jin, Z., Kim, E., Sun, H.B., (2012) Biomimetic graphene films and their properties, *Nanoscale*, 4(16), 4858-4869.

Zhang, Y.L., Xia, H., Kim E., Sun, H.B., (2012), Recent developments in superhydrophobic surfaces with unique structural and functional properties, *Soft Matter*, 8, 11217-11231.

Zhang, Y., Islam, N., Carbonell, R.G., Rojas, O.J., (2013), Specificity and regenerability of short peptide ligands supported on polymer layers for immunoglobulin G binding and detection, *ACS Applied Materials Interfaces*, 23, 8030-8037.

Zhao H., Law K.Y. (2012), Directional self-cleaning superoleophobic surface. *Langmuir*, 28(32), 11812-11818.

Zheng, Y., Guo, X., Jiang, L., (2007), Directional adhesion of superhydrophobic butterfly wings, *Soft Matter*, 3, 178-182.

Zheng, J.Y., Feng, J., Zhong, M.Q., (2010), Fabricating superhrdrophilic/ superhydrophobic surfaces bu replica/molding method using $CaCO_3$ particles as, *Acta Polymerica Sinica*, 10, 1186-2911.

Zorba, V., Stratakis, E., Barberoglou, M., Spanakis, E., Tzanetakis, P., Anastasiadis, S.H., Fotakis, C., (2008), Biomimetic Artificial Surfaces Quantitatively Reproduce the Water Repellency of a Lotus Leaf, *Advanved Materials*, 20(21), 4049-4054.

CHAPTER III

THERMAL AND STRUCTURAL ANALYSIS OF GEOPOLYMERS DERIVED FROM INDUSTRIAL WASTE MATERIALS

Ceyda BİLGİÇ

(Assoc. Prof. Dr.); Eskişehir Osmangazi University, Eskişehir, Turkey
e-mail: cbilgic@ogu.edu.tr, Orcid No: 0000-0002-9572-3863

Şafak BİLGİÇ

(Asst. Prof. Dr.); Eskişehir Osmangazi University, Eskişehir, Turkey
e-mail: safakb@ogu.edu.tr, Orcid No: 0000-0002-9336-7762

1. Introduction

Inorganic polymer concretes which are also called "geopolymers" have arisen an interest in their potential usage in the environmentally friendly construction and building industry. These materials not only result in lower greenhouse emissions but also allow the evaluation of raw clay material sources. Geopolymers display comparable properties to ordinary portland cement with their robust and versatile technology; the large scale of raw materials can be used as a source in geopolymerization so specific properties can be obtained for the desired application (Duxson et al., 2007:1590). The most commonly used application areas of geopolymers are; construction and building materials, fire resistance ceramics, composites, and matrix for immobilization of toxic wastes (Kumar and Kumar, 2013:865).

Geopolymerisation is a process in which silicon, aluminum, and oxygen atoms create a chain of SiO_4 and AlO_4 tetrahedra linked alternatively by shared oxygen atoms (Wang et al., 2005:1; Davidovits, 1991:1633). The water/solid ratio in this process, if no aggregates are used, ranges from 0.3 to 0.4 (Xu and van Deventer, 2000:247). The products are amorphous to semi-crystalline materials with superior mechanical behavior (Davidovits, 1991:1633; van Jaarsveld et al., 2002:63; Pacheco-Torgal et al., 2009:200; Tang et al., 2015:1244). The reactants used to form conventional geopolymers are usually industrial waste materials as the Al-Si source and an activator solution containing reactive silicate anions and alkali cations (Singh et al., 2004:1943). The focus of research in this field may be summarised as follows:

i) Al-Si source: identifying low-cost, readily available materials

suitable to participate in geopolymerization. It has been shown that a wide range of natural materials such as Fly ash, slag, and red mud can be used to make geopolymers.

(ii) alkali activation: analyzing the effects of pH and alkali ions on process completion and the final properties of the product, e.g. it has been shown that K-feldspars show increased dissolution in NaOH solution compared with KOH solution, and thus confer higher compressive strength (Xu and van Deventer, 2000:247).

(iii) geopolymerization: the mechanisms of the reaction have yet to be fully understood; the parameters affecting the process, microstructural reorganization of the source materials, and the reaction steps have been studied extensively by analytical methods.

The unique properties of geopolymers - high early strength, extraordinary durability, resistance to chemical attack, ability to immobilize toxic atoms, and environmental benefits such as low energy consumption and carbon dioxide emission in production - make geopolymers a strategic material for sustainable development and a serious alternative to Portland cement.

Understanding the structure of geopolymers is critical for designing geopolymers with desired properties. Therefore, this study was undertaken to review the thermal and structural analysis of the geopolymers, obtained from the industrial wastes. The samples of industrial waste and the synthesized geopolymers were characterized by X-Ray Fluorescence (XRF) for the chemical composition of materials. X-Ray Diffraction (XRD) measurements are performed to investigate the amorphous or crystalline phase of the synthesized geopolymers. Fourier Transform Infrared spectroscopy (FTIR) spectroscopy is utilized to understand the vibrational fingerprints of geopolymers, Scanning Electron Microscopy (SEM) images are performed on the synthesized geopolymers to resolve their surface microstructures. The thermal degradation and stability of the materials were studied using thermogravimetric analysis (TGA) and derivative thermogravimetric analysis (DTG) at several heating rates. The relationships established between the structure and physical properties will be important for controlling product properties.

2. Analysis of Geopolymers

2.1. X-Ray Fluorescent (XRF) analysis of geopolymers

X-ray fluorescent (XRF) analysis was carried out to determine the chemical composition of various binders used in the study of geopolymer

and the comparison among the chemical composition of binders can be seen. Materials such as fly ash, bottom ash, silica fume, rice husk ash, and others have shown a fair amount of silica and alumina content, which is suitable to be a substitute as supplementary cementitious materials. The major oxides present in most of the fly ash samples were mostly silicon oxide and aluminum oxide. Because ordinary Portland cement was processed from limestone, it has a higher content in calcium oxide and silicon oxide but lowers in aluminum oxide. As stated in ASTM C-618, ashes can be categorized into classes N, F, and C based on the pozzolanic oxides, namely SiO_2, Al_2O_3, and Fe_2O_3. According to the listed previous studies, only ground granulated blast furnace slag and sepiolite contain less than 50% of pozzolanic oxides. In general, fly ash studied in previous works fall in class F, which has at least 70% of pozzolanic oxides except for Abdulkareem et al. (2014) and Embong et al. (2016). Both studies used Fly ash sourced from the Manjung power plant, Malaysia which is categorized in class C (Abdulkareem et al., 2014:377; Embong et al., 2016:816).

2.2. X-Ray Diffraction (XRD) of geopolymers

XRD plays a crucial role in the characterization of geopolymers by providing information on the crystalline phases and amorphous character of the samples. Geopolymers are completely amorphous according to X-ray diffraction (XRD). Typically, they possess a diffuse halo peak at about 27-30^o 2θ (Davidovits, 1991:1633; Lecomte et al., 2003:2571; Lizcano et al., 2012:2607; Zhang et al., 2005:23). The broad diffuse hump is corresponding to the amorphous aluminosilicates which form the primary binder phase in the geopolymer matrix and contribute to the strength of geopolymers. The angle of this diffuse halo is dependent on the Si/Al ratio. Increasing Si/Al ratio lowers the degree of the hump (Lizcano et al., 2012:2607).

The study of geopolymers using X-ray diffraction is difficult because of the fact, a large part of the structure is amorphous content between 20^o and 40^o 2θ. The degree of disorder in geopolymers can be inferred by the way it diffracts X-ray to form a diffraction pattern. In a non-crystalline state, diffraction of X-ray results in a broad diffuse halo rather than sharp diffraction peaks (Davidovits, 1991:1633; Rees et al., 2007:9076). Peaks were of quartz, mullite, and hematite of the crystalline component of the fly ash. The broad peak in region 20-30^o 2θ arises from the glassy phase of fly ash and peaks in the region 6-10^o and 16^o 2θ arise from the alumino-silicate gel. A considerable amount of zeolites were found in cement-fly ash system blend, activated by the highly alkaline multi-compound activator, around pH 14 and cured at 70 ^{o}C (Bakharev et al.,

2005:1244).

The microstructure of the alkali-activated fly ash changes with the chemical composition (Rowles et al. 2007:663). After geopolymerization, all the main characteristic peaks of Al-Si minerals remained but decreased slightly. This suggested that the Al-Si mineral did not dissolve totally into the gel phase. However, there were no new peaks, which means that no new major crystalline phases were formed (Xu and van Deventer, 2000:247). The baseline broadened between 20^{o} and 40^{o} 2θ was an indication of an increased amorphicity (van Jaarsveld et al., 2002:63). Palomo et al. (2014) studied a series of fly ash samples activated under different experimental conditions and concluded that geopolymers are a family of materials with the same basic chemical composition but potentially different microstructures (Palomo et al., 2014:1). The structural properties of geopolymers depend strongly on many factors including raw material selection, synthesis conditions, thermal treatment temperatures, and durations following synthesis and etc. The phase's composition and pore structure were characterized by XRD and SEM.

Abdulkareem et al. (2014), reported a broad hump from 20^{o} to 35^{o} indicating the presence of amorphous geopolymer products (Abdulkareem et al., 2014:377). Based on previous studies, the presence of quartz and mullite reflected the composition of typical fly ash. More than half of the fly ash was composed of iron and calcium. Thus, it explained the crystalline phases present in the geopolymer paste pattern. The comparison of the cement-based control sample (CC) with geopolymer concrete- without the addition of nano-silica shows a wide hump around 25^{o} to 35^{o} in geopolymer concrete with nano-silica. The intensity of quartz, mullite, and hematite was found higher in geopolymer concrete with nano-silica due to the presence of additional nano-silica in the matrix. Some extra peaks are shown in nano-silica modified geopolymer concrete which indicates the formation of the new phases of quartz (SiO_2), albite ($NaAlSi_3O_8$), kaolinite ($Al_2Si_2O_5(OH)_4$), alite (Ca_3SiO_5), mullite ($3Al_2O_3{\cdot}2SiO_2$), and $Ca(OH)_2$ crystalline compound compared to the geopolymer concrete- without the addition of nano-silica and cement-based control sample. The wide diffraction hump was detected around $2\theta = 25^{o}$-35^{o} which confirmed the presence of crystalline phases in geopolymer concrete with nano-silica. As discussed earlier, crystalline phases were exposed after the addition of alkaline solution. Zeolite was formed after the dissolution while mullite, quartz, and hematite exist in all fly ashes.

Tho-In et al. (2018) reported the XRD analysis at the age of 7-day of Fly ash-based geopolymer paste with ground container glass (Tho-In et al., 2018:2892). The Fly ash-based geopolymer paste has a wide hump at 25^{o} to 35^{o} and low phases of calcite that corresponds to the high degree of geopolymerization (Phoo-ngernkham et al., 2014:58). The XRD trends of Fly ash-based geopolymer paste with ground container glass pastes are similar to that of Fly ash geopolymer paste. However, peaks of quartz and calcite were observed as the percentage of ground container glass increased due to the high contents of SiO_2 and CaO (Wongsa et al., 2017:49). Peaks of cristobalite and tridymite were noted at a higher percentage with ground container glass replacement.

Ground granulated blast furnace slag-based geopolymer represented the development of phases of geopolymer from early age to long-term specimen. The high-intensity peak, 2θ for 28 days geopolymer paste is reported at 27^{o}. Many minerals from bauxite ore tailing such as corundum, muscovite, anatase, quartz, and mullite are still identified for the long-term specimen. However, the formation of calcite mineral is detected in the long-term specimens which hinted the specimen is susceptible to carbonation (Ye et al., 2017:23).

The chemical composition of geopolymer is similar to zeolitic materials. Sometimes, geopolymers are regarded as a zeolitic precursor. The difference between geopolymers and zeolites is that geopolymer is amorphous, whereas zeolite is crystalline in nature (Lecomte et al., 2003:2571; Khale and Chaudhary, 2007:729). Crystallization does not only depend on curing temperature but also influenced by the type of alkali reactant used and curing time. Zeolite crystallization is promoted by high water content, high curing temperature as well as extended curing period (Provis et al., 2005:3075). Zeolite crystallites are also increasing with aging (Duxson et al., 2007:8).

It is known that zeolites are highly porous and have poor mechanical properties. It was believed that there is always a limitation of the amount of crystalline phase that can be tolerated by the matrix. Several researchers (Kolousek et al., 2007:9267; Palomo et al., 1999:997) discovered that zeolite crystallites reinforce the geopolymer matrix and improve strength, but it will cause a substantial reduction in long-term strength. A similar strength development trend has been concluded for fly ash geopolymers (Criado et al., 2007:671).

2.3. Scanning Electron Microscope (SEM) of geopolymers

Scanning Electron Microscopy (SEM) can be used to study the morphology of raw materials and synthesized of raw material-based

geopolymers. Micromorphologies of geopolymers, fast and non-destructive technique gives information about surface properties, particle size and also particle distribution (Yunsheng et al., 2010:271). Differ from metakaolin geopolymers; fly ash geopolymers reveal heterogeneous elements with lots of unreacted fly ash particles in the hollow cavities left by the partially dissolved fly ash particles. Unreacted particles act as a filler and strengthen the composite. In fly ash geopolymers, smooth and connecting geopolymer matrix was observed instead of a globular unit of geopolymer matrix in metakaolin geopolymers.

Many researchers reported on fly ash-based geopolymer concrete with variables that include additional binders, alkali activator ratio, molarity, and curing temperature & duration (Assi et al., 2016:806; Pavithra et al., 2016:117; Xie and Ozbakkaloglu, 2015:5945). Pavithra et al. (2016) researched fly ash-based geopolymer concrete and suggested a method as explained here to obtain optimum mix design (Pavithra et al., 2016:117). A few parameters such as molarity, sodium silicate to sodium hydroxide ratio (SS/SH), curing temperature, and duration was set as constant variables before deciding for the alkaline activator solution (AAS). In this study, the authors suggested that the water content to be used relied on the maximum aggregate size, as it can be used to control the limit of maximum water content. Calculation on binder content, alkaline activator solution, water content, the fine, and coarse aggregate was carried out based on the priority of the mix whether strength or alkaline activator solution to binder ratio is to be focused on. The effect of different alkaline solution-to-binder contents on the microstructure of geopolymer concrete was compared. The precipitation decreases constantly as the ratio of alkaline activator solution /binder increases. It is understood that as this ratio increases, the strength of geopolymer concrete decreases due to the increasing amount of water present in the geopolymer mix. This phenomenon is comparable with ordinary Portland cement concretes with a higher water/cement ratio. The contact area for the reaction was blocked by the water molecules and this, in turn, affected the geopolymerization process between the binder and the activator; this resulted in low compressive strength of geopolymer concrete (He et al., 2011:59). With appropriate alkali activator/binder ratios of 0.4 and 0.5, the unreacted Fly ash particles were found minimum. Also, the number of voids is sparse. The fineness of fly ash also contributed to the dense matrix, which helps reduce the formation of microcracks. Apart from that, the strength of geopolymers was improved fairly due to the ability of fly ash to fill the microcracks, which is in line with the study of Xie and Ozbakkaloglu (2015) and Assi et al. (2016) (Assi et al., 2016:806; Xie and Ozbakkaloglu, 2015:5945).

The effect of different mass ratios of sodium silicate to sodium hydroxide of fly ash-based geopolymer was studied through micro-structural investigation by Abdulkareem and Ramli (2015) (Abdulkareem and Ramli, 2015:61). Fully reacted fly ash was observed for geopolymer with alkaline activator mass ratios of 0.5 and 1.0. Even though a similar microstructure was observed for both mass ratios of 0.5 and 1.0, the compressive strength obtained for the mass ratio of 1.0 was 65 MPa compared to 35 MPa for the mass ratio of 0.5. Supported by the previous study, a higher concentration of silicate might contribute to higher strength development due to more silicates available for geopolymerization (Palomo et al., 1999:1323). However, the comparison shows that a higher mass ratio of sodium silicate resulted in unreacted fly ash particles. The use of activator mass ratios of 2.0 and 3.0 displayed high content of unreacted and partially reacted fly ash microspheres. It is understood that too much alkaline activator solution in the mix hampered the process of geopolymerization by limiting the interaction between the binder and alkaline activator solution (Villa et al., 2010:2084). Besides, geopolymer samples with SS/SH mass ratio of 3.0 recorded the weakest compressive strength of 32 MPa. The comparison of recent studies on this subject shows that most of the authors used the mass ratio of SS/SH up to 2.5 (Okoye et al., 2016:3000; Xie and Ozbakkaloglu, 2015:5945; Noushini et al., 2016:136). While another study has produced similar properties of geopolymer with a higher mass ratio of alkaline solution, the curing temperature might have been contributed to the dense structure (Gunasekara et al., 2016:352). Curing temperature of 70 ^{o}C or higher tends to have a looser arrangement due to evaporation of free water which causes continuous microcracks within the matrix; (Kong and Sanjayan, 2010:334; Chindaprasirt et al., 2007:224). According to Chindaprasirt et al. (2007), an adequate amount of water is necessary for the process of geopolymerization to have high strength development (Chindaprasirt et al., 2007:224). Okoye et al. (2016) examined the microstructure of geopolymer made of fly ash and silica fume (Okoye et al., 2016:3000). In contrast with previous studies, a geopolymer concrete sample with fly ash was found to have a fracture surface. The observation of voids proved a loose arrangement of particles. Whereas smoother surface was observed for the 20 % replacement of fly ash with silica fume in the fly ash-based geopolymer concrete.

SEM images of pure geopolymer and geopolymer nanocomposites containing 3.0 wt% nano-silica in wet and dry mix conditions. A significant amount of unreacted and partially reacted fly ash particles was observed in the case of pure geopolymer. However, the number of unreacted particles decreased. Besides, microcracks observed using the

dry mix procedure, are lower than the pure geopolymer and wet mix. Unlike Pavithra et al. (2016), the microstructure of bottom ash and fly ash in geopolymer was studied by Xie and Ozbakkaloglu (2015) (Pavithra et al., 2016:117; Xie and Ozbakkaloglu, 2015:5945). As the mass ratio of fly ash to bottom ash increases, the strength of the sample increases, too. The presence of bottom ash, however, reduced the strength of geopolymer and it could be attributed to the larger surface area of bottom ash with the presence of foreign objects that failed to react fully in the geopolymer.

A small number of semi-spheres was present along with some rectangular-shaped objects. While the composition test revealed the presence of foreign object-radium, a radioactive earth metal in the bottom ash, there were no foreign objects nor irregular-shaped particles found in fly ash. Other than the presence of foreign objects, some of the bottom ash did not react fully in the process of geopolymerization and this contributed to lower compressive strength compared to pure fly ash-based geopolymer. Similar to previous studies, unreacted Fly ash residues were observed that only small traces of sodium element were observed on the non-reactive minerals covering the unreacted Fly ash particles (Xie and Ozbakkaloglu, 2015:5945; Embong et al., 2016:816). Due to the low calcium content present in Gaston Fly Ash, insignificant amount of calcium element, SEM image illustrated that crystalline phases were exposed, and new precipitant was formed after the dissolution of Gaston Fly Ash using an alkaline solution. After the dissolution, parts A, B, and C correspond to zeolite, mullite, and hematite (Zeng and Wang, 2016:386).

Sharmin et al. (2017) has utilized a high volume of ground granulated blast furnace slag (GGBS) along with metakaolin (MK) and rice husk ash (RHA). A continuous compact microstructure is observed for the optimum mix (0.25:0.25:0.50 for MK: RHA: GGBS). It is understood that mixes with high volume GGBS used to replace RHA, has subsequently improved the compressive strength. Utilize high volume of RHA is known for geopolymer with lower compressive strength and more brittle due to the larger solid particle and lower specific gravity of RHA (Chindaprasirt et al., 2007:224; Sharmin et al., 2017:608).

Additional MK in geopolymer was able to contribute stronger Si-O-Al and Al-O-Al bonds than the Si-O-Si bond. However, the utilization of a high volume of MK is not advisable as it will produce sodium alumina silicate (zeolite) (Duxson et al., 2005:47). Zeolite is known for its negative effect on strength development as a result of excess alumina from MK. Subsequently, the process of polymerization is hindered as a

high concentration of the alkaline activated solution was required to activate a high volume of MK. Thus, the usage of MK in geopolymer needs appropriate consideration for achieving desired results. Ye et al. (2017) studied the early age and long-term microstructure of bauxite ore tailing and slag-based geopolymer paste. The microstructure of 28-days where porous gel with noticeable large pores was observed. It was predicted that the continuous geopolymerization process has been able to produce the gels where large pores tend to reduce in small and volume for a long-term specimen. The linking of geopolymer gels has formed capillary gels in pores and cracks (Ye et al., 2017:23).

Structural characterization was also performed using Scanning Electron Microscopy with Energy Dispersive X-Ray (SEM-EDX) analysis. In addition to SEM micrographs and EDX spectroscopies, an elemental mapping was done to some of the samples of the 1st category to inspect the effect of the studied parameters on the elemental distribution of the manufactured samples and thereby obtain an evaluation of the matrix through the ratios of the elements. The elemental mapping revealed the fact that in general a homogeneous distribution of the elements was observed. The observations are considered in line with the obtained results and the micrographs of the samples.

The SEM micrographs and the EDX spectroscopies of the main mixes were taken. As a general observation, the micrographs of the investigated samples indicate a satisfactory degree of compactness and good microstructural bonding between the components of the geopolymeric matrix. Some unreacted fly particles were observed in the micrographs, the existence of unreacted particles is an indicator of a good strength behavior because these particles will affect positively the bonding pattern of the manufactured samples (Sung et al., 2013:409).

2.4. Fourier Transform Infrared Spectroscopy (FTIR) of geopolymers

FTIR spectra of geopolymers is generally characterized by broadband in the 900-1300 cm^{-1} region that is characteristic of disordered geopolymer structure. Bands observed in this region are related to asymmetric stretching vibrations of Si–O–T (T=Al, Si) (Ye et al., 2014:1652; Arıöz et al., 2012:1115). The shift of this band to lower wavenumbers is a clear indication of the dissolution of the raw materials in an alkaline activator and the evolution of a new amorphous aluminosilicate phase during the geopolymerization process. Similar results are obtained in the study where FTIR spectroscopy is performed on fly ash-based geopolymers. FTIR band detected at 1085 cm^{-1} in fly ash has shifted to lower frequencies (986 cm^{-1}) with alkaline activation (Arıöz

et al., 2012:1115). Bands detected in the region between 550 - 750 cm^{-1} are assigned to symmetric stretching vibrations of Si–O–Si and Al–O–Si. An enhancement in the intensity of the bands in this region points out an enhancement in chain length and formation of aluminosilicate gel. High-frequency bands observed in the region between 1300-1600 cm^{-1} are assigned to stretching vibrations of O–C–O bonds and show the presence of carbonate materials (Ye et al., 2014:1652; Dimas et al., 2009:211; Mustafa Al Bakri et al., 2011:289). In a recent study, red mud is used together with fly ash as a raw material for geopolymer production, and a peak is detected at 458 cm^{-1} (Kumar and Kumar, 2013:865), this peak is associated with vibrations of Fe–O bonds (Muñiz-Villarreal et al., 2011:995) because of the iron present in red mud. Band detected at frequencies higher than 1600 cm^{-1} is due to stretching (–OH) and bending (H–O–H) vibrations of interlayer adsorbed H_2O molecules (Nath and Kumar, 2013:924; Mustafa Al Bakri et al., 2011:289). In a recent research employing fly ash and bottom fly ash in geopolymer production, FTIR spectra of raw materials and products are used to quantitively express the degree of geopolymerization. This calculation is made in terms of height ratios and area ratios of the Si–O–Si stretching peaks that exist in the FTIR spectra of geopolymers to their regarding ashes' peak. It is found in this study that the ratios of peak heights and areas to their corresponding ashes are much higher and this situation points out the high degree of geopolymerization in the system (Ferone et al., 2013:1920).

A FTIR analysis for Fly ash-based geopolymer was carried out by Adak et al. (2017) to determine the structure of geopolymer (Adak et al., 2017:430). The distinct intensity band near 460 cm^{-1} was recognized for the Si–O–Si bending vibration. The band between 750 cm^{-1} and 800 cm^{-1} was observed due to the AlO_4 vibration. Another peak for the asymmetric stretching and vibration band of Si–O–T (T = Al, Si) which was described as the strongest band, registered in the region of 950 cm^{-1} -1050 cm^{-1}. The position (1420 cm^{-1}) of Si–O–Si in with geopolymer concrete- without the addition of nano-silica was shifted to the right position (1485 cm^{-1}) in geopolymer concrete with nano-silica. A significant band was also located at approximately 3450 cm^{-1} for OH stretching bonding.

Tho-In et al. (2018) conducted the FTIR analysis on Fly ash-based geopolymer with ground fluorescent lamp (FP) and container glass pastes (Tho-In et al., 2018:2892). The absorption bands at approximately 3450 cm^{-1} and the weak band 1650 cm^{-1} are associated with the vibrations of O–H and H–O–H bonds in the water molecules. Previous studies reported that the bands as reported by Tho-In et al. (2018) revealed that the water molecules were absorbed on the surface or embedded in the pores during the process of geopolymerization (Tho-In et al., 2018:2892; Fernández-

Jiménez and Palomo, 2005:1984). The band at roughly 1450 cm^{-1} indicated the extension of O–C–O in carbonate groups due to the reaction of alkali metal hydroxides with atmospheric CO_2 (Panias et al., 2007:246). The irregular stretching of Si–O–X bonds found in all specimens is located at 1050 cm^{-1}, where X representing tetrahedral silicon or aluminum atom. The Si–O–X bond supported the geopolymerization process with the phases of amorphous aluminosilicates formed. Besides, researchers also stated that the sharp absorption band correlates to the number of tetrahedrally coordinated aluminum that exists in the geopolymer gel (Gao et al., 2014:503). Furthermore, the stretching of O–Si–O and Si–O–Si bonds which can be located at 450 cm^{-1} is identical to those Si–O–Al groups (Zawrah, et al., 2016:237).

2.5. Thermogravimetric Analysis of geopolymers

Information about the thermal stability of the samples and the weight loss versus temperature changes is measured by thermogravimetric analysis (TGA) and differential thermogravimetric analysis (DTGA). TGA is performed using TA instruments and the analysis is done by using nitrogen at a flow rate. The characteristic subsequent phases observed in the thermogravimetric analysis of geopolymers are; i) dissipation of free water molecules, ii) decomposition of geopolymer components, iii) dehydroxylation of zeolitics, iv) stabilization of the weight (Cheng et al., 2015:74).

Thermal analysis was carried out by Abdulkareem et al. (2014) to measure the mass loss as a function of temperature from 25 ^oC to 800 ^oC. Thermogravimetric analysis (TGA) and the derivative thermogravimetric analysis (DTG) curves for the geopolymer paste were displayed. Loss of water due to evaporation of both the free and some of the chemically bonded water from geopolymer was demonstrated with a decrease in mass rapidly before 150 ^oC (Abdulkareem et al., 2014:377). Roughly 55-60% of free water present in the geopolymer matrix evaporated before 100^oC in samples was illustrated by the sharp weight loss. However, it is observed that the rate of weight loss stabilized from 150°C to 780°C, on account of the evaporation of chemically bonded water and the hydroxyl groups, –OH. No further mass loss was detected with the increase of temperature to 800°C. The average mass after heated to 800°C was 79.8%.

Kong and Sanjayan (2010) analyzed the behavior of Fly ash-based geopolymer paste under elevated temperature (Kong and Sanjayan, 2010:334). Withstanding with Abdulkareem et al. (2014) the sharp weight loss came at 250^oC instead of 150^oC, which is also attributed to the

evaporation of the hydroxyl group (Abdulkareem et al., 2014:377; Duxson et al., 2005:47). The change in weight is rather constant after 300 ^{o}C. Kong and Sanjayan (2010) hypothesize that the slow rate of thermal shrinkage recorded from 300 ^{o}C and above is associated with the low rate of weight loss (Kong and Sanjayan, 2010:334). The average mass recorded after 800^{o}C exposure was 89%. Duan et al. (2016) studied the thermal analysis of geopolymer paste with iron ore tailing (IOT) (Duan et al., 2016:600). The content of calcium hydroxide $Ca(OH)_2$ decreased when the content of iron ore tailing increased, which was attributed to the lesser mass loss compared to the reference sample. It is understood that the addition of iron ore tailing contributed to the formation of calcium silicate hydrate by utilizing $Ca(OH)_2$. Nevertheless, even after 30% of iron ore tailing was added to the mix, the decomposition of $Ca(OH)_2$ recorded corresponding to the endothermic peak. It was reported that $Ca(OH)_2$ still presents as only a number of the calcium was converted into calcium silicate hydrate. Similar to Abdulkareem et al. (2014), the rate of mass loss at high temperatures after 800^{o}C was negligible for all samples (Abdulkareem et al., 2014:377). Thermal analysis was conducted by Okoye et al. (2016) to study the thermal stability of geopolymers (Okoye et al., 2016:3000). The weight loss for both kaolin incorporated Fly ash-based geopolymer and pure Fly ash-based geopolymer samples took place at approximately 100 ^{o}C. For the Fly ash-based geopolymer, a rather sharp drop in weight was observed when temperature increased whereas the kaolin incorporated -based geopolymer has a complex curve. From the observation of both samples, the ideal curing temperature could be ranged from 80^{o}C to 100^{o}C.

3. Conclusions

Innovative technology studies have started to focus on ‘geopolymers’ that are inorganic polymers that arise as potential future alternatives to cement-based materials. Geopolymer was first used as a fire-resistant to protect cruise ships from fire, in the protection of wooden structures, and different implementations. Geopolymers have also been shown to display good mechanical and thermal properties, low shrinkage, and longer design lives compared to some cementitious materials. Geopolymers, if used as an alternative to Portland cement, CO_2 emission produced by geopolymer technology is estimated to be 80% less than Portland cement. Therefore, it is thought that geopolymer technology is going to be vital in the near future for the green construction industry.

This study offers insights into the various techniques used for the characterization of geopolymers derived from industrial waste materials. Understanding the structure of geopolymers is critical for designing

geopolymers with desired properties. The relationships established between the structure and physical properties will be important for controlling product properties.

Acknowledgments

This study is part of the project (2018-2233) supported by the Research Fund of Eskişehir Osmangazi University.

References

Abdulkareem O.A., Mustafa Al Bakri A.M., Kamarudin H., Khairul Nizar I., Saif A.A., (2014) Effects of elevated temperatures on the thermal behavior and mechanical performance of fly ash geopolymer paste, mortar and lightweight concrete. *Construction and Building Materials,* 50, 377-387.

Abdulkareem, O.A., Ramli, M. Optimization of alkaline activator mixing and curing conditions for a fly ash-based geopolymer paste system, *Modern Applied Science*, 9 (12) (2015) 61-69.

Adak, D., Sarkar, M., Mandal, S. (2017) Structural performance of nano-silica modified fly-ash based geopolymer concrete, *Construction and Building Materials*, 135 (2017) 430-439.

Assi L., Ghahari S.A., Deaver E.E., Leaphart D., Ziehl P. (2016) Improvement of the early and final compressive strength of fly ash-based geopolymer concrete at ambient conditions, *Construction and Building Materials*, 123, 806-813.

Arıöz, E., Arıöz, Ö., Koçkar, Ö.M. (2012) "Leaching of F-type Fly Ash Based Geopolymers'', 20th International Congress of Chemical and Process Engineering CHISA, *Procedia Engineering*, 42, 1114-1120.

Bakharev T. (2005) "Geopolymeric materials prepared using Class F fly ash and elevated temperature curing" *Cement and Concrete Research*, 35(6),1224-1232.

Cheng, H., Lin, K.L., Cui, R., Hwang, C.L., Cheng, T.W., Chang, Y.M. (2015) "Effect of Solid-to-Liquid Ratios on the Properties of Waste Catalyst-Metakaolin Based Geopolymers", *Construction and Building Materials*, 88, 74-83.

Chindaprasirt, P., Chareerat, T., Sirivivatnanon, V. (2007) Workability and strength of coarse high calcium fly ash geopolymer, *Cement and Concrere Composites*, 29 (3), 224-229.

Criado M., Fernández-Jiménez A., de la Torre A.G., Aranda M.A.G.,

Palomo A. (2007) An XRD study of the effect of the SiO_2/Na_2O ratio on the alkali activation of fly ash, *Cement and Concrete Research*, 37(5), 671-679.

Davidovits, J. (1991) ‘‘Geopolymers: Inorganic Polymeric New Materials’’, *Journal of Thermal Analysis and Calorimetry*, 37(8), 1633-1656.

Dimas, D. D., Giannopoulou, I.P., Panias, D. (2009) ‘‘Utilization of Alumina Red Mud for Synthesis of Inorganic Polymeric Materials’’, *Mineral processing and extractive metallurgy review: An International Journal*, 30 (3), 211-239.

Duan P., Yan C., Zhou W., Luo W. (2016) Fresh properties, mechanical strength and microstructure of fly ash geopolymer paste reinforced with sawdust, *Construction and Building Materials,* 111, 600-610.

Duxson, P., Provis, J.L., Lukey, G.C., Mallicoat, S.W., Kriven, W.M., Van Deventer, J.S.J. (2005) “Understanding the Relationship Between Geopolymer Composition, Microstructure and Mechanical Properties”, *Colloids and Surfaces A: Physicochemical and Engineering Aspects*, 269 (1-3), 47-58.

Duxson P, Mallicoat, S.W., Lukey, G.C., Kriven W.M., van Deventer J. S. J. (2007), The effect of alkali and Si/Al ratio on the development of mechanical properties of metakaolin-based geopolymers, *Colloids and Surfaces A: Physicochemical and Engineering Aspects*, 292(1), 8-20.

Duxson P., Provis J.L., Lukey G.C., van Deventer J. S. J. (2007) ‘‘The Role of Inorganic Polymer Technology in the Development of 'Green Concrete'’’, *Cement and Concrete Research*, 37(12), 1590-1597.

Embong, R., Kusbiantoro, A., Shafiq, N., Nuruddin, M.F. (2016) Strength and microstructural properties of fly ash based geopolymer concrete containing highcalcium and water-absorptive aggregate, Journal of Cleaner Production, 112, 816-822.

Ferone, C., Colangelo, F., Roviello, G., Asprone, D., Menna, C., Balsamo, A., Prota, A., Cioffi, R., Manfredi, G. (2013), “Application-Oriented Chemical Optimization of a Metakaolin Based Geopolymer’’, *Materials*, *6*(5), 1920-1939.

Fernández-Jiménez, A., Palomo, A. (2005) “Composition and Microstructure of Alkali Activated Fly Ash Binder: Effect of the Activator”, *Cement and Concrete Research*, 35(10), 1984-1992.

Gao K., Lin K.L., Wang D.Y., Hwang C.L., Shiu H.S., Chang Y.M.,

Cheng T.W. (2014), Effects SiO_2/Na_2O molar ratio on mechanical properties and the microstructure of nano-SiO_2 metakaolin-based geopolymers, *Construction and Building Materials*, 53, 503-510.

Gunasekara, C., Law, D.W., Setunge, S. (2016) Long term permeation properties of different fly ash geopolymer concretes, *Construction and Building Materials*, 124, 352-362.

He P., Jia D., Wang M., Zhou Y. (2011) Thermal evolution and crystallization kinetics of potassium-based geopolymer, *Ceramics International*, 37 (1), 59-63.

Khale D., Chaudhary R. (2007) "Mechanism of geopolymerization and factors influencing its development: a review", *Journal of Materials Science*, 42, 729-746.

Kolousek D., Brus J., Urbanova M., Andertova J., Hulinsky V., Vorel J. (2007) "Preparation, structure and hydrothermal stability of alternative (sodium silicate-free) geopolymers", *Journal of Materials Science*, 42(22), 9267-9275.

Kong D.L.Y., Sanjayan, J.G., (2010) Effect of elevated temperatures on geopolymer paste, mortar and concrete, *Cement and Concrere Research*, 40 (2), 334-339.

Kumar, A., Kumar S. (2013) "Development of Paving Blocks from Synergistic Use of Red Mud and Fly Ash Using Geopolymerization", *Construction and Building Materials*, 38, 865-871.

Lecomte I., Liegeois M., Rulmont A., Cloots R., (2003) "Synthesis and characterization of new inorganic polymeric composites based on kaolin or white clay and on ground-granulated blast furnace slag", *Journal of Materials Science*, 18(11), 2571-2579.

Lizcano M., Kim H.S., Basu S., Radovic M. (2012) Mechanical properties of sodium and potassium activated metakaolin-based geopolymers. , *Journal of Materials Science*, 47, 2607-2616.

Mustafa Al Bakri, A.M., Kamarudin H., BinHussain M., Khairul Nizar I., Zarin Y., Rafiza A.R. (2011) "The Effect of Curing Temperature on Physical and Chemical Properties of Geopolymers'', *Physics Procedia*, 22, 289-290.

Muñiz-Villarreal, M. S., Manzano-Ramírez, A., Sampieri-Bulbarela, S., Ramón Gasca-Tirado J., Reyes-Araiza, J.L., Rubio-Ávalos, J.C., Pérez-Bueno, J.J., Apatiga, L.M., Zaldivar-Cadena A., Amigó-Borrás V. (2011) "The Effect of Temperature on the Geopolymerization Process of a Metakaolin-Based Geopolymer'', *Materials Letters*,

65(6), 995-998.

Nath S. K., Kumar, S. (2013) “Influence of Iron Making Slags on Strength and Microstructure of Fly Ash Geopolymer”, *Construction and Building Materials*, 38, 924-930.

Noushini A., Aslani F., Castel A., Gilbert R.I., Uy B., Foster S. (2016) Compressive stress-strain model for low-calcium fly ash based geopolymer and heat-cured Portland cement concrete, *Cement and Concrere Composites*, 73, 136-146.

Okoye, F.N., Durgaprasad, J., Singh, N.B. (2016) Effect of silica fume on the mechanical properties of fly ash based-geopolymer concrete, *Ceramics International*, 42 (2), 3000-3006.

Pacheco-Torgal, F., Castro-Gomes J., Jalali S. (2009) ‘Tungsten mine waste geopolymeric binder: preliminary hydration products investigations’, *Construction and Building Materials*, 23, 200-209.

Palomo A., Blanco-Varela M.T., Granizo M.L., Puertas F., Vazquez T., Grutzeck M.W. (1999) “Chemical stability of cementitious materials based on metakaolin”, *Cement and Concrete Research*, 29, 997-1004.

Palomo, A., Grutzeck, M.W., Blanco, M.T. (1999) Alkali-activated fly ashes: a cement for the future, *Cement and Concrere Research*, 29 (8), 1323-1329.

Palomo, A., Krivenko, P., Garcia-Lodeiro, I., Kavalerova, E., Maltseva, O., Fernández-Jiménez, A. (2014) “A review on alkaline activation: new analytical perspectives” *Materiales de Construccion*, 64 (315), 1-24.

Panias, D., Giannopoulou, I.P., Perraki, T. (2007) “Effect of Synthesis Parameters on the Mechanical Properties of Fly Ash-Based Geopolymers”, *Colloids and Surfaces A: Physicochemical and Engineering Aspects*, 301 (1-3), 246-254.

Pavithra P., Reddy M.S., Dinakar P., Rao B.H., Satpathy B.K., Mohanty A.N. (2016) A mix design procedure for geopolymer concrete with fly ash, *Journal of Cleaner Production*, 133, 117-125.

Phoo-ngernkham T., Chindaprasirt P., Sata V., Hanjitsuwan S., Hatanaka S. (2014) The effect of adding nano-SiO_2 and nano-Al_2O_3 on properties of high calcium fly ash geopolymer cured at ambient temperature, *Materials and Design*, 55, 58-65.

Provis J.L., Lukey G.C., van Deventer J.S.J. (2005) “Do geopolymers actually contain nanocrystalline zeolites? A reexamination of existing results”, *Chemistry Materilas*, 17(12), 3075-3085.

Rees, C.A., Provis, J.L., Lukey, G.C., van Deventer, J.S.J. (2007) “In situ ATR-FTIR study of the early stages of fly ash geopolymer gel formation”, *Langmuir*, 23 (17), 9076-9082.

Rowles M.R., Hanna J.V., Pike K.J., Smith M.E., O’Connor B.H. (2007), ^{29}Si, ^{27}Al, ^{1}H and ^{23}Na MAS NMR study of the bonding character in aluminosilicate inorganic polymers. *Applied Magnetic Resonance*, 32, 663-689.

Singh, P.S., Bastow T., Trigg M. (2004) “Outstanding problems posed by nonpolymeric particulates in the synthesis of a well-structured geopolymeric material”, *Cement and Concrete Research*, 34, 1943-1947.

Sharmin A., Alengaram U.J., Jumaat M.Z., Yusuf M.O., Alamgir Kabir S.M., Bashar I.I. (2017), “Influence of source materials and the role of oxide composition on the performance of ternary blended sustainable geopolymer mortar”, *Construction and Building Materials*, 144, 608-623.

Sung, G., Bok, Y., Taek, K., and Soo, Y., (2013) “The mechanical properties of fly ash-based geopolymer concrete with alkaline activators.” *Construction and Building Materials*, 47, 409-418.

Tang, Q., Ge, Y.Y., Wang, K.T., He, Y., Cui, X.M. (2015) “Preparation and characterization of porous metakaolin-based inorganic polymer spheres as an adsorbent”, *Materials and Design*, 88, 1244-1249.

Tho-In, T., Sata, V., Boonserm, K., Chindaprasirt, P., (2018) Compressive strength and microstructure analysis of geopolymer paste using waste glass powder and fly ash. *Journal of Cleaner Production*, 172, 2892-2898.

van Jaarsveld, J. G. S., van Deventer, J. S. J., Lukey, G.C. (2002) ‘‘The Effect of Composition and Temperature on the Properties of Fly Ash- and Kaolinite-Based Geopolymers’’, *Chemical Engineering Journal*, 89(1-3), 63-73.

Villa C., Pecina E.T., Torres R., Gómez L., (2010) Geopolymer synthesis using alkaline activation of natural zeolite, *Construction and Building Materials*, 24 (11), 2084-2090.

Wang H., Li H., Yan F. (2005) “Synthesis and mechanical properties of metakaolinite-based geopolymer” *Colloids and Surfaces A: Physicochemical and Engineering Aspects*, 268 (1-3), 1-6.

Wongsa, A., Boonserm, K., Waisurasingha, C., Sata V., Chindaprasirt P. (2017) Use of municipal solid waste incinerator (MSWI) bottom ash

in high calcium fly ash geopolymer matrix, *Journal of Cleaner Production*,. 148, 49-59.

Xie, T., Ozbakkaloglu, T. (2015) Behavior of low-calcium fly and bottom ash-based geopolymer concrete cured at ambient temperature, *Ceramics International*, 41 (4), 5945-5958.

Xu, H., van Deventer, J.S.J. (2000) "The geopolymerization of alumino-silicate minerals", *International Journal of Mineral Processing*, 59 (3), 247-266.

Ye N., Yang, J., Ke, X., Zhu, J., Li, Y., Xiang, C., Wang, H., Li L., Xiao B. (2014) "Synthesis and Characterization of Geopolymer from Bayer Red Mud with Thermal Pretreatment", *Journal of American Ceramic Society*, 97(5), 1652-1660.

Ye, J., W. Zhang, W., Shi, D. (2017) Properties of an aged geopolymer synthesized from calcined ore-dressing tailing of bauxite and slag, *Cement and Concrete Research*, 100, 23-31.

Yunsheng, Z., Wei, S., Zongjin, L. (2010) "Composition design and microstructural characterization of calcined kaolin-based geopolymer cement", *Applied Clay Science*, 47 (3-4), 271-275.

Zeng, S., Wang, J. (2016) Characterization of mechanical and electric properties of geopolymers synthesized using four locally available fly ashes, *Construction and Building Materials*, 121, 386-399.

Zhang Y.S., Sun W., Li Z.J. (2005) "Hydration process of potassium polysialate (K-PSDS) geopolymer cement", *Advances in Cement Research*, 17(1), 23-28.

Zawrah, M.F., Gado, R.A., Feltin, N., Ducourtieux S., Devoille L., (2016), Recycling and utilization assessment of waste fired clay bricks (Grog) with granulated blast-furnace slag for geopolymer production, *Process Safety and Environmental Protection*, 103, 237-251.

CHAPTER IV

REASONS AND RESOLUTIONS OF TRAPPED ANNULAR PRESSURE

Gabriella FEDERER-KOVACS

(Assoc. Prof. Dr.); University of Miskolc, Miskolc, Hungary, g.federer@uni-miskolc.hu
Orcid:0000-0002-3165-8169

Hani Al KHALAF

(PhD Student); University of Miskolc, Miskolc, Hungary, hanipetro1988@gmail.com
Orcid: 0000-0002-3175-0264

Emine YALMAN

(PhD Student); University of Miskolc, Miskolc, Hungary-Iskenderun Technical University, Iskenderun-Hatay, Turkey, emine.avci@iste.edu.tr
Orcid: 0000-0002-1782-3543

Nagham Al-Haj MOHAMMED

(MSc Student); University of Miskolc, Miskolc, Hungary, naghammohamad19@gmail.com
Orcid: 0000-0001-7323-2441

Tolga DEPCI

(Prof. Dr.); Iskenderun Technical University, Iskenderun-Hatay, Turkey, tolga.depci@iste.edu.tr
Orcid: 0000-0001-9562-8068

1. Introduction

There are several well integrity issues leading to well access problems around the world. After completion most of the wells passed the Cement Bond Log (CBL) evaluation. The apparent casing collapse events have occurred usually in injectors and producers with similar rate.

Improved cement bond log response can be achieved if several changes are made to the completion program to address lost circulation and cement bond log response issues. It can also have positive effect if the amount of freshwater pre-flush is increased; the surface casing depth is increased and the amount of cement slurry (excess) is increased as well.

Casing collapse events usually occurred during the steam cycle or the

beginning of geothermal production. The apparent casing collapse events occurred over a 2 to 3 m section within the surface casing interval; however, they did not occur at the same depth interval (measured or true vertical depth (TVD)).

After the incidents investigations were started that contained a data review on casing design, construction and start-up. A comparison between the intact and failed wells has also been done. Multiple parameters have been reviewed, such as:

- Material specs;
- Surface casing depth;
- Hole geometry;
- Geology;
- Drilling issues; e.g. losses to varying degrees on all main holes;
- Casing running procedures;
- Cement procedure revised;
- Crew influence;
- CWI activities; and
- Cement bond evaluation results – expert review and reassessment.

In most cases the casing design and cementing practices are generally consistent with industry.

It can be suspected that the casing failures may have resulted from trapped liquid in the cemented surface casing-production casing annulus due to incomplete mud removal during cementing, which generated sufficient pressure during steaming to result in production casing collapse. The information that leads to the assumption of APB were:

- Wells with lower cement quality or control lines (possible forming a leak path) are apparently unaffected;
- Impacted axial length is relatively short and isolated to the area of deformation;
- The failure depth does not correlate to other parameters (e.g. geological influences);
- Damage is similar for all impacted wells; and
- Tubing deformation is due to casing failure.

These casing failures may also be influenced by combined thermal loads generated in the casing.

2. Objectives

The objective of this work is to investigate potential methods to mitigate casing damage related to trapped annular pressure (TAP) between casing strings in thermal applications. -Areas of investigation will include:

- Parameters affecting well integrity due to trapped annular pressure
- Methods or technologies to reduce the occurrence or impacts of trapped annular pressure and associated casing failures

The review focused on the specific conditions and requirements of thermal wells. Where possible, the methods or technologies were evaluated in terms of their possible application to the specific requirements of thermal operations.

3. Overview of collapse events caused by APB

The collapse shape obtained by camera run in thermal operations is similar to collapse shapes that have been seen in geothermal wells that are also subjected to thermal load. Limited numbers of literatures exist in relation with collapse events occurred by expansion of channeled or pocketed fluid in the cement and even those are related to geothermal applications.

Thermal production wells as well as geothermal wells are built of concentric casings with cement in between the walls. The mechanical integrity of casings is required for well operations whether it is a geothermal or a steam injection well. Casing failures cause decreased cross-sectional area and can lead to a reduced production from the well, leave the well inoperative and in worst cases increase the risk of a well blowout.

3.1 Trapped annular pressure (TAP)

Annular Pressure Build-up (APB) is a phenomenon caused by the heating and expanding of trapped fluid in the closed annulus.

Many studies on the topic is related to a fluid filled annulus, where the cement top is not at surface and may or may not be inside the next casing shoe. The trapped fluid is heated by the injection and production operations, either by the injection of hot fluids (e.g. steam) or the production of fluids at the reservoir temperature. Fluid flow during drilling may also cause the same, as reported by Pattillo et al. (2004). -The TAP issues with trapped fluid pockets or channels in the cement sheath are somewhat different; however, the phenomenon is similar. Because of this similarity and the lack of literature related on the fluid pocket caused

collapse the methods for fluid filled annuli pressure build-up mitigation techniques were also reviewed.

When a closed system is filled with fluids that are heated, fluid expansion will occur that result induced pressure. Field results have shown the production casing can deform or collapse after production or injection starts due to heating effects.

When an unconfined fluid is heated, it will expand in volume, in case it is free to expand it is described by:

$$V = V_0(1 + \alpha\Delta T) \tag{1}$$

Where:

V - expanded volume, m^3
V_0 - initial volume, m^3
A - fluid thermal expansivity, K^{-1}
ΔT - average fluid temperature change, °C

According to Adams (1991) annulus heat-up pressures are due to two diverse effects: a volumetric expansion of the annulus fluids, and a radial expansion of the well casing.

According to Adams and based on O'Brien's work (1996), the change in volume because of a change in temperature and as a reason of the change in pressure due to volume limitation equals with the change in volume of the casing results a pressure change described by the following equation:

$$\Delta p = \frac{\alpha\Delta T}{\frac{1}{c_f}+\frac{D}{Et}} \tag{2}$$

Where:

Δp - fluid pressure change, Pa
c_f - fluid compressibility, Pa^{-1}
D - ID of outer casing or OD of inner caasing
E - Young's modulus
t - casing wall thickness (outer or inner)

Casing and tubing strings are not perfectly rigid container therefore when pressure builds up the diameter of the inner and outer pipe changes. Thermal expansivity and compressibility properties are functions of both pressure and temperature.

In land wells where the annulus can be accessed, APB is usually handled by bleeding off annular pressure as needed. In case of offshore operations this feature is usually not available; therefore, these operations are more likely prone to failures caused by APB. Collapse type failures in the up-hole section are rare because differential pressure (external – internal casing pressures) typically increases with depth.

Annular pressure build-up occurs on every annulus is full of fluid and the casing is cemented into the outer casing shoe and in cases where the annulus is cemented to the top but free water gets trapped in the cement sheath.

The consequences of a pressure build-up without the benefit of bleed-off or formation fracture can be catastrophic and usually happen in two different ways:

- Pressure can build up in the tubing-production casing annulus enough to collapse the tubing or burst the production casing, or
- The annulus between the inner and the outer casing can be heated to the point where the production casing collapses or the outer casing bursts

As presented in many studies, it can be deduced that APB cannot be ceased but with appropriate technique it can be prevented (Moe and Erpelding, 2000). Well designers can anticipate APB and take appropriate steps to avoid the expensive and dangerous results of pressure overload.

3.2 Failure mechanisms

Uniform external to internal differential pressure must exist if the casings collapse is a buckling shape. Most of the standards use combined mathematical methods in the empirical equations to determine collapse resistance of casings. These equations usually do not consider external supporting cement and non-uniform stresses and are also considered to be rather conservative. The ratio of outer diameter to thickness (D/t) determines what range of compressive stresses cause the collapse (elastic-, plastic- or intermediate range). For high values elastic collapse is the governing factor, for low values it occurs in the plastic range. The critical collapse pressure for long pipes is (Kaldal 2013):

$$p_{cr} = \frac{E}{4(1-\nu^2)}\left(\frac{t}{R}\right)^3 \tag{3}$$

Where:

E-Young's modulus (MPa)
ν-Poisson's ratio
t-wall thickness (cm)
R-pipe radius (cm)

High temperature has the effect of lowering the modulus of elasticity and thus the yield strength of the body (Rabia, 1985). The higher the casing quality is, the greater the reduction in yield strength due to high temperature. This results that the casing can withstand smaller collapse pressures than on lower temperature. The equation also helps to understand that increasing wall thickness makes the casing resistant to higher pressures. According to Kaldal et al. (2013) geometric imperfections and defects can also cause reduction in collapse resistance of casing.

When for any reason the external pressure is higher than the actual strength of the pipe failures happen. However, there are company policies in casing design it may be worth to compare casing data with American Petroleum Institute (API) standards. After the well is completed, a structural support is provided by the cement sheath. When the well is heated, the cement retains the thermally expanding casing and limits movements in various axes to some extent. If the cement is damaged, the impurities can lead to non-uniform conditions. Instability can be caused by off-centered string or water/mud accumulation. This can lead to fluid entrapment in one side of the casing. In case if there is trapped fluid in pockets or channels in the cement sheath that expands when effected by heat pressure can build-up high enough to cause casing collapse. In these cases, collapse shape differs from a collapse shape that is created in an entirely fluid filled annulus. A difference in the collapse shapes can be seen in cases where the casing is cemented or without any external support (Kaldal, Jónsson, Pálsson and Karlsdóttir 2013). (Fig.1).

The "bulging collapse shape" is related to the existing and mostly effective external support of the cement. According to Kaldal et al. (2013), the expression 'bulging collapse' refers to the type of shape of the casing failure amongst many shapes.

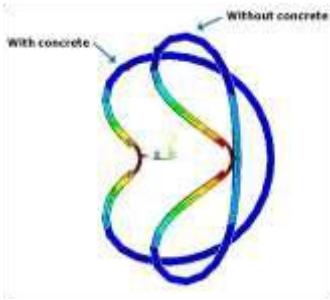

Fig.1 After collapse shapes with and without concrete support (Kaldal et al. 2013).

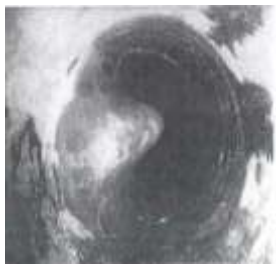

Fig.2 The buckling shape of a collapsed casing (Tahmourpour et al., 2017).

Many of the TAP collapsed casings is the same as shown in Figure 2. This type of failure suggests that the conditions on the outer side of the casing are not uniform. Instability in the cement supported casing can happen due to lack of centralization or trapped fluid.

It is also known that cold wells are more prone to APB because at installation the ambient temperature is cold in contrast to elevated production or injection temperatures that create a higher thermal shock in the system. According to Kaldal et al. (2013) pipe collapse due to temperature loading is not as well documented as APB collapses. Cyclic temperature loading could decrease the pipe's collapse resistance and under such tension that would result failure. It is also important information that large diameter surface and intermediate casings with relatively small wall thickness are particularly susceptible to this mode of failure (Hole, 2008).

3.3 Importance of design

The related literature mentions casing design as a key element in well integrity issues and therefore this section gives an overview of the main parameters of an accurate casing design.

The long-term integrity of a well is a function of many properties. In advance of planning an operation a profound and accurate design has to be performed taking all the possible events into consideration. Despite of the most accurate design, failures can happen but the rate of failure may be reduced.

- The first and most important factor is casing design:

In case of thermal applications burst and collapse are not enough to design for since pipes can lengthen and trapped annular fluids can expand,

causing severe loads that also must be considered.

Up-hole collapse events are rare and despite of applying best industrial practices and design, collapse caused by trapped fluid is difficult to avoid.

- The second factor is the presence of H_2S:

It needs to be considered that the presence and concentration of this acid is important since it is highly corrosive. Although corrosion typically has not proven to be a serious problem with respect to casing integrity in thermal well applications, various sulphide stress corrosion cracking mechanisms have been identified as the main reason to many thermal well operations. Under severe conditions damage can occur in a very short time (even within hours), while in less critical situations, small crack may develop in the metal which grows into larger under cyclic loads eventually causing failure (Matthews and Tao, 2011).

- The third and one of the most important well integrity issues is cementing:

Good cement jobs not only contain good quality cement slurry mixing but also accurately choose pump rates, displacement procedure and calculating the correct amount and time. This process needs to be precise in order to provide a good cement sheath that provides additional strength for the casings and protects the formations. A good cement placement practice has to include pipe reciprocation and centralization.

Despite doing all the necessary precautions there is still a potential for trapped free water (in cases in surface casing interval) due to cement hydration, casing eccentricity and cement fall back. In the event of cement fall back, attributable to loss circulation zone, the risk of TAP is higher.

- Steam injection procedure is also an important factor:

In case of drastically increased temperature the heat change can be too rapid which means a high risk on casing collapse in case of trapped fluid in the annulus.

Similarly, to steam injection, geothermal hot water production will have the same effect on trapped water.

4. Overview of mitigation methods

Even with the best design and available technology it is not possible to eliminate APB conclusively but it is possible to reduce the probability of a thermally induced failure. APB can be predicted and by appropriate mitigation methods its threat intensely reduced.

The literature reviewed in this study falls under the following categories:

- Different methods to mitigate annular pressure build-up;
- Cement applications in case of high temperature well conditions; and
- Well design considerations for geothermal applications.

In the following sections the different methods to mitigate trapped annular pressure will be discussed in detail.

4.1 Sophisticated casing design

In the literature one of the methods to moderate the effects of APB is improved well design. In thermal applications probably the most critical part of the design is the selection of casings (sizes, material, casing shoe depth and completion).

In normal applications casings are designed not to be prone to tensile yielding. Models indicated the use of N-80, C-95 and P-110 but these casing designs failed at higher temperature. In normal casing designs pipe tensile yield stress is the failure point. In case of thermal operation when the casing is cemented the tensile stress is the result of compression when heated and tensile stress when cooled. If the connection can handle the loading the tensile yield will not cause a failure even if it is exceeded. The tensile stresses and connection strength are similar for both, K-55 and L-80, grades therefore the pipe yielding at the lower stress would have a higher design factor. For operating at high temperatures (thermal operations or geothermal wells), design model shows the K-55 casing provides a greater safety design factor than L-80 buttress. For these reasons K-55 grade casing with premium connections gives a better design for thermal operations than L-80 or higher grade material (Lepper 1994).

Collapse resistance is also an important factor in the design of a thermal well. Tests have shown that K-55 casing retains significant collapse resistance when at axial yield (Lepper 1994). The design factors for thermal wells need to be higher than for conventional wells and shall be not less than the mentioned values (Eq.4) (Bradley, 1987). According to Hole (2008) for a geothermal well SF has to be no less than 1.2.

$$DF = SF_{min} \leq SF = \frac{pipe\ collapse\ rating}{\rho * g * h} \tag{4}$$

4.1.1 Design for thermal expansion of trapped fluid

A detailed casing design for a thermal application should include a design factor for possible trapped fluid. At temperatures above 100°C the

pressure increases and the change is about 1.6 MPa/°C (Hole, 2008). The highest pressure feasible from the thermal expansion of trapped liquid in the annulus quickly overcomes the strengths of normal casings in either burst or collapse. Since it is advantageous to keep the integrity of the production casing therefore any failure should be designed to happen in the outer string. For this reason, the collapse resistance of the inner casing should be higher than the burst resistance of the outer casing for the final two casing and can be calculated from Eq.5.

$$SF_{tf} = \frac{\text{production casing collapse strength}}{\text{outer casing burst strength}} \tag{5}$$

Where: SF_{tf}-Safety design factor for trapped fluid

This design factor shall not be below 1.2 (Southon 2005; Hole 2008).

4.2 Full Height Cementing

In all the reviewed literature, full height cement column is suggested as the best way to prevent APB problems. However, if the cement column is not consistent and channels are left or cracks are created, trapped fluid can cause an almost similar problem as APB in case of a fluid filled annulus.

The effectiveness of full height cement is based on the hypothesis that the cement sheaths will be error free. A non-continuous, poor cement bond can lead to more problems than leaving the annulus uncemented, as it is discussed later in Section 4.3. It is agreed though that cement completely encircling casing, even is the strength is low, will prevent effects of buckling and that the accuracy of cement placement is more important than even cement strength (O`Brien, 1996).

The effectiveness of cementing to surface depends on the mud removal. This cannot be certain and if even a little fluid stays (flow channel, fallback gap) then the liquid in the void will act just like a not cemented annulus. This method is therefore not entirely reliable (Leach and Adams, 1993).

Significant losses can cause two types of problems in cement job:

- Preflush can be lost and in that case that it mixes with the following cement slurry the quality of the cement will degrade or a free water inclusion may form; or
- Cement can be lost/fallback leaving a fluid filled gap in the closed annuli space

These problems can lead to trapped fluid in the annulus and can cause an annular pressure build-up.

4.2.1 Foam or elastic cement applications

Cementing material also contributes to the success of full height cement. The long-term integrity of a cement sheath shows how it can endure temperature and pressure changes, mechanical shocks and repeated loading. Integrity of the cement bond depends on the material and mechanical properties (Young's modulus, tensile strength and resistance to chemical attack) and influenced by the effectiveness of slurry and its placement (Griffith et al., 2004; Tahmourpour et al. 2010).

4.2.1.1 Foam cement

Foamed cement systems have optimized mechanical properties and by varying the amount of N_2 the volume reduction can also be compensated. Foam cement is useful where reduced density cement is needed to prevent cement losses. It also been found as a good zone isolating material compared to the hollow-spheres and conventional cement systems (Kopp et al. 2000). Foam cement has high extensional viscosity that gives them the ability of filling the gaps more than conventional slurries.

Given a low overall fluid loss this material is also a good preventer against influxes. As foam cement`s column pressure stays constant during the hydration period cement loss can also be decreased or avoided. Typically oil well cement shrink 4% under hydration while gas bubbles, as seen in Fig.3, in foam cement can balance this shrinkage.

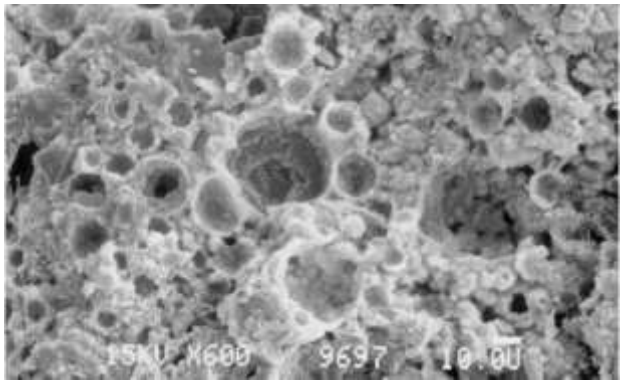

Figure 3. Quality foamed cement, 600 x magnification (Kopp et al. 2000).

Challenges and disadvantages of this method is that nitrogen solubility is an important factor in foamed cement characteristic and it is difficult to evaluate since foam cement has poor acoustic properties therefore conventional CBL will not be accurate. However earlier experiments

showed that with a 75% of cement sheath fraction standard CBL can work (Griffith et al. 2004).

4.2.1.2 Elastic/resilient cement

It is not always possible to release the annulus pressure into the formation or through a bleed-off valve since in some cases operational restrictions do not allow this type of relief. In these cases a well-designed cement slurry system placed with a proper cement job can provide a lifetime zonal isolation. It is also an option for those cases when foam cement is not feasible. The useful life of the foamed cement sheath is hundreds of load cycles more compared to the conventional, resilient cement provides an ultimate resistance as it can be seen in Fig.4. Operations in which elastic cement can provide benefit are high-rate producers, injection wells and HPHT wells.

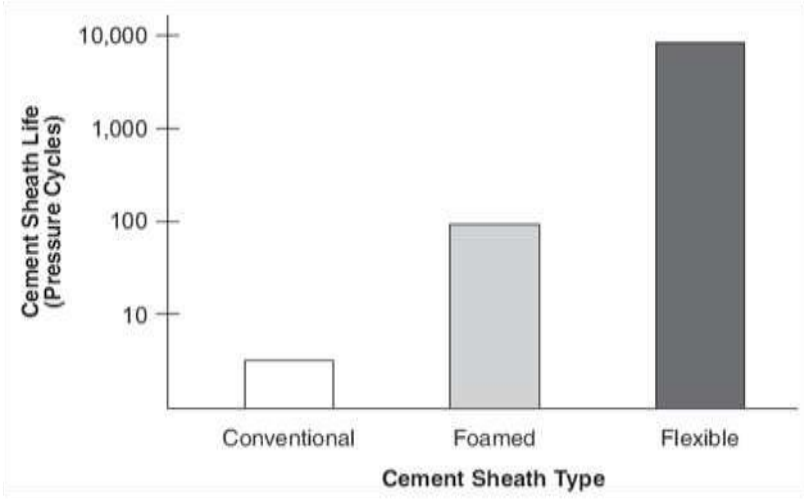

Figure 4. Comparison of cement sheath lives (Kopp et al. 2000).

"Flexible" cement designs focal point is dynamic slurry properties, compressibility, yield strength and other properties such as permeability, porosity since it needs to have elastic features to maintain its integrity. The density of these elastic cement slurries can be modified depending on the special needs in a range from ultra-light to super-heavyweight (Tahmourpour et al., 2010). The rheology of the slurries can be customized and optimized according to the needs of the operation.

4.3 Cement shortfall

Many failures such as these ones have been in casings cemented inside other casing. Cementing the annulus between two strings is not always as efficient as is thought and can create a variety of failures. In many situations it is better to leave the casing-casing annulus uncemented or filled with completion or drilling fluid compared to full height but not good quality cement (O'Brien, 1996).

In case of a cement shortfall, the top of the cement is left below the previous casing shoe. This way the heat-up pressure creates a natural 'path' by fracturing the formation. By applying this method, a closed annulus can be avoided. This option provides an easy solution but not always possible to accomplish.

In case if a closed annulus is created, so closing the vulnerable formations out in the open hole section, but the casing-casing annulus is not cemented to the surface, pressure can be relieved at the surface. These methods are detailed in the next sections.

4.4 Leak path or bleed port installation

Another means of preventing APB is a leak path or a bleed port. The rapture disc technology was patented by Staudt (2004). As a preliminary point worth to note that this device was developed for offshore wells where pressure can be relieved between two fluid filled annulus or if the disc is in the outer string, it is as deep that flow to the formation is not ruinous. Casing leak path or "burst-disk" technology set in the outer casing allows casing to fail in a predictable way and vent outward rather than collapse inward (Vargo et al., 2003). By rupturing the disk, the increasing pressure creates a leak path towards the formation. The rapture disk technology (see in Fig.5) has been tested and optimized and is preferred since it does not compromise internal well integrity (Williamson et al. 2003). No field test related to the burst disk has been reported in details in any of the reviewed literature. However, some operators consider this kind of controlled failure as an unacceptable risk.

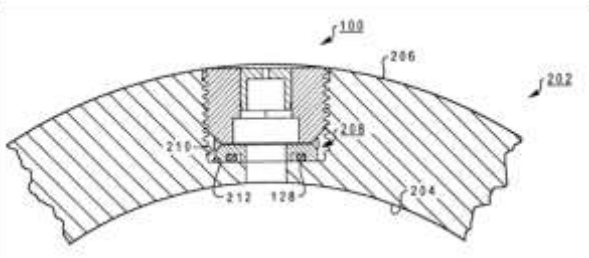

Figure 5. Rapture disk technology in casing (Staudt, 2004).

For land wells (mainly geothermal) it is a routine to install surface-accessible wellhead relief valves. If the pressure overcomes certain pre-set value the trapped pressure can be relieved through manual or automatic valves. A pressure build-up in a fluid filled but closed annulus can also be bled off through a casing head valve.

4.5 Syntactic, crushable foam wrap

Several authors have suggested crushable foam material in the annulus as a method to reduce APB by accommodating the expansion of trapped fluids. This means syntactic foam that contains small hollow glass spheres filled with air at atmospheric pressure (Leach and Adams 1993). (See in Fig.6) Other authors have suggested compressive urethane foams. According to the patent the spheres can be used in conjunction with different fluids as well depending on the purpose of use such as production fluids, drilling mud, spacer fluids, chemical pills, completion fluid or their combination.

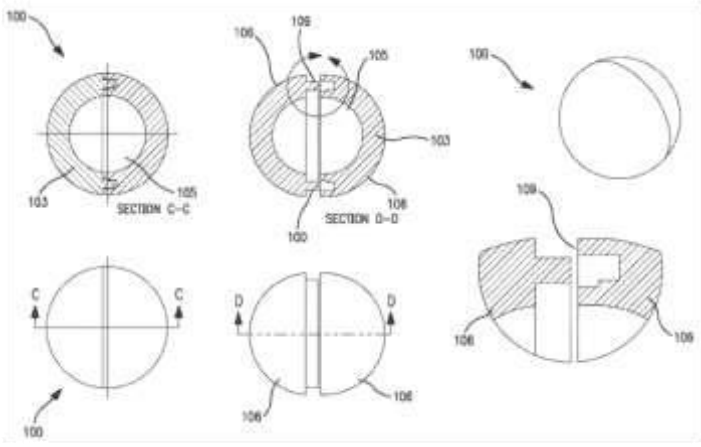

Figure 6. Sphere hollow particles (Shepherd, 2010).

This foam wrap is attached to the outside surface of the inner string of the annulus as shown in Fig.7. The spheres can also be placed directly from the surface or be circulated down the wellbore as part of the composition of completion and pumped into place in the annulus. The wrap length and volume have to be relatively small only 2-8% of the total annulus length. This amount is defined by the anticipated volume change in response to the temperature increase.

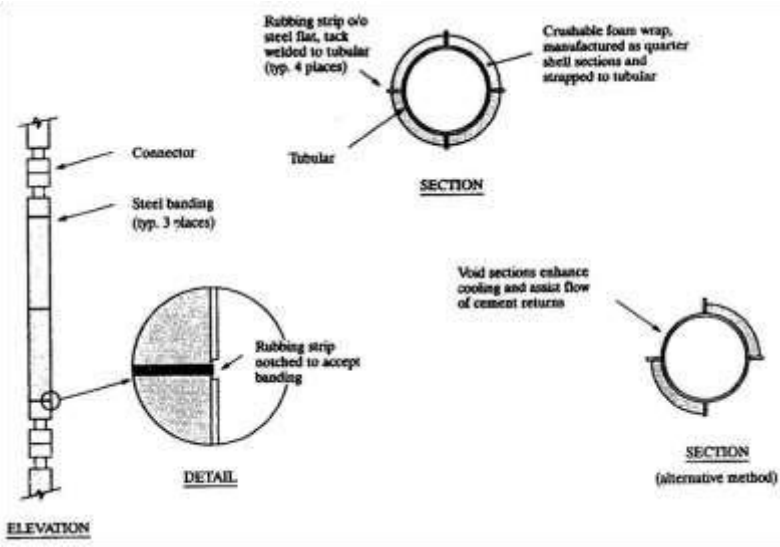

Fig.7. Placement of sphere hollow particles around the string (Leach and Adams, 1993).

The spheres are surrounded by placement fluid which is usually followed by additional fluids (e.g. cement slurry) that usually do not mix with the fluid around the particles. When annular pressure builds up the spheres crush providing more space for the fluid to expand.

4.6 Compressible or shrinking fluid in the annulus

Two other methods can be found in the literature to mitigate APB. In case of these two methods also fluid fills up the upper section of the annular space above TOC.

4.6.1 Compressible fluid in the annulus

A method where compressible fluids are placed in the annulus to balance the volume increase caused by thermal load is introduced in this section. This method has already been successfully used for APB mitigation in deepwater operations which are more inclined to this type of failure (Vargo et al., 2003). This method has been tested and proved to be effective in wells prone to annular pressure increase due to heat up.

Compressible fluid in the annulus means a nitrified foam spacer that is placed above the top-of-cement in the annulus between two casing strings. A reasonably small percentage of nitrogen, less than 5% of the trapped volume, is adequate to form a compressible pad that can facilitate the pressure increase. Pressure increase vs. increase in temperature with non-

foamed fluids and foamed fluids can be seen in Fig. 8 and Fig. 9, respectively.

The theory of this method is shown in the Ideal Gas Law (Loder et al., 2003). A decrease in the gas volume causes a small increase of pressure. This relation is well described by Boyle's Law that shows the pressure change in a system is directly proportional to the change in volume (Eq.6).

$$p_1 V_1 = p_2 V_2 \tag{6}$$

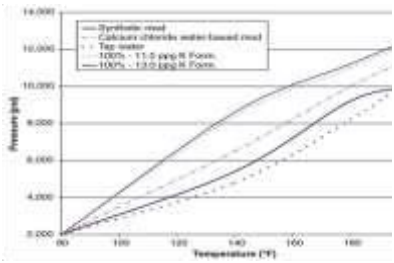

Fig.8. Pressure increase vs. increase in temperature with non-foamed fluids (Vargo et al. 2003).

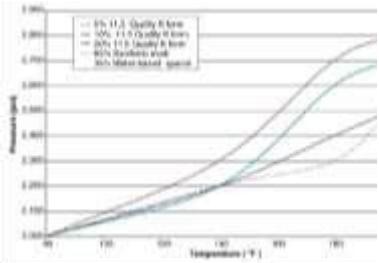

Fig.9. Pressure increase vs. increase in temperature with foamed fluids (Vargo et al. 2003)

Therefore, with this method the size of the pressure build-up can be moderated from thousands to hundreds of kPa or psi above the placement pressure. This magnitude is significant when the pressures become close to the collapse pressure of a casing string.

4.6.2 Spacer fluid that shrinks

Annular fluids that shrink upon heating have been suggested as a means to prevent APB. These may be pumped as a spacer before the cement slurry which contains about 20-40% of emulsified methyl methacrylate monomer (MMA). According to Bloys et al. (2008) MMA phase shrinks by about 20% upon polymerization creating space for the other fluid's volume increase. Polymerization is initiated by heat, as seen in Fig.10 and even the target temperature can be controlled and the earlier polymerization can be blocked by appropriate type of initiator. The MMA (10%-50% very sable emulsion) is emulsified into a simple water-based fluid with densities from 0.96-1.8 g/cm^3 that is planned to be the last spacer before the cement.

This method has already been successfully tested in a 500 ft deep test well in Bossier City, LA. In this test well a 7" casing was hanged inside of

9-5/8” casing. The bottom of the 7” casing was sealed with flapper valves what allows the test fluids to be circulated through. The MMA (concentration 28% of liquid phase) spacer was displaced into the annulus. The annulus was sealed and heating started. Pressure increased but once the target temperature was achieved polymerization and the quick pressure drop begun.

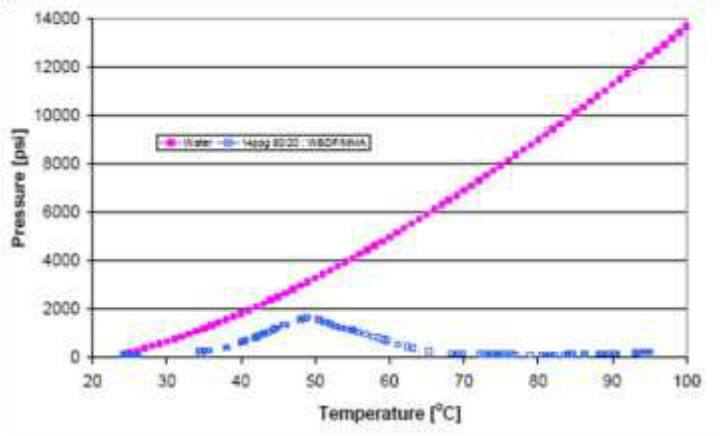

Figure 10. Behaviour of water vs. a 14 ppg MMA emulsion (Bloys et al., 2008).

4.7 VIT or VIC applications

Vacuum insulated tubing (VIT) has been successfully applied to mitigate annular pressure build-up. VIT with thermal packer is an applied insulation technique in case of steam injection procedures. However due to difficulties vacuum insulated casing (VIC) as a completion technique has been researched and used in some oilfield operation (Yue et al. 2013).

4.7.1 Vacuum insulated tubing (VIT) application

The vacuum insulated tubing is a piping system consists of an inner and outer tubing welded together at both ends, as seen in Fig.11. The first oilfield application happened in the Alaskan tundra to prevent flowline subsidence. Since then, in many APB related cases VIT has been recognized as a potential mitigation technique.

There are special areas where VIT has been applied successfully (Azzola et al., 2004):

- Enhanced oil recovery

- SAGD
- Prevention of paraffin build-up
- Lessen the severity of cold start-up and hydrate formation
- Temperature preservation for heavy oil flow through

Vacuum insulated tubing given its effective insulating capabilities can prevent the annulus to be heated to the point when the fluid expansion creates high enough pressure for casing or tubing damage. The piping sizes ranges from 2" to 7" and usually the grade is L-80 or 13Cr. The circular space between the two welded tubes is typically 0.15-0.5" wide. The space contains aluminium wraps for reducing radiation, and a substance that removes gas by sorption, also known as getter, in order to make the design to be able to preserve the vacuum for about 10 years (Azzola et al., 2004).

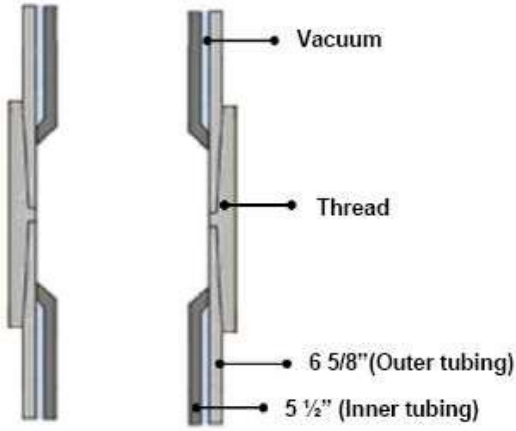

Figure 11. Representation of a vacuum insulated tubing (Ferreira et al., 2012).

An issue with VIT is that it is not able to provide a similar collapse and burst resistance as a conventional tubing of the same size and grade. According to (Yue et al. 2013), when a thermally loaded well is deeper than 600 m VIT with thermal packer technique is recommended. Further limitations of this technique is related to thermal packer`s mechanical failure which sometimes so serious that it is not possible to continue steam cycles. It also has workover problems if VIT is moved after steam injection or economic problems if VIT is left in the well.

4.7.2 Vacuum insulated casing (VIC) application

In order to prevent problems and fulfill insulation, injection and production expectations collectively vacuum insulated casing (VIC) can be a viable technique.

It can be stated that VIC equals to VIT in manufacturing such as the design theory, vacuum as insulation, materials, welding but VIC is also different from VIT in function and its role in the well`s life (Yue et al., 2013). VIC is an integral part of well completion, as seen in Fig.12.

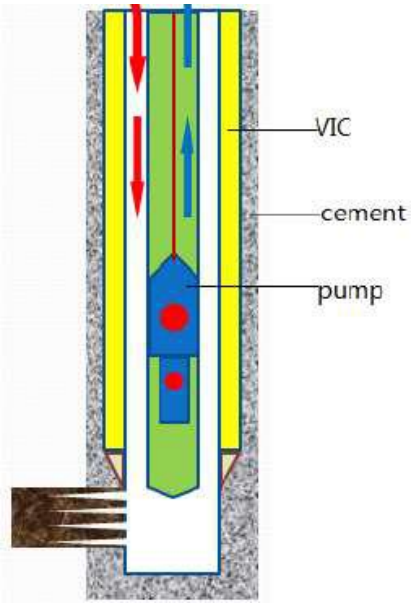

Fig.12. VIC as part of the well completion (Yue et al., 2013).

Advantages of VIC compared to VIT:

- There is no packer
- It avoids workover
- It increases steam flow area

While having their advantages they inevitably have some mechanical problems since the welding technique is the same as in case of VIT. This application is a new technique and has only been tested recently (Yue et al. 2013) however VIC has great potential in different thermal applications. As reported by Yue et al. (2013) a field trial was performed in several oilfileds in China in more than 10 wells.

5. Summary APB resolutions

It can be concluded that there are numerous methods exist in the literature for mitigating annular pressure build-up however only a small percentage pay attention to the problem of trapped fluid in pockets or channels. This special pressure buildup problem despite of all the applied best practices cannot be eliminated; therefore prevention of fluid trapped in pockets or channels behind the casing is the most important task.

Table 1. Summary of the mitigation methods.

Mitigation methods	Key parameters	Maturity	Use in thermal application	Environmental effect	Technology	Logistics	Relative cost	Regulatory recommended practice
Sophisticated well design		C						comply
Full Height Cement		C						comply
Foamed Cement		C						comply
Resilient Cement		D						permit
Cement Shortfall		C						unallowed
Rapture Disk		P	N/A				N/A	unallowed
Relief Valve		D						permit
Crushable foam wrap		P						permit
Compressible fluid (N_2)		C						permit
Shrinking fluid (MMA)		P						permit
VIT		D						comply
VIC		P	N/A					N/A

C-	commercial/often used
D-	well developed/seldom used
P-	prototype/not used or only tested

A table (Table 1) was prepared about a summary of the mitigation methods that help in comparison and choose the best method for thermal application.

6. Conclusions and recommendations

From the work conducted in this literature review, the following conclusions are made:

- Cement integrity have a key role in well integrity and if that have been compromised casing collapse occurs caused by trapped annular liquid behind the casing.

- Steam injection means a great thermal load in a well. In case of trapped fluid behind the casing pressure can access the collapse pressure when

fluid expands induced by 300°C injected steam. Trapped pressure problem cannot be 100% eliminated therefore prevention its forming is important.

- There are numerous mitigation methods in the literature but not every method can be applied for each drilled well. The final method depends on regulatory board approval, logistics, reliability and cost.

- A basic method in the industry is casing upgrading. In a thermal application it is major to apply higher safety factors than in case of a conventional application.

- Applying full height good cement job is the best practice for wells however the evaluation of the cement material can highly improve the cement job in thermal wells. Testing foam cement, resilient cement or cement with hollow microspheres may be conducted. Getting more information on the behaviour of these materials is important as this way reliable data can be served for further finite element analysis. Also, a rarely examined parameter is cement permeability however it is a main factor that reflects on the sealing capability of each cement type. Important to note that the especially high temperature can also create more changes in the cement material that expected therefore a full testing can be necessary and useful. Testing of special material, like hollow sphere cement at 300° can provide results that are novelty for the industry since this type of testing has not been done before.

- There are many potential methods for preventing trapped annular fluid therefore testing of methods would be beneficial since this helps in better understanding and more accurate planning for future applications.

7. References

Azzola, J.H., Tselepidakis, D.P., Pattillo, P.D., Richey, J.F., Tinker, S.J., Miller, R.A., Segreto, S.J. 2004. Application of Vacuum Insulated Tubing to Mitigate Annular Pressure Buildup. SPE 90232, SPE Annual Technical Conference and Exhibition, Houston, Texas, USA. 26-29 September 2004.

Bloys, B., Foley, R; Harvey, F; Davis, J; Cassel, T; Bloys, B; Gonzales, M; Hermes, R; Daniel, J M. 2008. Trapped Annular Pressure Mitigation: A Spacer Fluid That Shrinks: Update. IADC/SPE 112872, IADC/SPE Drilling Conference, Orlando, Florida, USA. 4-6 March 2008

Bradley, H B. Petroleum engineering handbook. United States: N. p., 1987. Web.

Ferreira, M.V.D., Santos, A.R., Vanzan, V. 2012. Thermally Insulated Tubing Application to Prevent Annular Pressure Buildup in Brazil Offshore Fields.

SPE 151044, SPE Deepwater Drilling and Completions Conference, Galveston, Texas, USA. 20-21 June 2012.

Griffith, J.E., Lende, G., Ravi, K., Saasen, A., Nodland, N.E., Jordal, O.H. 2004. Foam Cement Engineering and Implementation for Cement Sheath Integrity at High Temperature and High Pressure. IADC/SPE 87194, IADC/SPE Drilling Conference, Dallas, Texas, USA., 2-4 March 2004.

Hasan,A.R., Izgec, B., Kabir,C.S. 2009. Sustaining Production by Managing Annular-Pressure Buildup. May 2010 SPE Production & Operations: 195-203, SPE 120778,

Hole, H. 2008. Geothermal Well Design-Casing and Wellhead. Petroleum Engineering Summer School, Dubrovnik, Croatia, Workshop #26 June 9-13,08

Kaldal, G.S., Jonssonm.P., Palsson, H., Karlsdottir, S.N. 2013. Collapse Analysis of the Casing in High Temperature Geothermal Wells. Thirty-eight Workshop on Geothermal Reservoir Engineering, Stanford, California, February 11-13, 2013

Kopp, K., Reed, S., Foreman,J., Carty, B., Griffith, J. 2000. Foamed Cement vs. Conventional Cement for Zonal Isolation-Case Histories. SPE 62895, SPE Annual Technical Conference and Exhibition, Dallas, Texas, October 1-4.

Leach, C.P., Adams, A.J. 1993. A New Method for the Relief of Annular Heat-Up Pressures. SPE 25497, Production Operations Symposium, Oklahoma City, Oklahoma, USA, March 21-23, 1993

Lepper, B.; Production Casing Performance In a Thermal Field; PETSOC-94-07.; DOI: 10.2118/94-07

Loder, T., Evans, J.H., Griffith, J.E. 2003. Prediction of and Effective Preventative Solution for Annular Fluid Pressure Buildup on Subsea Completed Wells-Case Study. SPE 84270, SPE Annual Technical Conference and Exhibition, Denver, Colorado, USA, 5-8 October 2003.

Matthews, C.; Tao, G.; Adams, A.; Special Considerations for Well Tubular Design at Elevated Temperatures; SPE Drilling & Completion (2020); DOI: 10.2118/199570-PA

Moe, B., Erpelding, P. 2000. Annular Pressure Buildup: What it is and what to do about it. Deepwater Technology, August 2000

O`Brien,T.B., Simpson,O.G. 1996. A Case Against Cementing Casing-Casing Annuli. IADC/SPE 35106, IADC/SPE Drilling Conference, New Orleans, Luisiana, USA, 12-15 March 1996.

Pattillo,P.D.,Cocales,B.W., Morey,S.C. 2004. Analysis of an Annular Pressure Buildup Failure During Drill Ahead. SPE 89775, SPE Annual Technical Conference and Exhibition, Houston, Texas

Rabia, H. Oilwell Drilling Engineering. Principles and Practice. Graham&Trotman Ltd. London 1995. 322 p.1.

Southon, J.N.A. 2005. Geothermal Well Design, Construction and Failures. Proceedings World Geothermal Congress 2005, Antalya, Turkey

Tahmourpour,F.,Hashki, K., Hassan, H. 2007. Different Methods to Avoid Annular Pressure Buildup by Appropriate Engineered Sealant and Applying Best Practices (Cementing and Drilling). SPE 110040, SPE Annual Technical Conference and Exhibition, Anaheim, California

Tahmourpour,F.,Hashki, K., Hassan, H. 2007. Different Methods to Avoid Annular Pressure Buildup by Appropriate Engineered Sealant and Applying Best Practices (Cementing and Drilling). June 2010 SPE Drilling & Completion: 248-254,

Thorhallsson, S. Geothermal well operation and maintenance. 2003 11.10.2017; Available from: http://www.os.is/gogn/flytja/JHS-Skjol/IGC2003ShortCourse/13Sverrir.pdf.

Barrier definitions and risk assessment tools for geothermal wells. Available from: https://www.researchgate.net/publication/324573751_Barrier_definitions_and_risk_assessment_tools_for_geothermal_wells [accessed Apr 19 2021].

Yue, H., Pang, W., Zhang,T., He, Z., Hou, Q., Deng, D., Du, J., Mao, J., Zhao, X., Duan, Y. 2013. Integral Completion Technique for Heavy Oil Thermal Recovery. SPE 165518, SPE Heavy Oil Conference Canada, Calgary, Alberta, Canada

Vargo Jr., R.F., Payne, M., Faul, R., Leblanc, J., Griffith, J.E. 2003. Practical and Successful Prevention of Annular Pressure Buildup on the Marlin Project. SPE 77473, SPE Annual Technical Conference and Exhibition, San Antonio, Texas, USA, 29 September-2 October, 2002

Williamson, R., Sanders, W., Jakabosky, T., Serio, M., Griffith, J.E. 2003. Control of Contained-Annulus Fluid Pressure Buildup. SPE/IADC 79875, SPE/IADC Drilling Conference, Amsterdam, The Netherlands

Staudt, J. J. (2004). U.S. Patent No. 6,675,898. Washington, DC: U.S. Patent and Trademark Office.

Shepherd, J.E,; Rakow, J.F.; Pattillo, Ii, P.D.; US Patent No. US2010/0113310 A1; 2010; Washington, DC: U.S. Patent and Trademark Office.

CHAPTER V

THE EVALUATION ON WATER STRUCTURE IN MARDIN HISTORICAL MADRASAHS

F. Demet AYKAL

(Prof. Dr.); Dicle University, Diyarbakır, Turkey,
e-mail: demetaykal@gmail.com,
Orcid No: 0000-0003-2424-0407

Meltem ERBAŞ ÖZİL

(Asst. Prof.) Dicle University, Diyarbakır, Turkey,
e-mail:meltemerbas@gmail.com,
Orcid No: 0000-0003-2077-8728

1. Introduction

Water has always been a basic and indispensable element for people. The water, which has affected settlement and lifestyles of people throughout history, is necessary for a healthy life. Water has the features of rehabilitating, tranquillizing, relaxing and keeping people away from stress in psychological respects. In addition to its vital importance, water is an indispensable factor for landscape architecture. This factor welcomes us as landscape elements, such as ornamental pool, water running on wall, fountain in architectural respects.

The city of Mardin, located in the north of Mesopotamia, hosted people from different religions and nationalities throughout history. These people from different cultures lived together based on mutual respect. They have built a cultural harmony in Mardin by still maintaining this way of life. Respect has become a factor which is not only supporting people but also buildings. The historical buildings in Mardin have survived until today by challenging the destructive effects of time. Accordingly, it has made his name known throughout the world as a cultural and historical city.

One of the group of buildings enabling the city to have a cultural and historical characteristics is madrasahs. The abundance of historical madrasahs in Mardin shows the importance given to education in the past in the region. When examining madrasahs, which have generally similar structural typologies, in detail, water features, bringing in sound and life to these buildings, are seen. These water architecture features in madrasahs

were not only used for ornamental purposes but also used for its positive effects on the psychology of user and representing cleaning and purity.

The aim of the paper was to analyze how art and techniques affected water structure at the histo-rical madrasahs in the city Mardin and to research about what functional contributions water made to madrasah architecture except for using water as a landscape element.

2. Water Structure and Religional Relation

The structures, which must use water in order to function or built for using water, are called water architecture structures (Tayla, 2007).

The water architecture has been used in order to build following constructions from ancient periods: to collect snow and rainwater at cisterns and reservoirs, and existing running water at weirs, especially in Anatolia and to transfer this collected water to somewhere through channels or tunnels with appropriate slopes, and to distribute water brought to cities, to build pools, shadirvans and fountains in cities, to make groundwater at low levels move to higher levels by containers, to drill wells for using underground waters (Önge, 1997).

The first water systems in Turks were uncovered in Transoxiana. The water needed by cities were brought by creating channels and waterways on streams and rivers. Big water channels were used for agricultural areas. In traditional civilizations, water is the symbol of purity, simplicity and wisdom containing a mystical purification and cleaning power in itself. In the Ottoman civilization, water became a factor bringing dynamic and independent environment of nature to inner-city through public fountains, water jets, pools, salsabil, cisterns, wells and etc. (Yüter, 2014)

Water was also regarded holy in polytheistic religions. In many cities, there were senior judges appointed for caring fountains (Wycherley, 1993). Hindus take bath in rivers during their religious rituals by believing to have peace.

The water also has an important place in Judaism. It is directly related to the creation of the world. Although it has not been recorded, we can understand that the fountain next to the Wailing Wall in Jerusalem has a religious meaning. It is significant that believers drink water from this fountain before leaving after their worship at the Wailing Wall. It is traditional for bathhouses in quarters, where Jewish people are in majority, to have a big water basin and a private room is dedicated for this. The Jewish people enter into this water basin after taking bath similar to full ablution taken by Muslims. There are customs that water accumulations

(pools) are usually made where very important events occur. It is commonly believed that pools have a curative function (Ertuğrul, 1989).

Water was considered to be holy in Christianity. Jesus said that "You could not clean your heart by washing your body". The water did not lose its holiness during the period from the baptism of Jesus Christ to Ayazma, and this holiness still goes on. Ayazmas are water resources believed to provide cure, thus, regarded holy. It is also believed by people that Ayazmas allow people to make their wishes come true, are cure for diseases, enable anybody contacting them to redeem from his/her sins.

Water is an important element in Islam as it is in other religions. It is stated in Islam's holy book Koran that creation has begun with water and every living creature has somewhat a relationship to water. "We have created all living creature from water". This civilization, enlivened with water, has regarded water as a must for cleanliness next to faith and has made water basis for its civilization (Sarı, 2016).

3. The General Characteristics of Mardin

The city of Mardin has been called by different names throughout history. The city was named after by Assyrians as Merdin, Merdi, Merdo, Mirdo, Merde, Marda, Mardin meaning castle or castles in Syriac language; by Byzantines as Maride, Mardia; by Armenians as Merdin; by Arabs as Maridin and by Ottomans as Mardin (Dolabani, 1972).

The establishment date of Mardin is not exactly known, it was dominated by following civilizations from B.C. 3000 to today: Hurrians, Akads, Babylonians, Hittites, Mitannies, Assyrians, Aramis, Meds, Persians, Seleceons, Abgars, Romans, Abbasis, Hamdanis, Byzantines, Sassanids, Marwanians, Turkmen, Seljuks, Artuks, Ayyubis, Mongolians, Karakoyunlus, Akkoyunlus and Ottomans. Mardin was conquered by Artuqids after 1071 Battle of Malazgirt and then conquered by the Ottoman Empire in 1517 as a result of the Battle of Çaldıran (Cragoe, 2011).

Mardin lived its heyday in the period of Artuqids in architectural respect. Today, most of the historical buildings in the city were built in this period. Mardin madrasahs also belong to the period of Artuqids.

The city Mardin is one of the places whose sloping lands are used very well. Its general view resembles huge stairs. Also, the streets with stairs or ramps are often confronted due to its land structure. The depth of land makes residential buildings cascaded. However, these steps are not in the form of cubic elevators, but are integrated in a way that they are positioned so as not to close each other's view (Demir, 2010) (Figure 1).

Figure 1 Views from Mardin

The city of Mardin is 1,083 meters above sea level. The features of the continental climate are seen in the city. Summers are arid and hot while winters are heavy rainy and cold (Demir, 2010)

3.1. Aqua Architectural Elements in the Historical Texture of Mardin

The architectural elements used related to water in the historical madrasahs of Mardin are fountains, salsabil, pools, shadirvans and salsabil.

It is considered that the word of "çeşme (fountain)", which is explained as a hole similar to an eye and water flowing from this hole in dictionaries, has derived from the word of "çeşm" meaning "eye" in Farsi language. Fountains are public water collection mediums made of marble, stone or similar materials as a reservoir with a pipe or a faucet for receiving water collected from a resource by a container or pipe (Önge, 1997). A fountain has following parts: water reservoir, sink, inscription, water basin and waiting platforms (Figure 2).

Figure 2 Historical Mardin Fountain

Salsabils are the most pleasant examples of the garden and water architecture of palaces, waterside residences and mansions. Salsabils look like an ornamented fountain at first glance. Water flows from a pipe at the top in salsabils. The water pours into the bottom basin by flowing as small waterfalls into the gradually made bowls on the front of the salsabil (Tayla, 2007) (Figure 3).

Figure 3 Historical Mardin Salsabil

Small fountains are little structures built at the outer court of a mosque mostly at kulliyes. These structures have an appearance facing outward. Their exterior surfaces are covered by metal bars reflecting the characteristics of their periods. Small fountains are made up of one room, and people are offered free water as charity. It is even known that sherbets were offered in religious festivals and important days (Önge, 1997).

Shadirvans are architectural structures adding value where they are both with their nice appearance and natural effect of water at narthex, they also enable Muslims to take ablution. They were mostly made of marble. (Önge, 1997) (Figure 4).

Figure 4 Historical Mardin Shadervan

Pools are very significant water architecture works mostly built at the gardens of palaces, mansions and waterside residences and reflecting the characteristics of their periods by their architecture, ornaments and water jets, and making people peaceful. The interior of many palaces, mansions and waterside residences are ornamented by pools. The pools at the yard and especially eyvans (vaulted or domed space recessed from a central hall or court) of houses with a garden in the South and Southeastern regions have an important role in becoming cool (Önge, 1997) (Figure 5).

Figure 5 Historical Mardin Pool

Gargoyles are auxiliary architectural elements directing water in places such as housetop, fount, house bath etc. from where accumulating water is

needed to be poured. Water finds its way with a chain. It is used for accumulating water, especially in regions of insufficient rain (Figure 6).

Figure 6 Historical Mardin Gargoyle

3.2. Historical Madrasahs of Mardin and Their Water Elements

There are madrasahs in Mardin, which are still surviving since the 13th century. There are seven (7) madrasahs registered at the Mardin provincial directorate of culture and tourism as follows: Şehidiye Mosque and Madrasah, Zinciriye Madrasah, Sıttı Radviyye (Hatuniye) Madrasah, Şah Sultan Hatun Madrasah, Melik Mansur Madrasah, Altunboğa Madrasah, Kasımiye Madrasah (Url-1, 2019).

The word "Medrese (Madrasah)" comes from the Arabic root of "derase" and means "a place where it is studied and a building where students live and study". The madrasahs are buildings including rooms dedicated to students studying and they have generally a yard at the middle and rooms around this yard. Students may live and sleep here and attend lessons in the mosque. There may be sometimes a shadervan at the middle of yard of madrasahs, and there is mostly a portico in front of rooms (Kansu, 1930).

The abundance of historical madrasahs in Mardin shows the importance given to education in the past in the region. When it is examined in details in madrasahs of which structural typologies are centred around the yard, water elements, bringing in sound and life to the structure, are encountered. The water elements in these madrasahs made of stone have an oasis feature and take their place in the center of structure.

3.2.1. Şah Sultan Hatun Madrasah

This madrasah, consisting of ground + 1 floor, was built at the end of the 15th century and the beginning of the 16th century. This structure with a rectangle plan was built as an addenda to a mosque. Spaces arranged

around a yard with portico was built as two-storey. Today, you can see the spaces in the north and the ruins of upstairs. The yard has a rectangle plan.

It is entered into space with a salsabil and two windows opening to the yard through a door with a drop arch on which written basmala, at the north of yard (Yıldız, 2008).

Its entrance is lancet arch and bonded with straight dimension stones. The water of fountain flows towards the south. It is entered through stairs to the fountain of which walls are made of ordered rubble stones. Water is firstly poured to a circular trough and then to the second trough with a rectangular plan (Figure 7-8).

Figure 7 Şah Sultan Hatun Madrasah Fountain and Trough (Çağlayan, 2019)

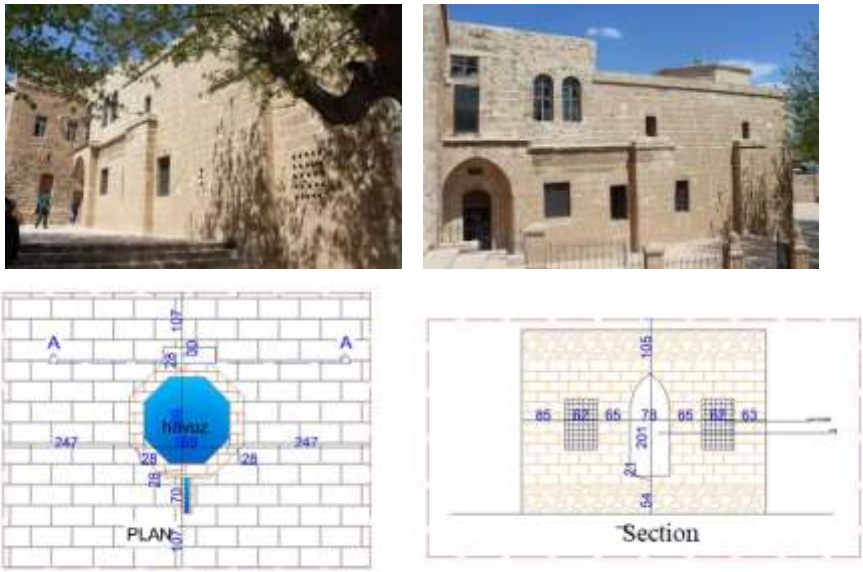

Figure 8 Şah Sultan Madrasah and pool plan- section

3.2.2. Zinciriye Madrasah

It was built by Melik Necmeddin İsa Bin Davud in H. 787/AD.1385. It has ground+1 floor. The building having a rectangular and wide-area consists of a yard, mosque, tomb and student rooms. It is a two-storey complex structure including spaces around a double yard (Yıldız, 2008).

Fountain and pool are at the center of yard. In addition, there is a fountain connected to the street at the exterior facade of the mosque. Fountains flow towards the south (Figure 9).

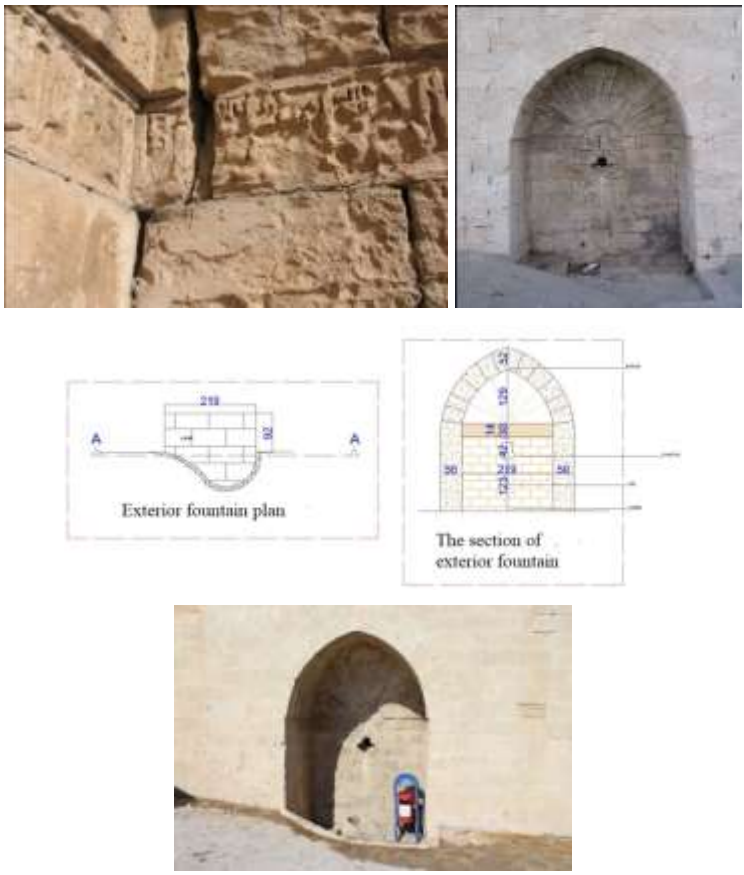

Figure 9 Fountain Plan-Section and Writing Arch at the Exterior Façade of Zinciriye Madrasah (Çağlayan, 2019)

The fountain at the exterior façade of Zinciriye Madrasah provides service for people on the street. The fountain was made of straight dimension stones. Top cover of the fountain with an archway is cradle vault. The plain façade is ornamented with stone network style. There are

ornamental writings at the end of arch along niche wall of fountain. This fountain is out of use, which still survives.

The entrance of salsabil on the north of yard is lancet arch and its top is covered by cradle vault. The salsabil is in a rectangular planned eyvan. Salsabil, made of dimension stone material, has a plain façade. Black stones on the façade and pool were added after restoration. Terraces at both sides of the rectangular bath basin may also be used as a seat. (Figure 10).

Figure 10 Yard and Salsabils at Zinciriye Madrasah

The water of salsabil flows from pipe to bath basin and then to trough and then the second trough and is finally accumulated in the pool at the yard. The water flowing in four stages is in different rhythms and gives sound to the place.

However, there is not a pool in the original plan of Zinciriye Madrasah. Water had flown from a little pool at eyvan to a fountain in the street located at the southern façade of the madrasah. The pool present at the yard of Zinciriye was added during the restoration in 2007, thus, water flowing to the fountain was cut (Soyukaya, Özgür, Kaya, 2013). It absorbs sounds to come to a classroom from outside or other classrooms, therefore, it enables students to concentrate on their lessons. It is claimed that the water of fountain represents life while the water flowing from pipe represents birth, the water from bath basin symbolizes childhood, the water from trough represents youth, the waterway between trough and pool symbolizes death, and pool represents heaven and eternal peace. The pool at the center of the yard not only moisturize the air of madrasah but also feed green plant around (Figure 11).

Figure 11 Plans and Appearances of Pool and Salsabil at Zinciriye Madrasah

Gargoyle construction elements are generally responsible for throwing rainwater out of the building. Yet, gargoyles at Zinciriye madrasah let water come into the yard, and water is collected in the pool at the yard. This water contributes to the refreshment of this place in Mardin where there is little rain.

3.2.3. Kasimiye Madrasah

It was built between 1487 - 1502. It has a plan consisting of ordered spaces around an open yard. It was built as a kulliye including a mosque,

tomb and madrasah. It has ground+1 floor on northern, eastern and western facades while it has only one floor on southern facade (Yıldız, 2008).

The water of fountain in the north of Kasımiye madrasah flows towards south. The top fountain with an entrance of lancet arch is covered by cradle vault. The facade was enriched with straight dimension stone in different colors. There is a fountain niche with a recessed stalactite. There are ornaments on the lancet arch of fountain niche. The niche arch is placed on a little pillar. There are two cup pockets on each side of the fountain niche (Figure 12).

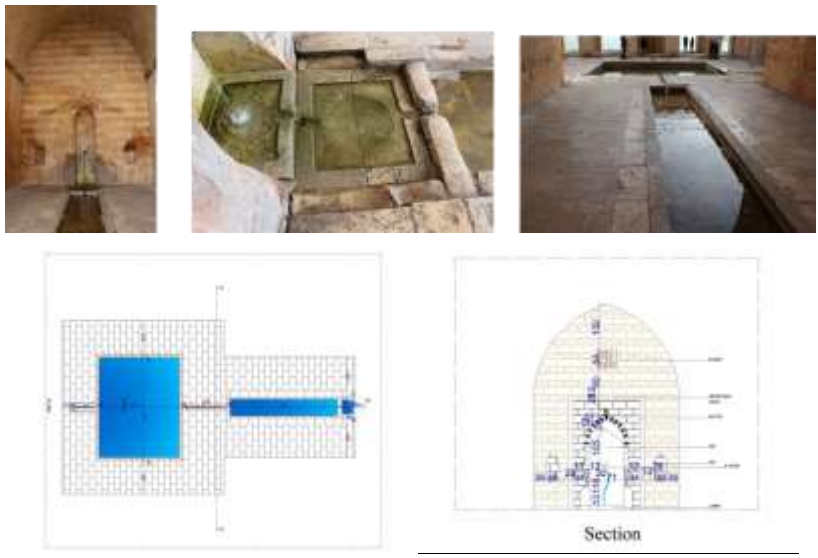

Figure 12 Kasimiye Madrasah Fountain

There is a pool at the center of madrasah. A story is told by local people on eyvan and pool. It is told that the fountain, from which the water begins to flow, symbolizes the birth, the beginning of life, this thick channel where it poured first and the water flowed slowly, and seemed stationary, represents the ages of babyhood, childhood and youth, the following thin channel, in which water flows fast, symbolizes old age and the pool in which water is collected represents the last judgment.

The water channel, beginning with the fountain at the middle of this eyvan and then reaching the pool, results in an axis dividing the madrasah into two from its yard.

It is believed that different points of pool symbolize ways to Heaven and Hell, however, “all water will reach to Mesopotamian plain and every

creature dying with the thought that it gives life to a plant will somehow find life in the plain.

It is known that pools were used in order to follow stars in the Hellenistic period. (Wycherley, 1993) (Figure 13).

Figure 13 The Pool at the Center of Kasimiye Madrasah

The eyvan with salsabil seen commonly in Mardin architecture was used not only for air conditioning and visual purposes but also for educational purposes within the scope of astronomy lessons utilizing reflections of stars on the pool (Mardin Metropolitan Municipality, 2017).

It is considered that there were pools at madrasahs, engaging in education and science, for this purpose. Roof gargoyles of madrasahs were designed so as to let water flow into the yard.

3.2.4. Altınboğa Madrasah (Tumbağa Tomb)

It was built in the middle of the 14th century in the Artuqids period. The madrasah built by Altınboğa, the Vizier of Melik Mansur Ahmet Küçük, is located at the end of dead-end street on the east of Zinciriye Madrasah (Sultan İsa). The madrasah is devastated.

A deep eyvan, used as a fountain, and some other marks are only ruins of the madrasah. The eyvan is in 2.80 x 4.70 m with a rectangular plan enlarging from south to north and covered by cradle vault in the same direction.

The eastern wall of eyvan was enriched by a lancet niche in 0.90 x 2.20 m. There is a door, opening to a water reservoir, in 1.15 m height and 0.90 m width and in rectangular form, on top of pipe. The work was made of broken stone materials and is plain (Çağlayan, 2019).

After the entrance section remaining high, a deep room at the left covered by cradle vault and reached by ascending a few stairs is seen. The eyvan arch takes a step in front of this room and then arrived at the section descended by two stairs.

There are wide niches with deep lancet arches on the left and right of this section considered to have a fountain and in the form of an salsabil. Eyvan vault is narrower and covered by a cradle vault in the same direction. The reservoir of the fountain is at the back. There is a ruin of a door on the south of the eyvan of this fountain (Figure 14).

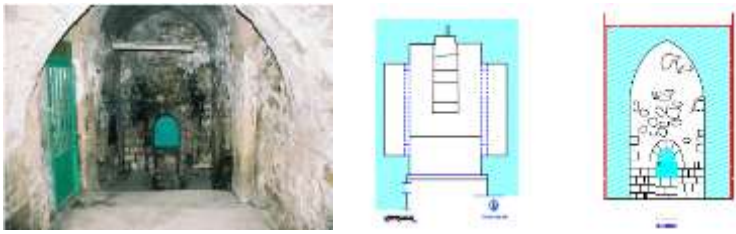

Figure 14 The Fountain of Altınboğa Madrasah (Tumbağa Tomb) (Çağlayan, 2019)

The wide gate post is softened by a stalactite and there are ornaments with vegetative curves on stones out of this structure. It is understood from the door ruins on the south that this place, today called Altın Boğa Fountain, is not a fountain. It is seen that half of the arch on the west of corridor of vaulted eyvan is filled. There is a lighting hole at the top cover of the tomb (Yıldız, 2008).

3.2.5. Şehidiye Madrasah

Şehidiye Madrasah was built by Nasreddin Artuk Arslan, an Artuquid ruler, in the early 13th century. (Yıldız, 2008). There is an eyvan with a salsabil, of which water flows towards the south, on the north of yard. The entrance is lancet arch and its top is covered by cradle vault. It was bonded by straight dimension stone, including its vault. The niche of salsabil has four centers, an arch and recessed stalactite. The niche arch is lancet and ornamental. Arch ornaments are placed on a little pillar. There are ornaments around niche till ceiling. There is a Maliki script on the niche arch (Figure 15).

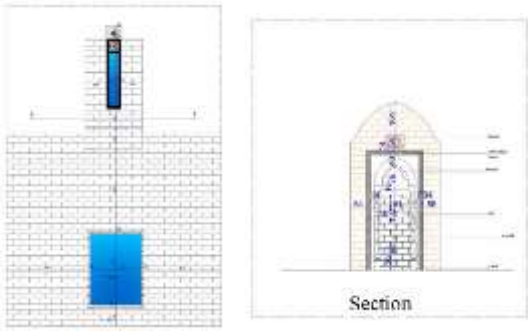

Figure 15 The Salsabil Şehidiye Madrasah

There is an eight-strand star on the ground of bath basin. There is a trough with sixteen-strand and star ornamented at the following section of bath basin. (Figure 16).

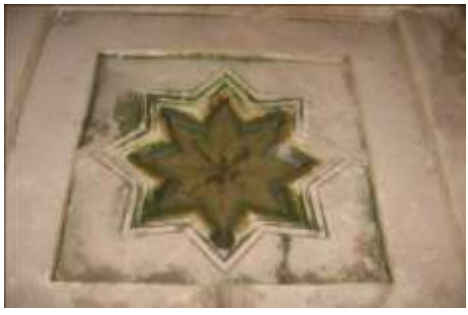

Figure 16 Details of Bath Basin at Şehidiye Madrasah

The water flowing from pipe goes to bath basin and then trough and finally the second trough. The difference in flow distances of water creates different rhythms in water sound. The rhythmical water sound from Salsabil functions as sound insulation (Figure 17).

Figure 17 Details of Trough at Şehidiye Madrasah

4. CONCLUSION

Human being needs water, which is vital for people, due to physical, psychological and architectural purposes. As a result of these needs, different techniques are applied to water in different fields so as to benefit from it. In this study, the use of water in madrasahs were emphasized along with its benefits in educational buildings.

Madrasahs are educational and scientific places. Madrasahs are mostly considered to have the characteristics of religious structures. When detailing these buildings, it is seen that they were designed for a functional education. Since water-related elements generally flow towards south.

The madrasahs, built in the Artuqids period and still surviving, show the importance given to education by Artuqids. It is not known whether the reason for the absence of madrasahs belonging to the Ottoman period is due to the fact that the existing madrasahs were considered sufficient or because the Ottoman Empire did not attach the necessary importance to education.

This research concludes that the water architecture was not only performed for ornamental purposes but also educational, psychological and physical needs. It is argued in this research carried out on the historical madrasahs that water may also be used in the same purposes. The water elements, which are not used sufficiently in today's educational institutions, can be used in this respect.

5. References

Cragoe C.D. (2011), How to Read Buildings? / Picture Building Reading Guide, Yem Publishing, İstanbul.

Çağlayan M. (2019), An Architectural Comparison: Zinciriye and Kasimiye Madrasahs in Mardin, Traces of History from the Early Ages to the Modern Period II, Editors Prof. Dr. M. Doğan KARACOŞKUN Prof. Dr. Osman Köse, Berikan Publishing, ISBN: 978-605-7501-36-3.

Demir M.M. (2010), Mardin City, İstanbul University, Social Sciences Institute, İs-tanbul.

Demirağ D., Erten A., & Şen M. (2008), Culture coming with Water, İski, transfer Yüter, F.Z. (2014), Water Architecture and Shadervan Fountains in Istanbul, Haliç University, Institute Of Natural And Applied Sciences.

Dolabani H. (1972), Mardin in History, Deyrulzafaran Monastery Publications, pp: 195, İstanbul.

Ertuğrul Ö. (1989), The Aqua Architecture of the Byzantine Period in Istanbul, Phd Thesis, İstanbul University, Social Science Institute, İstanbul.

Kansu A.N. (1930), History of Education in Turkey, Muallim Ahmet Halit Bookstore, İstanbul.

Mardin Travel Guide, (2017). Publication of Mardin Metropolitan Municipality, Culture Tourism and Social Affairs Department, November 2017.

Önge Y. (1997), Water Structures in Seljuk and Ottoman Periods in Turkish Architecture, Turkish History Association, Ankara

Sarı İ. (2016), All Omans Water, Nokta Publishing, İstanbul.

Soyukaya N., Özgür M., Kaya F. (2013), Mardin Cultural Inventory, Mardin Governorship & Çekül, İstanbul.

Tayla H. (2007), Building Systems and Elements in Traditional Turkish Architecture, Taç Vakfı Publications, Vol:1 İstanbul.

URL-1. The Ministry of Culture and Tourism of the Republic of Turkey, Mardin Provincial Culture and Tourism Directorate, Mosque - Madrasa and islamic-ottoman social complexes, http://www.mardinkulturturizm.gov.tr/TR,56509/camiimedrese-ve-kulliyeler.html (E.T. 27 Aralık 2019).

Wycherley R.E. (1993), How Cities were Established in Ancient Times? Archeology and Art Publications, İstanbul.

Yıldız İ. (2008), Aqua Architecture in Mardin, Yüzüncü Yıl University, Social Science Institute, Van.

Yüter F.Z. (2014), Water architecture and shadervan fountains in Istanbul, Master Thesis, Haliç University, Institute Of Natural And Applied Sciences, İstanbul.

CHAPTER VI

SUSTAINABLE URBAN RENEWAL PROCESS AND ASBESTOS FACTOR

Gülferah ÇORAPÇIOĞLU

(Asst. Prof. Dr.); Istanbul Arel University
e-mail: gulferahcorapcioglu@arel.edu.tr
https://orcid.org/0000-0002-4748-3009

Sabit OYMAEL

(Prof. Dr) Istanbul Arel University
e-mail: sabitoymael@arel.edu.tr
https://orcid.org/0000-0003-2632-1139

1. Introduction

Asbestos is a natural mineral with a fibrous structure that is formed when various silicate minerals are exposed to high pressure, temperature and chemical impacts. It is medically proven to be cancerogenic, and its use in especially the shipping, automotive and construction sectors due to its impermeability and insulating properties constitutes such a serious problem that it is in Group 1 of the list of Agency for Research on Cancer, and is defined as carcinogenic (WHO, 2009). According to scientific findings, the fibers have a low release probability, however when asbestos-containing materials are subjected to repair, damage or disassembly, and when weather conditions permit, the spread of asbestos fibers is possible. When such fibers are released for any reason, the risk of the development of diseases related to asbestos increases (Üzmezoğlu &Töreyin, 2017). The first country to restrict the production and use of asbestos was Iceland (1983), and the United Kingdom completely banned the use of asbestos in 1999 (Akboğa et al., 2017). Its use was banned in the EU member states after 'Regulation (EC) No 1907/2006 of the European Parliament of 18 December 2006 concerning the Registration, Evaluation, Authorisation and Restriction of Chemicals' came into effect (01.06.2007) (ECHA, 2006). In Turkey, with the revision in 2010 of the Regulation on the Restrictions Relating to the Production, Supply to the Market and Use of Certain Hazardous Materials, Products and Goods, published in the Official Gazette (dated 26.12.2008, No. 27092), the launching, processing,

sale, import and production of all types of asbestos and asbestos products were banned (Resmi Gazete, 2010), although banning asbestos does not necessarily eliminate the problem. According to research, 500,000 tonnes of asbestos were used in many products between 1983 and 2010 in Turkey, and its deleterious effects still pose a threat when there is a need to maintain, repair, disassemble, demolish and transport these products. As exposure to this substance increases, so does the likelihood of developing a disease (Topçu, 2002).

There are two types of asbestos minerals with the $Mg_3[Si_2O_5](OH)_4$ compound – serpentine and amphibole. Minerals from the serpentine group are defined as chrysotile (white asbestos) CAS No12001-29-5, CAS No132207-32-0, while minerals from the amphibole group are defined as crocidolite (blue asbestos) CAS No12172-73-5, amosite (brown asbestos) CAS No12172-73-5, actinolite (green asbestos) CAS No77536-66-4 and tremolite (white-gray) CAS No77536-68-6 (Thompson, 1982). It has been suggested that there are approximately 113 asbestos deposits in Turkey, 65 percent of which are chrysotile, 39 percent are tremolite and 1 percent are crocidolite (Müller & Fischer, 2000). Asbestos fibers have been used in the production of many cement composites due to their chemical structure and their resistance to alkali environments (Ersoy, 2001). Chrysotile (white asbestos) in particular has a binding characteristic and can absorb such organic substances as resin and polymer (Akboğa et al., 2017). During our research, chrysotile (white asbestos) was found in some concrete pipes in Istanbul.

With the adoption of the Law on Converting of Areas Under Disaster Risk dated and numbered 16.05.2012/6306 and its related regulation, the urban renewal process began on 04.08.2012, and this led to the renewal of old structures in areas where there is a high risk of earthquake. Urban renewal projects, although aimed at creating healthy and livable cities, come with adverse environmental problems on national and international scales. The disassembly of construction components containing asbestos comes with occupational and non-occupational environmental asbestos problems. Based on the findings in literature regarding the delay in the appearance of the consequences of asbestos exposure on human health, it is apparent that the problem will prevail for years to come, despite the bans and restrictions.

Contemporary studies aimed at decreasing and managing the adverse effects of asbestos and other air pollutant wastes resulting from disassembly and the recycling of hazardous waste have provided useful perspectives on the matter. In one study it is stated that conducting an environmental impact assessment (EIA) prior to embarking on the

disassembly and demolition of structures, using parameters such as soil, water and energy resources, adverse environmental effects resulting from the process could be decreased by at least 50 percent (Ding et al., 2016). In a similar study, Kobeticov et al. (2017) address the current methodologies with a critical approach in their analysis of the adverse effects of construction materials on the environment. In a study determining the factors affecting building demolition and waste management in Hong Kong, Chen et al. (2017) put forward suggestions to minimize the processes and costs. Wang et al. (2017) carried out a case study on lifecycle and building information modeling in which they took into account carbon emissions from wastes, and found that metal waste could prove to be more useful in recycling, and that decreasing aluminum carbon emissions in particular could contribute to recycling as much as 45 percent. Studies on asbestos-containing waste, which is considered a threat for human health and environment around the world, are regarded as expensive and difficult hazardous materials to research (Zimmer & Ha, 2017). There are studies that emphasize the fact that the issue of hazardous waste storage should be addressed when dealing with the disposal of waste containing asbestos, but should be based on a recycling and reuse approach. Iwaszko et al. (2018) claim that asbestos fiber structures can be broken down through exposure to thermal impact, that different calcium silicate phases may be formed under suitable cooling conditions, and that high-energy milling could be a solution. The international trade of asbestos constitutes a further problem.

In line with the exclusion of chrysotile from hazardous substance classification in international asbestos trade, Taşbaşı et al. (2017). draws attention to the laws and regulations related to the cross border transportation of hazardous substances and wastes and their control [16]. Demolition of buildings and waste management issues should be approached by experts from different disciplines within the frame of "sustainability" and should be investigated at national and international scale in terms of their social, economic and environmental aspects.

Urban renewal projects, which have gained prominence especially in large cities in recent years, aim to transform settlement dynamics and structures, however environmental sustainability is ignored during the process. According to urban renewal legislation related to the Regulation on the Control of Excavation Soil and Construction and Demolition Waste, while an Asbestos Inventory Report must be prepared and asbestos-containing materials must be disassembled and removed from the site before demolition, according to related regulations, the environmental health problems resulting from transformation processes are up for discussion.

The purpose of this study is to conduct a research based on tangible data regarding the existence, impact and severity of asbestos in building demolitions within the scope of urban renewal in Turkey. To this end, an experimental study is made of residential buildings in the process of demolition in Istanbul-Kadikoy, where the prevalence of urban renewal related demolitions and restorations has been increasing rapidly since 2012. In addition, observations are made regarding the compliance of the demolition, disassembly and waste removal activities with current regulations.

2. Material and Method

2.1. Examination of legislation

The study contains an analysis of the legislation and regulations related to urban renewal, building demolition and waste that have been published in the Official Gazette, including the "Regulation on Environmental Impact Assessment" dated and numbered 25.11.2014/29186, and the "Waste Management" regulation, dated and numbered 02.04.2015/ 29314 of the Ministry of Environment and Urban Planning. In addition, current practices in the Kadikoy district of Istanbul have been evaluated in line with the regulation on "Health and Safety Measures with respect to Asbestos", dated and numbered 25.01.2013/28539, and the regulation on "Occupational Health and Safety in Construction Work", dated and numbered 05.10.2013/28786, of the Ministry of Labor and Social Security (Resmi Gazete, 2014, 2015, 2013/01, 2013/10).

2.2. Experimental studies

In the experimental study conducted to detect whether the demolition of buildings containing materials with asbestos content, samples from a large number of construction materials were collected through a random sampling method from three residential buildings located on Fahrettin Kerim Gokay Street in the Zuhtu Pasa neighborhood of the Istanbul-Kadikoy district, which was built prior to 1970 and is now undergoing urban renewal. As seen in Appendix A, the number of samples was reduced to 17, which were then sent to an accredited laboratory in plastic packaging. The site and environmental conditions during the sampling were not extraordinary, and sampling was carried out in accordance with the regulation on "Health and Safety Measures with respect to Asbestos" and "HSG 248-A2: Asbestos: The Analysts' Guide for Sampling, Analysis and Clearance Procedures". A polarized light microscopy (Nikon/Eclipse, 200 MV POL) was used on all asbestos-type detection analyses for the solid samples (agt. Vonka Lab). The results of the analysis were evaluated taking into account the presence and type of asbestos minerals.

3. Results

Different types of asbestos have different fiber structures, which are viewable under a microscope. The mineral images to be used as a reference are provided in Figure 1.

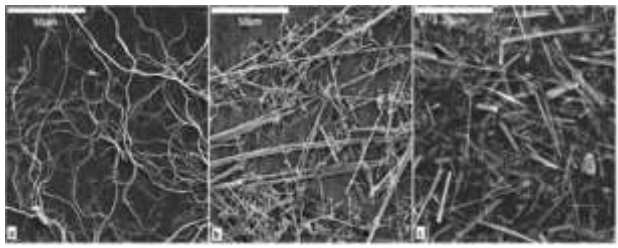

Figure 1. Fiber structures of different asbestos minerals under scanning electron microscope (μm): a. chrysotile b. crocidolite c. Amosite (Barlow et al., 2017).

The results of the analysis of the 17 samples were tested for the presence and type of asbestos mineral. Following the SEM analysis, chrysotile-type asbestos fibers were detected in a 1.8 pipe concrete pipe sample (S108.8) that was taken from the basement of Building no. 1, with no asbestos found in the remaining 16 analyzed samples (Appendix A). This result, which reflects the status of the structure at the time of the evaluation, should be revised in the event of a significant change in the structure or any of the equipment contained within the buildings. The SEM images of chrysotile-containing material sample no. (S108.8) are presented in Figure 2, and the fiber structure of the said material corresponds to Figure 1.a.

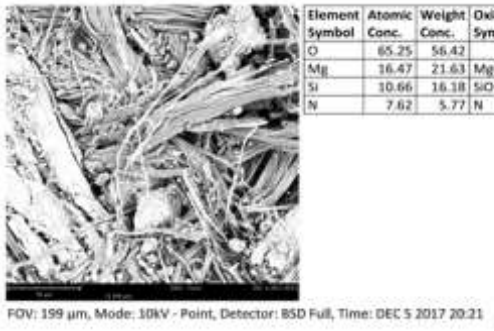

Element Symbol	Atomic Conc.	Weight Conc.	Oxide Symbol	Stoich. wt Conc.
O	65.25	56.42		
Mg	16.47	21.63	MgO	47.03
Si	10.66	16.18	SiO_2	45.40
N	7.62	5.77	N	7.57

Figure 2. SEM analysis of concrete pipe No. S108.8. [Report, 05.12.2017]. (Agt, Vonka, 2017).

Asbestos fibers, which have different internal structures according to the mineral type, in addition to their contribution to internal tensile forces, also offer the advantage of durability against externally affecting acidic

and sulfate-based materials. The hazardous chemical materials in question would have the highest impact on concrete pipes containing cement and asbestos fibers. In the Kadikoy district, where all the analyzed and sampled buildings are located, applications for urban renewal compliance certificates are first directed to the Directorate of Environmental Protection and Control, and experts from this directorate carry out site controls of the building to be demolished and collect samples for analysis using statistical methods. The collected samples are analyzed by laboratories with ISO/IEC 17025 accreditation and an asbestos inventory report is created. The report includes data of the lab results, building description, analysis method, location and approximate amounts of asbestos-containing materials. If no asbestos is identified in the report, a certificate of compliance for urban renewal is granted to the applicant company, and if asbestos is detected, the materials must be removed using personal protective equipment in accordance with the criteria in the Regulation on Health and Safety Measures with respect to Asbestos. The resulting waste must be packaged in accordance with the regulation and disposed of with a national waste transportation form (Kadiköy Belediyesi, 2012). Asbestos is defined as "asbestos-containing construction materials with code no. 17 06 05" on the list of waste hierarchy in the Regulation on Hazardous Waste Control of Ministry of Environment and Forestry, and is a class-1 hazardous waste that requires systematic storage (Resmi Gazete, 2005).

4. Discussion and Conclusion

According to Kadikoy district regulations, asbestos-containing wastes are disposed of at a class-1 systematic storage unit located in Sile Komurcuoda, (İstaç, 2008) meaning that asbestos-containing materials are expected to become harmless. An Asbestos Inventory Report is required to be submitted in the event of building demolition in seven municipalities: Kadikoy, Besiktas, Sisli, Maltepe, Atasehir, Tuzla and Bagcilar, out of the 39 municipalities in İstanbul. According to April 2017 data from the Kadikoy Municipality, where the implementation is mandatory, 1,517 construction sites have been inspected since the asbestos inspection process started in 2015, leading to the identification of asbestos-containing materials in 446 buildings and the disposal of a total of 498.5 tonnes of asbestos waste.

Looking at the results of the air quality measurements in Kadikoy, it is observed that the values are much higher than international standards. The World Health Organization (WHO) states that the 24-hour limit value for (PM10) is 50 µg/m3 and 25 µg/m3 for (PM2.5); however, the values in Kadikoy-Fikirtepe have been measured at 145.85 µg/m3 and 91.86 µg/m3, respectively (Kadıköy Belediyesi, 2017) –much higher than the WHO

values – and should be considered as posing a serious threat to human health. The danger to environmental health associated with asbestos becomes clearer when it is considered as stated by Ersoy (2001), that asbestos fibers with a diameter of as little as 0.01 μm. Üzmezoğlu and Töreyin (2017) found out that when released into the air, can reach the respiratory tract and accumulate in the lung tissue, and the risk of disease increases proportional to the amount of asbestos fibers. Asbestos is highly resistant to temperature, and its adverse environmental effects cannot be eliminated, even by fire.

Based on the fact that approximately 90 demolition permits are granted monthly in Kadikoy, and that five or six buildings may be being demolished on a single city block at the same time, the management of demolition and hazardous waste needs to be taken much more seriously. There was no trace of asbestos, aside from the concrete pipe in the S108.8 sample, in the sample analysis carried out within the scope of this study. As seen in Appendix A, no findings indicating the existence of persistent organic pollutants – the use of which is banned and limited due to their adverse effects on environmental and human health – aside from asbestos were obtained. In line with these results, during the urban renewal process, it is vital that more comprehensive studies are carried out, not only related to asbestos, but also on the mitigation of other adverse environmental impacts on air quality.

There are ongoing studies around the world into such topics as the mitigation of the adverse environmental effects of building demolition, waste sorting and recycling, minimizing demolition processes, planned demolition, waste management and improvements to air quality. In addition, it is observed that these studies are conducted with higher scale designs in most countries. The air quality limit values set out in the Regulation on Air Quality Assessment and Management by the Ministry of Environment and Urbanization in Turkey are not compatible with those of the European Union or the World Health Organization, and while these values are expected to become compatible, it can be observed that the action plans directed towards this purpose are not being executed and the current laws are not being enforced due to a lack of inspections. In parallel to the rapid urban renewal process, it is necessary to keep in mind that environmental problems should be addressed with a serious approach, and that this responsibility falls upon the respective ministries and local administrations.

Opinions and objectives aimed at maintaining economic development in the world in accordance with sustainable life limits are stated by international organizations that deal with global environmental issues, such

as the United Nations Environment Programme (UNEP) and the European Union (EU). It is emphasized that studies into this subject should be the main concern of governments, planners, architects, preservationists and groups of experts from different disciplines. It should further be kept in mind that success can only be achieved if urban renewal is handled through an integrated approach, and with the aim of preserving the entire set of balances of a city. In this study, asbestos is examined within the context of the urban renewal process and the environmental effects, and is discussed within the framework of literature review data, experimental study results, observations and related legislations. The study is expected to raise awareness about the subject and to provide data for future studies. It would be beneficial to take into consideration the following suggestions to ensure a livable and sustainable environment:

- Creating awareness of living in a healthy environment across the society, educating future generations on the subject, and conducting joint activities between non-governmental organizations and public institutions,
- Taking control of the urban renewal process, ensuring compliance with legislation and putting into force a more effective inspection mechanism,
- Taking global standards related to demolitions and waste management as an example, transforming recycling and disposal processes into production from waste programs,
- Taking the asbestos factor into account in air quality measurements, and focusing on the sources of pollution,
- Measuring concentrations of asbestos in the air that workers are exposed to under the "Regulation on the Control of Excavation Soil and Construction and Demolition Waste", dated and numbered 18.03.2014/25406, and complying with the criteria that levels do not exceed 0.1 fiber/cm³ in an 8 hour period,
- Health and environment experts to conduct joint studies to identify the impact of demolitions as part of urban renewal projects on diseases caused by asbestos,
- Conducting asbestos scanning of construction materials and industrial material production sources, industrial buildings, and asbestos-containing floors rather than buildings, and mapping asbestos sources.

References

Agt-Vonka. (2017). SEM Analizi Sonuçları, (Rapor- 05.12.2017). Agt, Vonka Laboratuarı, İstanbul.

Akboğa-Kale, Ö., Gürcanlı, G. E., Baradan, S. (2017). Kentsel dönüşüm sürecinde asbest maruziyeti ve alınması gereken önlemler. *Pamukkale Üniversitesi Mühendislik Bilimleri Dergisi*, *23*(6), 694-706.

Barlow, C. A., Sahmel, J., Paustenbach, D.J., Henshaw, J. L. (2017). History of knowledge and evolution of occupational health and regulatory aspects of asbestos exposure: 1900–1975. *Journal of Critical Reviews in Toxicology: 4*, 286-316.

Chen, X., Lu, W. (2017). Identifying factors influencing demolition waste generation in Hong Kong. *Journal of Cleaner Production 141,* 799-811.

Çevre ve Şehircilik Bakanlığı. (2008). Hava Kalitesi Değerlendirme ve Yönetimi Yönetmeliği. https://www.csb.gov.tr/db/cygm/editordosya/YON26898HavaKalitesi.

Ding, Z., Wang, Y., Zou, P.X.W. (2016). An agent based environmental ımpact assessment of building demolition waste management: conventional versus gren management. *Journal of Cleaner Production 133*, 1136-1153.

Ersoy, H.Y. (2001). *Kompozit Malzemeler*. Literatür Yayıncılık.

European Chemicals Agency. Reach Legislation. (2006). https://echa.europa.eu/regulations/reach/legislation.

İstaç. Endüstriyel Atık Yönetimi. (2008). http://www.istac.istanbul.

İstanbul Asbest Raporu. (2018). TMMOB Çevre Mühendisleri Odası İstanbul Şubesi. https://www.tmmob.org.tr/sites/www.tmmob.org.tr/files/ikk_asbest_raporu_sayfalar_baski.pdf.

Kadıköy Belediyesi. Çevre Koruma ve Kontrol Müdürlüğü. (2012). Binalarda Asbest Atıklarının Kontrolü. http://www.kadikoy.bel.tr/Kurumsal/Mudurlukler/cevre-koruma-ve-kontrol-mudurlugu.

Kadıköy Belediyesi. (2017). www.ebelediye.info/.../fikirtepe-deki-hava-kalitesi-olcum-sonuclari.

Resmi Gazete. (2005). Tehlikeli Atıkların Kontrolü Yönetmeliği. http://www.resmigazete.gov.tr/eskiler/2005/03/20050314-1.htm.

Resmi Gazete. (2010). Bazı Tehlikeli Maddelerin, Müstahzarların ve Eşyaların Üretimine, Piyasaya Arzına ve Kullanımına İlişkin Kısıtlamalar Hakkında Yönetmelik. www.resmigazete.gov.tr/eskiler/2010/08/20100829-3.

Resmi Gazete. (2013). Asbestle Çalışmalarda Sağlık ve Güvenlik Önlemleri Hakkında Yönetmelik. www.resmigazete.gov.tr/eskiler/2013/01/20130125-24.htm.

Resmi Gazete. (2013). Yapı İşlerinde İş Sağlığı ve Güvenliği Hakkında Yönetmelik. www.resmigazete.gov.tr/eskiler/2013/10/20131005.htm.

Resmi Gazete. (2014). Çevresel Etki Değerlendirmesi Yönetmeliği. www.resmigazete.gov.tr/eskiler/2014/11/20141125.htm.

Resmi Gazete. (2015). Atık Yönetimi Yönetmeliği. http://www.resmigazete.gov.tr/eskiler/2015/04/20150402-2.htm.

Iwaszko, J., Zawada, A., Lubas, M. (2018). Influence of high-energy milling on structure and microstructure of asbestos-cement materials. *Journal of Molecular Structure, 1155*, 51-57.

Kobeticov, K., Cerný, R. (2017). Ecotoxicology of building materials: a critical review of recent studies. *Journal of Cleaner Production, 165*, 500-508.

Müller KM, Fischer M. (2000). Malignant pleural mesotheliomas: an environmental health risk in Southeast Turkey. *Journal of Thoracic Medicine*. *67*(6), 608-609.

Taşbaşı, A., Sarıca, Y.P., Sabah, S. (2017). Uluslararası asbest ticareti. *İş Sağlığı ve Türkiye, Çalışma ve Toplum Dergisi, 4*, 2003-2040.

Thompson, C.S., Levadie, B.(ed). (1982). *Consequences of using ımproper definitions for regulated minerals, definitions for asbestos and other health-related silicates*. ASTM Technical Publication.

Topçu, F. (2002). Asbest ve plevra. *Solunum Dergisi (Eurasian Journal of Pulmonology), 4* (Ek 1), 144-148.

Üzmezoğlu, B., Töreyin, N.Z. & Bayram, H. (Ed). (2017). *Asbest nedir? Asbestin sağlık üzerine etkisi*. Türk Toraks Derneği Eğitim Kitapları.

Wang, J., Wu, H., Duan, H., Zillante, G., Zuo, J., Yuan, H. (2017). Combining life cycle assessment and building ınformation modelling to account for carbon emission of building demolition waste: a case study. *Journal of Cleaner Production, 1*-13.

WHO (World Health Organization). (2009). International agency for research on cancer, ıarc strengthens ıts findings on several carcinogenic

personal habits and household exposures, France. https://www.iarc.fr/en/mediacentre/pr/2009/.../pr196_E.pdf.

Zimmer, A.T., Ha, H. (2017). People, planet and profit: unintended consequences of legacy building materials. *Journal of Environmental Management, 204*, 472-485.

Appendices

Appendix A. SEM (Scanning Electron Microscope) Analysis Table of Samples.

No	Sample No	Sample Type / Sampling Point		SEM	El. Symbol	Atomic Conc. (%)	Weight Conc.(%)	Oxide S.	Stoich. wt Conc. (%)	Asb. Presence
1	S108.1	[1.1] Fiberglass/ water tank / Building no. 1/basement		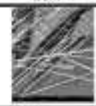	Si	50.21	47.79	SiO2	56.35	Asb. not found
					Mg	28.81	23.73	MgO	21.69	
					Ca	20.97	28.48	CaO	21.96	
2	S108.2	[1.2] Tile adhesive / Building no. 1/first floor		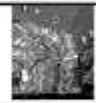	O	61.43	47.47			Asb.not found
					Si	16.86	22.87	SiO2	53.07	
					Mg	14.70	17.26	MgO	31.04	
					S	4.11	6.36	S	6.90	
					Ca	2.32	4.49	CaO	6.81	
					Fe	0.58	1.56	FeO	2.18	
3	S108.3	[1.3] Rubber section / Building no.1/second floor		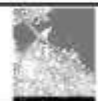	O	72.83	60.77			Asb.not found
					Na	12.83	15.38	Na2O	42.74	
					S	9.47	15.84	S	32.66	
					Mg	3.43	4.35	MgO	14.88	
					Ca	1.28	2.68	CaO	7.72	
4	S108.5	[1.5] Asphalt / Building no.1- Parking area slab			O	47.43	36.79			Asb.not found
					C	28.53	16.62	C	20.51	
					Ca	21.79	42.33	CaO	73.14	
					K	2.25	4.26	K2O	6.34	
5	S108.6	[1.6] Electrical plastic tubing / Building no. 1/basement		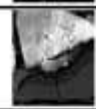	C	85.04	81.02	C	100.00	Asb.not found
					O	14.96	18.98			
6	S108.7	[1.7] Glass cement (white)/Building no.1/second floor			O	84.37	69.51			Asb.not found
					Ca	12.76	26.33	CaO	80.54	
					Si	2.88	4.16	SiO2	19.46	
					Mg	0.00	0.00	MgO	0.00	
7	S108.8	[1.8] Concrete pipe/ Building no. 1/basement			O	65.25	56.42			Asb. found
					Mg	16.47	21.63	MgO	47.03	
					Si	10.66	16.18	SiO2	45.40	
					N	7.62	5.77	N	7.57	
8	S108.9	[2.1] Electrical plastic tubing / Building no. 2/basement			C	63.13	56.73	C	91.32	Asb.not found
					O	33.70	39.10			
					Ca	1.05	3.05	CaO	6.87	

No	Sample No	Sample Type / Sampling Point		SEM	El. Symbol	Atomic Conc. (%)	Weight Conc.(%)	Oxide $.	Stoich. wt Conc. (%)	Asb. Presence
9	S108.10	[2.2] Lime mortar/ Building no. 2/first floor			O	77.48	58.64			Asb.not found
					Ca	20.19	38.27	CaO	91.47	
					Si	0.85	1.13	SiO2	4.13	
					Mg	0.82	0.94	MgO	2.67	
					S	0.67	1.01	S	1.73	
10	S108.11	[2.3]Translucent acrilyc /Building no. 2-Parking area roof		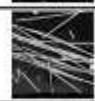	O	66.84	50.78			Asb not found
					Si	17.91	23.88	SiO2	56.61	
					Ca	9.32	17.73	CaO	27.48	
					Al	5.93	7.60	Al2O3	15.90	
11	S108.12	[2.4] Vinyl floor covering/Building no.2/second floor			O	45.96	23.73			Asb.not found
					Ca	34.35	44.41	CaO	84.77	
					S	13.09	14.18	S	14.75	
					Sb	4.00	15.72	Sb	16.17	
					Si	1.82	1.65	SiO2	3.68	
					Fe	0.18	0.32	FeO	0.42	
12	S108.13	[2.5] Plank flooring adhesive/Building no.2/second floor			C	44.41	39.10	C	56.50	Asb. not found
					N	29.33	30.11	N	43.50	
					O	26.26	30.79			
13	S108.14	[2.6] Poliester water tank/Building no.2/basement			O	81.27	66.85			Asb.not found
					Ti	9.83	23.61	Ti	55.05	
					Si	3.58	5.04	SiO2	25.15	
					Al	3.32	4.50	Al2O3	19.81	
14	S108.16	[3.1] Rubber mat/ Building no.3/basement			O	50.58	49.12			Asb. not found
					C	36.17	26.37	C	36.39	
					Si	7.63	13.01	SiO2	38.41	
					Ca	2.87	6.99	CaO	13.49	
					Al	2.73	4.47	Al2O3	11.64	
15	S108.17	[3.2] Electrical plastic tubing /Building no.3/basement			C	100.00	100.00	C	100.00	Asb.not found
16	S108.18	[3.3] Concrete/Building no.3/ first floor			O	65.18	38.27			Asb. not found
					Ca	27.79	40.87	CaO	70.03	
					Sb	3.96	17.70	Sb	21.67	
					Si	3.07	3.17	SiO2	8.30	
17	S108.19	[3.4] Vinyl floor covering/Building no.3/second floor			C	34.96	15.84	C	15.19	Asb. not found
					Ca	32.02	47.80	CaO	64.94	
					O	27.00	16.09			
					Sb	3.97	18.03	Sb	17.50	
					S	2.04	2.44	S	2.37	

CHAPTER VII

A COMPREHENSIVE OPTICAL LOSS ANALYSIS OF A LINEAR FRESNEL REFLECTOR-PHOTOVOLTAIC HYBRID SYSTEM WITH COMPUTER AIDED DESIGN

Keziban CALIK

Istanbul Technical University, Energy Institute, keziban.calik@gmail.com
Orcid: 0000-0003-1348-3358

Coskun FIRAT

(Dr.); Istanbul Technical University, Energy Institute, coskun.firat@itu.edu.tr
Orcid: 0000-0002-2853-8940

1. Introduction

The optical efficiency of a linear Fresnel reflector (LFR) system which can be defined as the ratio of the amount of solar radiation falling on the receiver to the incoming solar radiation on the reflectors, is greatly dependent on the system configuration. Besides the roughness of the mirror surface, when an LFR system configuration made by considering the parameters such as the mirror width (W), the distance between the mirrors (S), the distance of each mirror to the tower (Q), the width of the receiver (W_r), the height of the receiver (f) is not correct, then a serious decrease in the overall system efficiency is observed due to optical losses. Optical losses in LFR systems occur due to the mirrors shading and blocking each other, the receiver shadow on the mirrors, the end losses and the edge losses on the receiver. In systems with single axis solar tracking such as LFRs, the cosine losses (transversal and longitudinal) are inevitable because the incoming sun rays and the normal of the mirror surfaces might not be in the same direction and because the mirrors don't track the sun in north-south direction as well.

To determine the optical efficiency in terms of the loss mechanisms before constructing a linear Fresnel reflector system provides a very important information on an optimum configuration. There are many studies in the literature on determining the structure and the optical losses in LFR systems. These studies are either done by using ray tracing software or geometrical relationships between the optical parameters. The optical losses are given inside the optical efficiency in most of the studies but not as the amount of the lost itself. Therefore, to understand the optical losses in details needs further researches.

The detailed expression on optical parameters for LFR systems is done by Mathur et al. (1991a, 1991b). The LFR systems employing mirror elements of both varying and equal width for three different absorber configurations are analyzed in the study. In their study, the distribution of the local concentration ratio on the surfaces of the absorbers has been investigated using the ray trace technique. However, no any details about the optical losses were given. Gouthamraj et al. (2013), have discussed the design of a rooftop LFR solar concentrator module in terms of geometrical parameters of the mirrors. However, there was no any detail about the optical losses. In the study done by Gordon and Ries (1993), it was proposed a new design concept for secondary concentrators that was tailored to Fresnel reflector and analyzed the optical parameters however there was no given detail on optical losses. Beltagy et al. (2017), have presented a theoretical and experimental study of a prototype using Fresnel type concentrator. In the study, the power received by the solar field was calculated by considering the losses of cosine effect, shading of mirrors and shading of the receiver. The results were verified experimentally however, there was no detail about the losses. Zhu and Huang (2014) have proposed a semi-parabolic linear Fresnel reflector solar concentrator. To avoid the shading and blocking effects of the adjacent mirrors, it was offered varying width mirrors located on a parabolic shaped base. However, there was no any given detail for the losses. In the study done by Hongn et al. (2015), end losses are analyzed analytically by using a simple least square fitting and they give an expression to estimate the average annual non-illuminated length and end loss. Chemisana et al. (2013) have tried to design and test a method to assess the optical quality of solar concentrators, based on the absorber reflection method. In the study, very detailed information is given about the errors while the mirrors reflecting the sun rays. Varying width of mirrors are offered to avoid the shading and blocking loss, however no any details about the losses. Liu et al. (2014) have investigated the relations between the structural parameters and the optical performances of the system. In the study, the structural parameters (W, S, Q) of the system are obtained and analyzed. However, instead of giving details about optical parameters, it was focused on the concentrated radiation distribution on the PV device (receiver) by making use of software for tracing sun rays. Sallaberry et al. (2015) have focused on the estimation of long-term optical losses due to the tracking error of a low-temperature collector using low-concentration optics in their study. Balaji et al. (2016) have studied on structural and optical parameters of an LFR system in terms of secondary reflector in the receiver. Although the optical efficiency was calculated, it was not supplied any details about the losses. Tsekouras et al. (2018) have dealt with the optical and thermal investigation of a linear Fresnel collector with trapezoidal cavity receiver.

The optical analysis is performed through the development of a ray-tracing model in their study. Therefore, there was no any detailed information about the losses individually. Bittencourt et al. (2015) have developed a numerical model in order to obtain the optical efficiency of a solar collector with a linear Fresnel concentrator. Their model is built based on the ray-tracing and Monte Carlo methods.

In this study, optical losses in an LFR-PV hybrid system are analyzed with the aid of computer by considering 9 realistic mirror-field configurations. For each of the configuration, the loss because of the mirror shadowing, mirror blocking, receiver shadowing, spillage and longitudinal cosine effect (end loss) are calculated hourly for the representative days of January, April, July and October as the seasonal representative months of a year and presented as the annual average values. Later on, a relationship is built in between the losses and the structure parameters of the LFR system to get a fast understanding about the losses.

2. Precise determination of the optical losses

Besides the inevitable transversal and longitudinal cosine losses, the optical losses in an LFR system (Fig.1) can occur due to the shadowing and blocking of the adjacent mirrors, shadow of the receiver on the mirrors and the edge losses due to the height of the receiver tower.

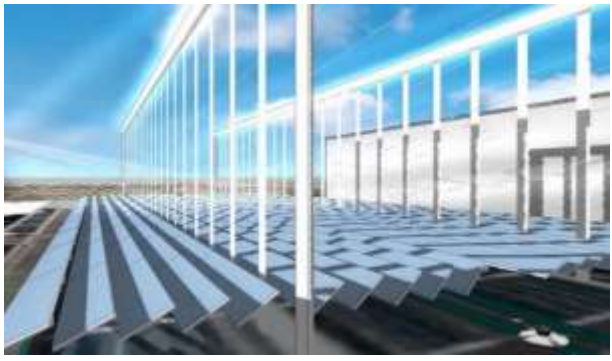

Figure 1 Demonstration of the optical losses in an LFR system.

When the incoming sun rays on a mirror is blocked by an adjacent mirror then a shadow is occurred on the mirror which is called as shadowing loss and when the sun rays reflected by a mirror is blocked by an adjacent mirror then a blocking loss occurs as it is shown in the Fig.2

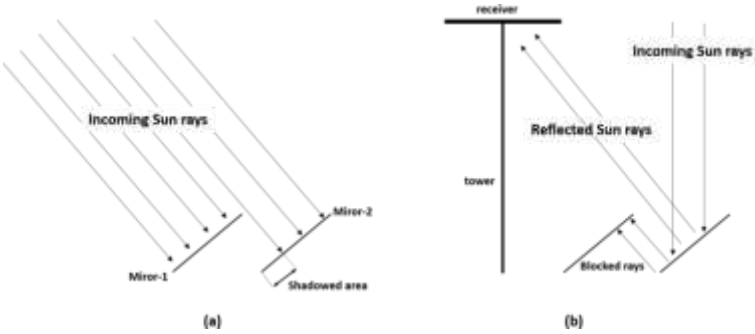

Figure 2 Mirror (a) shadowing (b) blocking loss mechanisms in an LFR system

A classical thermal receiver is replaced by a PV panel in the considered LFR system in this study. Thus, the edge losses are relatively small because of the larger aperture of PV when compared to a thermal receiver. The shadow caused by receiver is seen in Fig.3.

Figure 3 Optical loss due to shadow on the mirrors caused by receiver.

The system is theoretically configured by taking the mirror width (*W*), the gap between mirrors (*S*) and the distance of mirrors to the center of the system (*Q*) as it is shown Fig.4

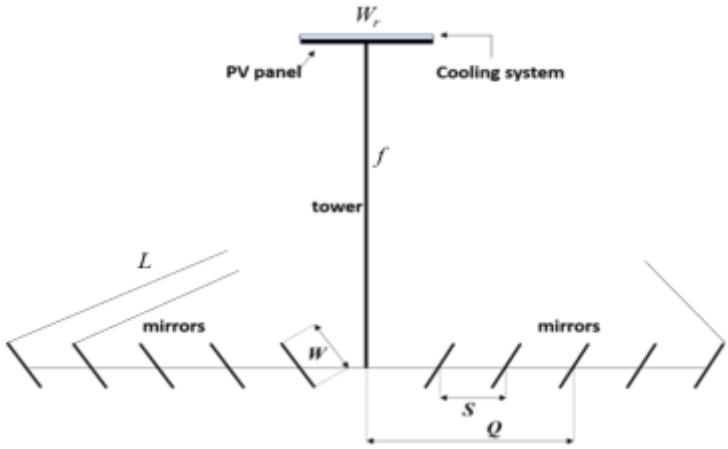

Figure 4 Theoretical configuration of the LFR system

The LFR system is assumed to be located at 41.1051º N and 29.0225º E (Ayazaga Campus of Istanbul Technical University, Turkey). The monthly average hourly global solar radiation is calculated by using the ASHRAE algorithm (Maleki et. al, 2017) for the optical calculations. The months January, April, July and October are selected as the seasonal representatives to make annual calculations. The radiation for every month is averaged by taking the representative day of the month into account (Anis et. al, 2019). To make the calculations, the sun is considered moving on the transversal and the longitudinal plane of the system as showing in the Fig.5

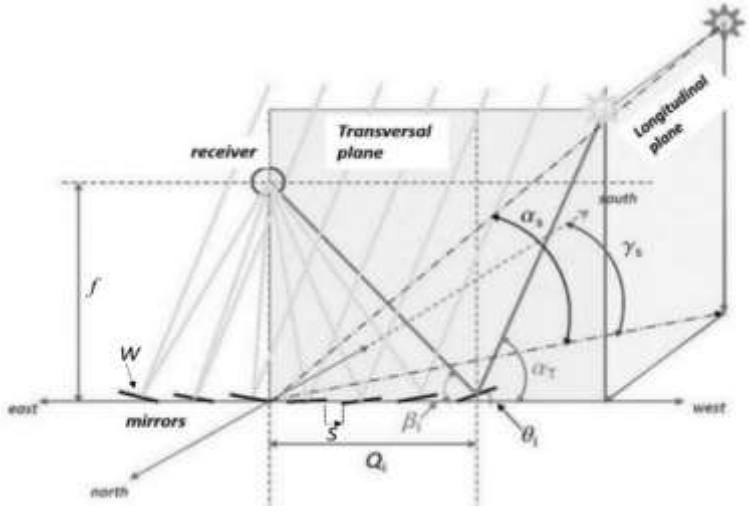

Figure 5 Geometrical parameters on the transversal plane of the system (Çalık and Firat, 2019)

Nine different system configurations are considered as variations for the optical losses. The length of the mirrors is taken as 3 m in all of the variations. These variations are shown in Table 1.

Table 1 LFR System-configuration variations respect to mirror width (*W*), Gap (*S*) and distance (*Q*)

VARIATIONS	1	2	3	4	5	6	7	8	9
Mirror width, *W* (mm)	300	300	300	400	400	400	500	500	500
Gap between mirrors, *S*, (mm)	100	200	300	100	200	300	100	200	300
Mirror to Center distance, *Q*, (mm)	400	500	600	500	600	700	600	700	800

Shadowed areas on each of the mirror are calculated with the help of the computer aided graphics. The hours considered for the calculations are selected according to the value of the radiation at that time of the day. Therefore, the hours with low radiation levels are eliminated and this is why the hours for the shadowing loss calculations are not matched with the sunrise and sunset hours. For the given location, the solar radiation data for the month January is given in the Table 2 as sample. The data for the other months is obtained and calculated in the same way.

Table 2 Solar radiation data for January for the given location.

	Local time	Zenith angle (degree)	Solar Azimuth (degree)	Solar altitude (degree)	Hourly DNI (W/m2)
	09.00	85.1	122.86	4.9	19.71
	10.00	76.4	133.87	13.7	159.03
	11.00	69.1	146.45	20.9	294.33
	12.00	64.1	160.72	25.9	388.34
	13.00	61.8	176.27	28.2	430.01
Solar noon	13.14	61.7	179.99	28.3	431.65
	14.00	62.6	192.11	27.4	415.03
	15.00	66.4	207.08	23.6	345.01
	16.00	72.7	220.47	17.3	227.08
	17.00	80.8	232.2	9.2	80.58
	18.00	89.9	242.56	0.1	0.00

From Table 2, it can be seen that the considerable values of the average hourly direct solar radiation (HDNI) are in between the hours 10:00 and 17:00 for the representative day of the January. Therefore, this interval of hours is considered for the shadowing loss calculations. The average HDNI for January is obtained as 292.43 W for the hours between 10:00 and 17:00. Similarly, when the months April, July and October is considered as

seasonal months, the average HDNI for all variations, the average daily DNI incoming on the mirrors and the average daily radiation after transversal cosine loss for the variation#1 are given in the Table 3.

Table 3 The seasonal average HDNI, the average daily DNI and the average daily irradiation w/transversal cosine loss for the variation#1

Seasonal months	Av. HDNI (W)	Av. daily DNI (W)	Av. daily transversal cosine loss (W)	Av. daily irradiation w/cosine losses (solar power expected to be reflected)
January	292.43	2579.20	228.39	2350.81
April	615.60	5429.56	408.87	5020.69
July	643.18	5672.88	414.61	5258.27
October	449.32	3963.01	323.31	3639.70

All cosine effects are inevitable in fixed and single axis tracking systems unless the system is located at the equator (the latitude φ=0^o), the sun is at the equinoxes and the measurements is made at solar hour angle of 90^o.

The transversal cosine effect depends on the transversal solar incident angle θ_i , which is defined by the angle β_i and the transversal solar altitude angle α_T given in Fig.5 as following;

$$\theta_i = \frac{\alpha_T - \beta_i}{2} \tag{1}$$

The angle β_i is calculated by the distance of the considered mirror center from the system center, Q_i , and the height of the receiver tower, *f*, as below;

$$\beta_i = \tan^{-1}\frac{f}{Q_i} \tag{2}$$

The angle α_T, is calculated by using solar azimuth, γ_s, and solar altitude angle, α_s as given in Eqn. (3);

$$\alpha_T = \begin{cases} \frac{\tan\alpha_s}{\sin\gamma_s}, & if\ \gamma_s \le 180 \\ \frac{\tan\alpha_s}{\sin(\gamma_s - 180)}, & if\ \gamma_s > 180 \end{cases} \tag{3}$$

The transversal cosine loss is defined for one mirror as following;

$$L_{ci} = HDNI.W.(1 - \cos\theta_i) \tag{4}$$

Thus, the total transversal cosine loss in all mirror system is obtained by the following equation;

$$L_c = \sum_{i=1}^{N} L_{ci} = HDNI.W.\sum_{i=1}^{N}(1 - \cos\theta_i) \tag{5}$$

where *N* is the number of the mirrors in the considered system.

The calculations for the shadowing and blocking losses are made as following: First, the sun's position (transversal altitude angle, α_T) is placed on the transversal plane hours by hours in a computer aided design (CAD) program, as it is shown in Fig 6.

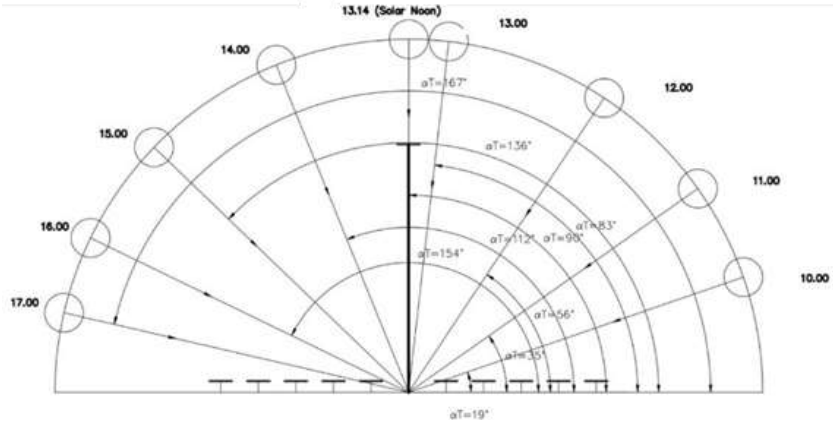

Figure 6 Position (transversal altitude, α_T) of the sun on the transversal plane of the system.

Then, after drawing the incoming and the reflected sun rays, the shadowed and the blocked areas are calculated by measuring the shadowed and blocked width for each of the mirrors for the given time of the representative day of the considered month as it is shown in the Fig.7 as a sample for January at time 10:00 for the variation#1.

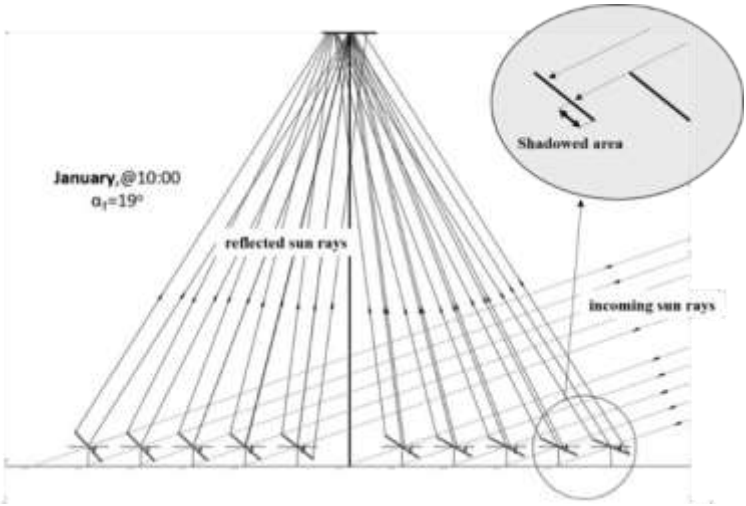

Figure 7 Shadowed areas on the mirrors on January at 10:00 for variation#1

As an example, for the representative day of the month January (17th Jan), there is seen no any blockage however the shadow by the mirror and the amount of shadow on the 4th left mirror caused by an adjacent mirror is measured as 104 mm as it is shown in the Fig.8.

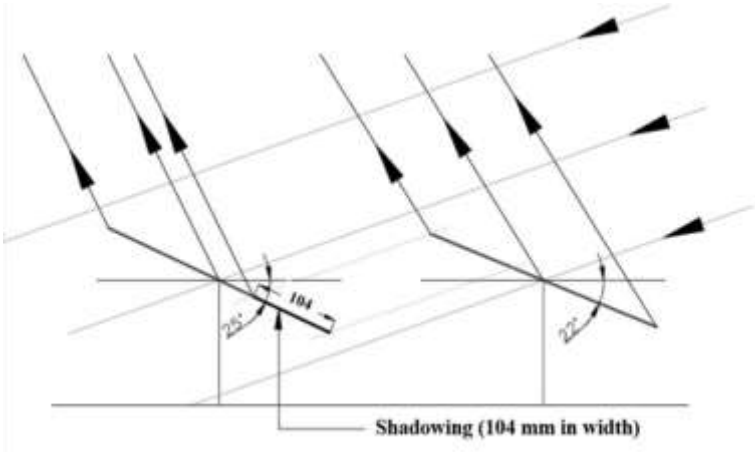

Figure 8 The shadowing width for variation#1 on January at 10:00

Therefore, the shadowed area on 4th mirror is calculated as 0.31m^2 for the mirror length of 3m. Similarly, the measurements and the shadowed and blocked area calculations are made for all of the mirrors for the given system configuration and the results regarding shadowing area are given in Table 4.

Table 4 Shadowed area values for each of the mirrors for the representative day of the month January for variation#1

Local time	10:00	11:00	12:00	13:00	14:00	15:00	16:00	17:00
Shading	(m^2)	(m^2)	(m^2)	(m^2)	(m^2)	(m^2)	(m^2)	(m^2)
Mirror no			NO SHADING					
1	0.38	0.09				0.00	0.00	0.20
2	0.37	0.066				0.021	0.30	0.56
3	0.34	0.033				0.033	0.32	0.58
4	0.31	0.00				0.042	0.33	0.59
5	0.00	0.00				0.048	0.34	0.59
Center								
-1	0.00	0.00				0.00	0.25	0.53
-2	0.44	0.147				0.00	0.23	0.51
-3	0.44	0.159				0.00	0.20	0.49

-4	0.46	0.171		0.00	0.17	0.47
-5	0.47	0.18		0.00	0.00	0.00

As it is seen from Table 4, there is no any shadowing loss at some certain hours and for some certain mirrors on the given day. The equivalent shaded power on each of the mirrors on the representation day of January for the variation#1 is presented in Table 5 by considering the hourly DNI values given in Table 2.

Table 5 The lost power due to shadowing for January for variation#1

Local time	10.00	11.00	15.00	16.00	17.00
Mirror No	Lost Solar Power due to Shading (W)				
1	59.38	25.96	0.00	0.00	15.64
2	57.04	19.04	7.10	66.76	44.30
3	52.83	9.52	11.16	70.77	45.48
4	48.62	0.00	14.20	72.77	46.91
5	0.00	0.00	16.23	75.44	46.67
Center					
-1	0.00	0.00	0.00	54.75	41.46
-2	67.79	42.40	0.00	50.07	40.04
-3	67.79	45.86	0.00	45.40	38.85
-4	71.07	49.32	0.00	37.39	37.19
-5	72.94	51.92	0.00	0.00	0.00

In the case of considering the shadowing loss, the total reflected net solar power coming on the receiver will be obviously lesser than the solar power expected to be reflected if there was no shadowing loss as it is given in Table 6 for January for variation #1.

Table 6 Reflected net total solar power from mirrors after the shadowing loss for the representative day of January for variation#1

Local time	Solar Power expected to be reflected (W)	Power lost due to mirror shading (W)	The expected to be reflected net power after shadowing loss (W)
10:00	1119.62	497.47	622.15
11:00	2259.12	244.02	2015.10
12:00	3217.50	-	3217.50
13:00	3720.79	-	3720.79
14:00	3531.20	-	3531.20
15:00	2750.91	48.69	2702.22

16:00	1666.18	473.35	1192.83
17:00	541.13	356.53	184.60
Average	2350.81	202.51	2148.30

The expected to be reflected solar power values given in Table 3 are calculated as the product of the hourly DNI given in Table 2 and the projective surface area of the tilted mirror (transversal cosine effect) whose surface is covered with an aluminum lightning sheet with a very high reflectance rate of 0.98 (ANOLUX, 2021). Similar calculations are repeated for the representative days of April, July and October to obtain the annual averaged values for the given LFR system variations as the expected to be reflected power after mirror shadowing loss. As an example, the monthly average-hourly solar radiation results for all of the months for variation#1 are given in Table 7.

Table 7 The monthly average-hourly solar radiation values for variation#1

Months	Reflected power (with cosine loss), (W)	Power loss due to mirror shadowing, (W)	Net power to be reflected, (W)
January	2350.81	202.51	2148.30
April	5020.69	280.07	4740.62
July	5258.27	289.26	4969.01
October	3639.70	248.02	3391.68
Average	4067.37	254.97	3812.40

It can be seen that the annual average-hourly shadowing loss in an LFR system for the variation#1 is calculated as about 254.97 W. When the measurements and the calculations are repeated for the other variations, the results obtained for annual average shadowing loss, expected-reflected power, net reflected power after shadowing loss and the total area of the LFR system for given configuration are presented in the Table 8.

Table 8 System and the yearly average hourly solar radiation values for all variations

Var.s	Width (mm)	Gap (mm)	Dist. (mm)	Mirrors area (m^2)	System Area (m^2)	Power with transversal cosine loss (W)	Shadowing loss (W)	Reflected Power after shadowing loss (W)
1	300	100	400	9	12.9	4067.37	254.97	3812.40
2	300	200	500	9	15.9	3749.17	116.00	3633.17
3	300	300	600	9	18.9	4001.23	59.73	3941.5
4	400	100	500	12	16.2	5380.33	417.94	4962.39
5	400	200	600	12	19.2	5334.97	217.84	5117.13
6	400	300	700	12	22.2	5288.79	127.52	5161.27

7	500	100	600	15	19.5	6668.71	508.01	6160.70
8	500	200	700	15	22.5	6610.99	277.35	6333.64
9	500	300	800	15	25.5	6553.71	209.39	6344.32

There is no any blocking loss seen in all of the variations. This is because of the enough gaps between the adjoint mirrors.

Another optic loss which is called as receiver shadowing loss happens due to the receiver shadow on the mirrors. In Fig.9, how the receiver-shadow occurs on the mirrors is shown for the month January at time 13:00 as an example.

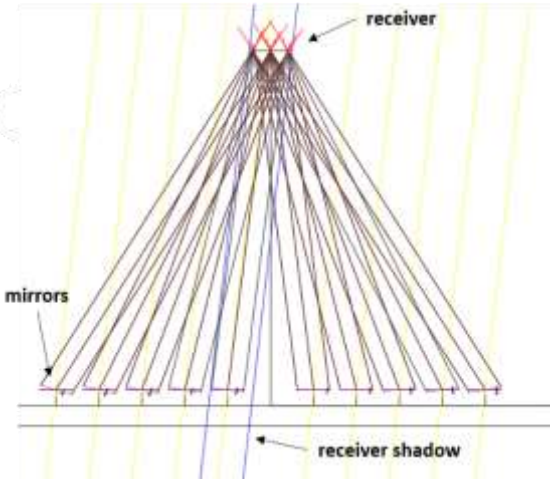

Figure 9 The receiver shadow on the mirrors for the variation #1 on January at time 13:00.

The amount of the shadowed mirror-area by receiver is given in Table 9 for January at time 13:00.

Table 9 Shadowed area values for each of the mirrors for the month January at time 13:00 for variation#1

Local	10:0	11:0	12:0	13:0	14:0	15:0	16:0	17:0
	Shadowed area (m^2)							
Mirro								
1								
2								
3					0.79			
4					0.10			
5								

-1				0.90				
-2								
-3								
-4								
-5			0.71					

The amount of the loss in terms of power is shown in Table 10.

Table 10 The lost power due to receiver shadowing for January at time 13:00 for variation#1

Local time	12:00	13.00	14.00
Mirror No	Lost Power due to Receiver-Shading (W)		
1			
2			
3			324.57
4			42.71
5			
Center			
-1		379.27	
-2			
-3			
-4			
-5	272.87		
Total	272.87	379.27	367.28

The longitudinal cosine loss (or the end loss) causes some receiver area as not illuminated and it is calculated by the longitudinal solar incident angle which is given with the following equation,

$$\theta_L = Arctan(\cos\gamma_s \tan\theta) \tag{6}$$

where θ is the solar incident angle which is defined as below;

$$\cos\theta = \sin\delta \sin\varphi + \cos\delta \cos\varphi \cos\omega \tag{7}$$

φ is the latitude of the system location and the solar declination angle and the solar hour angle are defined as the following respectively,

$$\delta = 23.45 \sin\left[\frac{360}{365}(d + 284)\right] \tag{8}$$

$$\omega = 15^o(t - 12) \tag{9}$$

d is the day number of the year and *t* is the local solar hour. The longitudinal cosine loss is calculated by the Eqn. (10) and the effect is sketched up in the Fig. 10.

$$L_{cL} = HDNI.L.W.(1-\cos\theta_L)(1-\cos\theta_i) \quad (10)$$

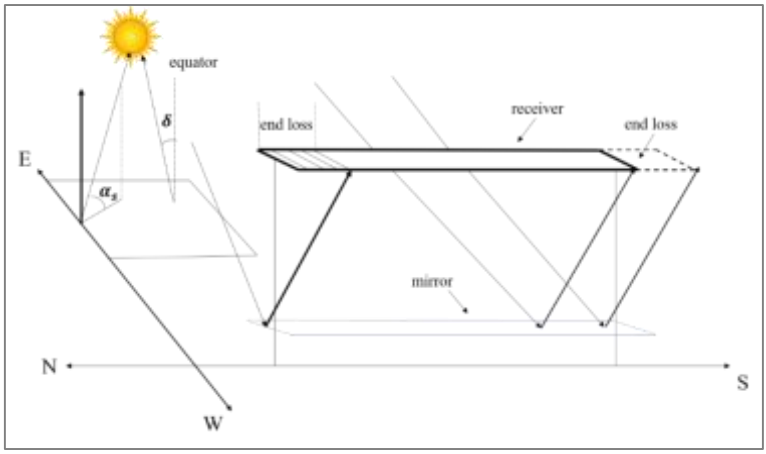

Figure 10 The sketch of the longitudinal cosine effect.

It is clear that through the equations (1) to (10), the transversal and the longitudinal cosine losses include all information about the sun's position in the sky, the solar radiation in the location and the mirror's geometry regarding to the sun's position.

As an example, the hourly end loss (longitudinal cosine loss) for the representative day of January (*d*=17) for the variation#1 is presented in the Table 11.

Table 11 The hourly end loss for the representative day of January (*d*=17) for the variation#1

Local time	ω (deg.)	δ (deg.)	γ_s (deg.)	θ_L (deg.)	Lost area (m^2)	HDNI (W)	Long. cosine loss (W)
10:00	131.49	-20.68	133.87	35.32	0.15	159.03	23.71
11:00	146.49	-20.67	146.45	30.20	0.11	294.33	32.35
12:00	161.49	-20.67	160.72	24.49	0.07	388.34	28.30
13:00	176.49	-20.66	176.27	20.62	0.05	430.01	22.32
14:00	191.49	-20.65	192.11	22.20	0.06	415.03	24.93
15:00	206.49	-20.64	207.08	27.55	0.09	345.01	31.68

16:00	221.49	-20.63	220.47	33.06	0.13	227.08	29.77
17:00	236.49	-20.62	232.20	37.73	0.17	80.58	13.65

Table 11 shows that the average hourly longitudinal cosine loss (end loss) in January for the variation#1 is just 25.84 W.

Some of the reflected sun rays towards the receiver is not collected by the receiver and they escape back in to the space (ray-spillage), this causes an optical loss which is called as edge loss. No edge losses are observed in variation#1. However, this loss is observed in other variations and is included in the calculations. In Fig. 11, the edge loss is shown for January at time 12:00 for the variation#8 as an example.

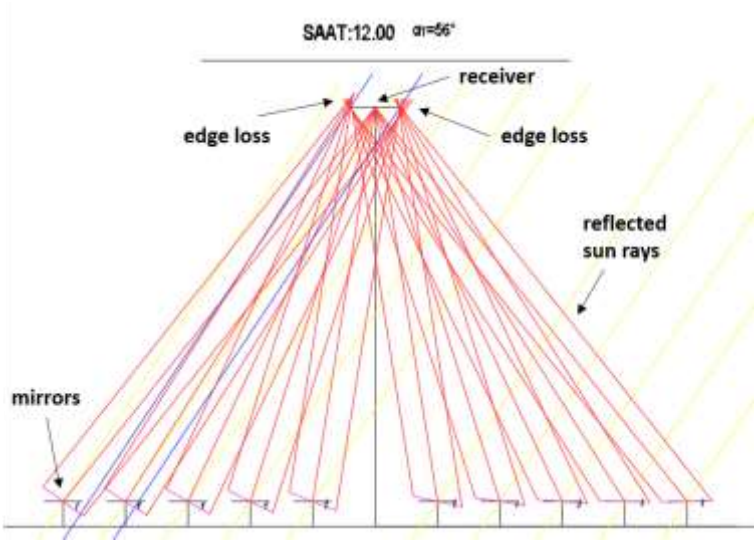

Figure 11 The end losses for the variation #8 on January at time 12:00.

The amount of the edge loss for the variation#8 is given in Table 12 in terms of the lost area and the lost solar power for January for the hours 10:00 to 17:00. The lost power is calculated by multiplying the reflected solar irradiation (W/m^2) and the lost area related to ray-spillage.

Table 12 The amount of the edge loss for the representative day of January for variation#8

Local time	The length of lost area (m)	Lost edge area, (m^2)	Power lost due to spillage, (W)
10:00	0.182	0.55	85.09
11:00	0.226	0.68	195.56
12:00	0.344	1.03	392.75

13:00	0.318	0.95	402.03
14:00	0.339	1.02	413.64
15:00	0.344	1.03	348.93
16:00	0.197	0.59	131.52
17:00	0.170	0.51	40.27

All of the optical losses occur on the representative day of July for the variation#8 is given in Table 13 as an example.

Table 13 The optical losses occur on the representative day of July for the variation#8

Local time	Power with transversal cos. loss (W)	Mirror shading loss (W)	Receiver shading loss (W)	Edge loss (W)	End loss (W)	Net power on the receiver (W)
07:00	1418.15	602.23		58.40	60.09	697.42
08:00	3916.92	830.29		184.07	238.12	2664.43
09:00	6682.08			350.28	9.37	6322.44
10:00	9370.21			556.74	242.44	8571.03
11:00	11674.54		692.90	867.38	434.16	9680.09
12:00	13294.03		594.77	925.82	635.59	11137.84
13:00	13988.57			890.48	768.06	12330.03
14:00	13639.41		1119.26	933.19	696.89	10890.07
15:00	12305.30		699.15	751.91	503.55	10350.70
16:00	10199.49		692.64	783.18	309.63	8414.03
17:00	7602.45			416.51	104.65	7081.29
18:00	4825.47	827.67		235.30	405.46	3357.04
19:00	2189.78	937.31		96.65	98.60	1057.22

Direct normal irradiation (DNI), incoming power including transversal cosine loss (P_c), average annual (as the average of the seasonal representative months of January, April, July and October) optical losses (the transversal cosine loss, L_c, the mirror shadowing loss, L_m, the receiver shadowing loss, L_r, the edge loss, L_e, and the longitudinal cosine loss (end loss), L_{cL}) and the total optical efficiency, η_{op} , calculated according to Eq.11 are given in Table 14 for all variations.

The total optical efficiency can be calculated as following;

$$\eta_{op} = 1 - \frac{L_m + L_r + L_e + L_{cL}}{P_c} \quad (11)$$

Table 14 Average annual optical losses and total optical efficiency of the system

Variations	DNI	P_c, (W)	L_c, (W)	L_m, (W)	L_r, (W)	L_e , (W)	L_{cL}, (W)	η_{op}, (%)
1	4411.25	4067.36	344	254.97	198	0	92.92	86.58
2	4411.25	4035.25	376	116.00	182	0	101.65	90.10
3	4411.25	4001.23	410	59.73	130	0	109.75	92.52
4	5881.55	5380.33	501	417.94	228	115	134.92	83.34
5	5881.55	5334.97	547	217.84	177	181	147.07	86.45
6	5881.55	5288.79	593	127.52	145	249	159.22	87.12
7	7351.94	6668.71	683	508.01	236	344	183.99	80.93
8	7351.94	6610.99	741	277.35	209	433	200.19	83.06
9	7351.94	6553.71	798	209.39	227	532	216.15	81.93

Hence, it can be built a relationship between the mirror shadowing loss (L_m), the receiver shadowing loss (L_r), the edge loss (L_e), optical efficiency (η_{op}) and the structure parameters width (W) and gap (S) as well as transversal (L_c) and longitudinal cosine losses (L_{cL}) by using a multiple regression (MR) analysis (Darlington and Hayes, 2017). This relation might satisfy very useful information about the optical losses and the structure parameters before constructing an LFR system. Hence, by using an MR, these relations are obtained as follows respectively:

$$L_m = -212.89 + 32.26W - 7.54S + 3.01L_c - 15.74L_{cL} \quad (12)$$

$$L_r = -39.08 + 16.77W + 1.39S - 13.04L_c + 45.24L_{cL} \quad (13)$$

$$L_e = 353.26 - 56.49W - 14.40S + 8.60L_c - 15.87L_{cL} \quad (14)$$

$$\eta_{op} = 76.52 + 1.09W + 0.55S - 0.20L_c + 0.42L_{cL} \quad (15)$$

As an example, the shadowing loss presented in Table 14 and the values obtained by Eq. (12) are given in the Fig.12. It can be seen a good match between the values. Therefore, one can calculate all of the optical losses

by offering different W, S, L_c and L_{cL} values before constructing an LFR system.

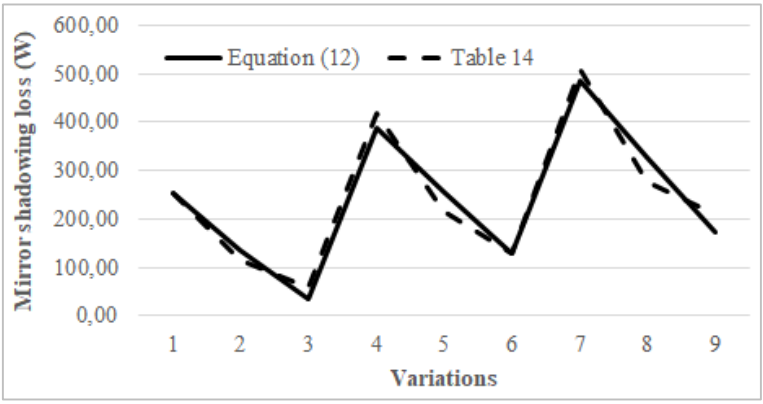

Figure 12 Comparison of shadowing loss values presented in Table 14 and Eqn. (12).

3. Conclusion

In this paper, a comprehensive optical loss mechanism is analyzed with the aid of CAD by considering 9 realistic mirror configurations. For each of the configuration, besides determining the transversal and longitudinal cosine losses, the optical loss due to mirror shadowing and blocking of the adjacent mirrors, the loss due to receiver shading on the mirrors and the edge loss on the receiver are calculated hourly for the representative days of January, April, July and October as the seasonal representative months of a year. After tabulating the results, one can make an eye-checking decision on the configuration by considering the parameters whichever they want. For example, if one decides that the amount of shadowing loss is more important, then, they can select the variation in where the shadowing loss is the least without minding the cost of the mirrors or system size.

Later on, relationships are established in between the optical losses and the structure parameters of the LFR system by regression analysis. Thus, one can have a very strong idea about the amount of the optical losses when the structure parameters change.

Once a relationship is obtained between the optical losses and the structural parameters, the regarding optical loss can be optimized by introducing some restrictions on the parameters. This kind of optimization can be made on other parameters as well. For example, one might want the system size minimum but the shadowing loss minimum too. Thus, by

introducing a restriction on shadowing loss, the system size might be maximized.

References

Anis MD.S., Jamil B., Ansari MD.A., Bellos E. (2019). "Generalized models for estimation of global solar radiation based on sunshine duration and detailed comparison with the existing: A case study for India", Sust. Energy Tech. and Asses., 31, 179–198.

ANOLUX Miro Silver, http://anomet.com/reflective-aluminum, (accessed 01/04/2021).

Balaji S., Reddy K.S., Sundararajan T. (2016). "Optical modelling and performance analysis of a solar LFR receiver system with parabolic and involute secondary reflectors", Applied Energy, 179, 1138–1151.

Beltagy H., Semmar D., Lehaut C., Said N. (2017). "Theoretical and experimental performance analysis of a Fresnel type solar concentrator", Ren. Energy, 101, 782-793.

Bittencourt A., Pigozzo V.C., Passos J.C., Cascaes G.M., Burigo A. (2015). "Geometrical Parametric Analysis to Find Optimum Configuration of a Solar Concentrator Workbench Using Linear Fresnel Technology", ISES Solar World Congress, Daegu, Korea, 08-12 November 2015, DOI:10.18086/swc.2015.10.06.

Calik K., Firat C., (2019). "A Cost-Effective Theoretical Novel Configuration of Concentrated Photovoltaic System with Linear Fresnel Reflectors", J. of Polytechnic, 22:3, 583-589.

Chemisana D., Barrau J., Rosell J.I., Abdel-Mesih B., Souliotis M., Badia F. (2013). "Optical performance of solar reflective concentrators: A simple method for optical assessment", Renewable Energy, 57, 120-129.

Darlington R.B., Hayes A.F., (2017). Regression Analysis and Linear Models: Concepts, Applications, and Implementation, The Guilford Press, New York, USA.

Gordon J. M., Ries H. (1993). "Tailored edge-ray concentrators as ideal second stages for Fresnel reflectors", Applied Optics, 32:13, 2243-2251.

Gouthamraj K., Jamuna Rani K., Satyanarayana G. (2013). “Design and Analysis of Rooftop Linear Fresnel Reflector Solar Concentrator”, Int. J. of Eng. and Innovative Tech., 2:11, 2013, 66-69.

Hongn M., Flores Larsen S., Gea M., Altamirano M. (2015). “Least square based method for the estimation of the optical end loss of linear Fresnel concentrators”, Solar Energy, 111, 264–276.

Liu Y., Hu P., Zhang Q., Chen Z. (2014). “Thermodynamic and optical analysis for a CPV/T hybrid system with beam splitter and fully tracked linear Fresnel reflector concentrator utilizing sloped panels”, Solar Energy, 103, 191– 199.

Maleki S.A.M., Hizam H., Gomes C. (2017). “Estimation of Hourly, Daily and Monthly Global Solar Radiation on Inclined Surfaces: Models Revisited”, Energies, 10, 134.

Mathur S.S., Kandpal T.C., Negi B. S. (1991a). “Optical design and concentration characteristics of linear Fresnel reflector solar concentrators-I. Mirror elements of varying width”, Energy Conversion and Management, 31:3, 205-219.

Mathur S.S., Kandpal T.C., Negi B. S. (1991b). “Optical design and concentration characteristics of linear Fresnel reflector solar concentrators-II. Mirror elements of equal width”, Energy Conversion and Management, 31:3, 221-232.

Sallaberry F., García De Jalón A., Torres J., Pujol-Nadal R. (2015). “Optical losses due to tracking error estimation for a low concentrating solar collector”, Energy Conv. and Management, 92, 194–206.

Tsekouras P., Tzivanidis C., Antonopoulos K. (2018). “Optical and thermal investigation of a linear Fresnel collector with trapezoidal cavity receiver”, App. Thermal Eng., 135, 379–388.

Zhu J., Huang H. (2014). “Design and thermal performances of Semi-Parabolic Linear Fresnel Reflector solar concentration collector”, Energy Conv. and Management, 77, 733–737.

CHAPTER VIII

AROMATIC COMPOUNDS OF PROTEOLYSIS AND LIPOLYSIS ORIGIN OCCURRING DURING FERMENTATION IN MEAT PRODUCTS

Özgür KARADAŞ

(PhD Student); Tekirdağ Namık Kemal University, Tekirdağ, Turkey
e-mail: ozgurkaradas1@gmail.com, Orcid ID: 0000-0002-7379-7845

Binnur KAPTAN

(Asst. Prof. Dr.); Tekirdağ Namık Kemal University, Tekirdağ, Turkey
e-mail: bkaptan@nku.edu.tr, Orcid ID: 0000-0002-6268-7245

İsmail YILMAZ

(Prof. Dr.); Tekirdağ Namık Kemal University, Tekirdağ, Turkey
e-mail: iyilmaz@nku.edu.tr, Orcid ID: 0000-0003-1116-0934

1. Introduction

Meat, which has been important in terms of our diet from the ancient times till present day, is the source of minerals, vitamins, proteins and different bioactive compounds (conjugated linoleic acid, peptides, taurine, creatine, etc.). Various methods such as smoking, salting, drying, cooking, sterilization, cooling and freezing have been used in order to preserve the meat for a long time, and thus, meat products have emerged. Today, meat products are produced in many countries by applying traditional or modern technological processes, depending on the differences in preservation methods and eating habits. Meat products have a longer shelf life as they contain less water, more protein, spices and various additives compared to fresh meat due to their production technology. Therefore, meat products are preferred more compared to fresh meat (Öziş, 2014; Öztan, 1999; Ulusoy, 2007).

Fermentation is also an old method used to prevent food spoilage, and is widely used in the meat industry as a preservation method and to benefit from the specific taste and aroma of meat (Ulusoy, 2007; Yılmaz and Velioğlu, 2009). While fermentation is carried out naturally with the effect of bacteria on meat in small production enterprises, it is carried out in a controlled manner by using starter cultures in industrial enterprises. Meat products produced through natural fermentation have superior properties compared to meat products produced through controlled fermentation. This superiority depends on the quality of the raw meat used, the specific nature

of the natural flora, and the characteristics of the technology used. However, in meat products produced by natural fermentation, taste, aroma, structure and other features are not always similar, so it is not possible to reproduce meat products with the same characteristics (Başyiğit et al., 2007; Macedo et al., 2017).

Fermented meat products constitute an important part of our diet, and when it comes to fermented meat products in our country, sausage comes to mind first due to its familiar properties related to its texture, flavor and color. Fermented sausage is a meat product obtained by mixing the ground raw meat and fat with salt, spices and additives and filling them into the intestines, and leaving to maturing and drying at a certain temperature and humidity. Sausage specific to our country is a product that has an important share in the market and is popularly consumed (Laslo et al., 2019; Şanes, 2006).

The aroma of the meat and the appearance of the food on the plate affect acceptability by the consumers. In fermented meat products, texture (softness, juiciness, fiber, oiliness, etc.), aroma and taste are the main factors affecting the sensory quality of the product (Resconi et al., 2013). Fermentation of meat produces a series of physical, biochemical and microbial changes in the muscle-based product caused by endogenous and microbial enzymatic activities. Among these changes are acidification (carbohydrate catabolism), increased solubility and gelation of myofibrillar and sarcoplasmic proteins, degradation of proteins and lipids, reduction of nitrate to nitrite, nitrosomioglobin formation, and dehydration (Ojha et al., 2015). However, the main biochemical reactions in the formation of flavor or flavor precursors are due to proteolysis and lipolysis caused by both microbial and endogenous enzymes (Martín-Sánchez et al., 2011).

Proteolysis is an extremely important biochemical change in fermented meat products such as sausage, wiener and ham. It affects both the texture and aroma of meat due to the formation of many low molecular weight compounds, including peptides, amino acids, aldehydes, organic acids and amines (Wang et al., 2017). Lipolysis is one of the main processes of breaking down lipids in fresh meat during processing and is governed by a number of specific enzymes, namely lipases and phospholipases, leading to the formation of free fatty acids. Endogenous enzymes of fat cells, muscle fibers and bacterial enzymes play a role in lipolysis (Gandemer, 2002). Lipolysis is especially necessary for the development of fermented dry sausage flavor. Lipids are affected by lipolytic and oxidative reactions, causing the release of fatty acids, carbonyl compounds and other low

molecular weight substances important for flavor (Martín-Sánchez et al., 2011).

Aldehydes, ketones, terpenes, aromatic hydrocarbons, acids, alcohols, esters, sulfur and nitrogen containing compounds are commonly found in fermented meat products as aromatic compounds. The purpose of this review is to examine in detail the effects of proteolysis and lipolysis reactions on aroma compounds and flavor in fermented meat products.

2. Formation of Aroma Compounds in Fermented Meat Products

The characteristic flavor and aroma of fermented meat products can be formed as a result of the breakdown of proteins and lipids by microbial and enzymes (Macedo et al., 2017).

2.1 Proteolysis

Proteolysis is one of the important biochemical reactions that occur during the production of fermented meat products, and it is the breakdown of proteins into polypeptides, peptides and amino acids, respectively, by means of muscle enzymes and enzymes such as microbial protease. The main importance of proteolysis, which is also defined as protein degradation briefly, is that free amino acids create different components such as amine, ketone and organic acid, which have a smaller molecular weight, through various chemical transformations such as decarboxylation, deamination and transamination. While these components affect the sensory properties of foods, they sometimes add undesirable properties to food (Ercoşkun and Ertaş, 2003; Gökalp et al., 1998; Şanes, 2006; Yetim, 2013). The main stages of proteolysis observed in meat and meat products are shown in Figure 1 (Toldra, 1998).

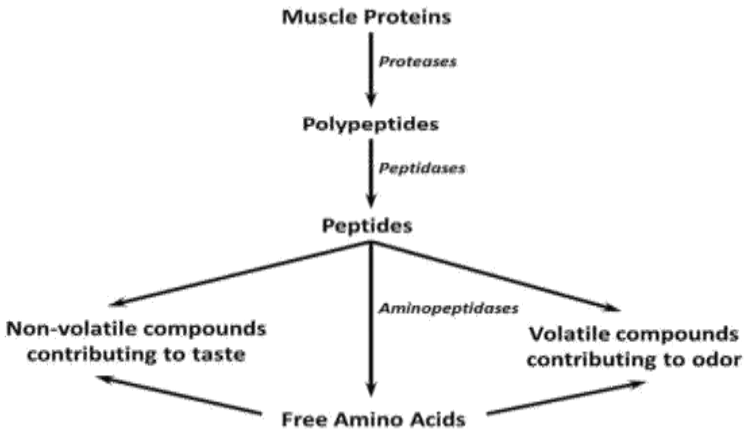

Fig. 1 The main stages of proteolysis observed in meat and meat products

The formation of flavor and aroma in fermented meat products is significantly affected by proteolytic breakdown. Proteolysis during fermentation and maturation causes an increase in non-protein nitrogen compounds. Optimum conditions are provided for fermented meat products for the activity of proteolytic enzymes. While the muscle's own proteolytic enzymes cause the destruction of actin and myosin in the initial stages of fermentation, proteases belonging to bacteria show activity during drying. With the use of proteolytic enzymes in fermented meat products, the proteolysis process accelerates, and the maturing period required for flavor formation is shortened, thus reducing the storage costs of the products. In addition, by using proteolytic enzymes, the continuity of sensory quality in fermented meat products is ensured. However, excessive proteolysis can cause a bitter and metallic taste by spoiling the taste in fermented meat products such as sausage and similar fermented meat products (Serdaroğlu and Tömek, 1995; Şanes, 2006).

2.2 Lipolysis

Lipolysis is the event of the formation of di- and monoglycerides and free fatty acids as a result of the hydrolysis of lipids, which are the main component of fermented meat products, with microbial lipase enzymes and endogenous enzymes. The free fatty acids formed by the hydrolysis of triglycerides are unsaturated and are the precursors of autooxidation reactions that affect the final product aroma, and as a result of these reactions, free fatty acids turn into hydroperoxides and carbonyl compounds. Volatile compounds with aroma properties are also formed as a result of the oxidation of fatty acids and microbial catabolism. (Ercoşkun and Ertaş, 2003; Flores et al., 2006; Şanes, 2006; Toldrá et al., 2001; Yetim, 2013). The main stages of lipolysis observed in meat and meat products are shown in Figure 2 (Toldra, 1998).

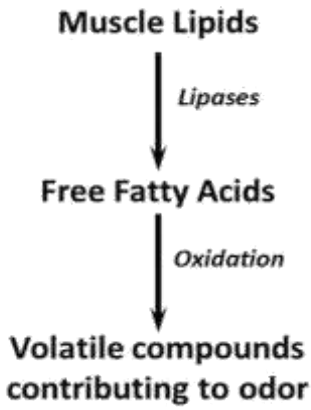

Fig. 2 The main stages of lipolysis observed in meat and meat products

Lipids have a very important effect on the quality of fermented meat products. A large part of the sensory properties in meat products result from the properties of the lipids they contain and the lipolytic and oxidative degradation events that occur during processing in these lipids. Lipid reactions in fermented meat products depend on the source of the meat, especially the breed and diet of the animal. In addition, other raw materials, starter cultures, additives and processing conditions used in the production process also affect the lipid reactions occurring in the product. During production, lipids are subjected to hydrolysis by meat lipases, which remain active during processing, and free fatty acids released as a result of lipid hydrolysis are oxidized, positively affecting the sensory properties of the meat product. However, as a result of lipolysis, flavor degradation and rancidity as well as toxic, carcinogenic, mutagenic, aging-accelerating and immune system impairing components can also occur in fermented meat products, and such a meat product becomes unacceptable as a food item for human consumption. Therefore, it is necessary to keep lipid reactions at a certain level in order to obtain optimum quality in fermented meat products (Ercoşkun et al., 2004; Zanardi et al., 2004).

3. Aroma Compounds in Fermented Meat Products

Products of lipolysis and proteolysis breakdown, namely peptides, amino acids, carbonyls and volatile flavor compounds, contribute to the characteristic flavor and texture of fermented meats (Casaburi et al., 2008). The chemical structures of volatile flavor compounds vary widely, including aldehydes, ketones, terpenes, aromatic hydrocarbons, acids, alcohols, esters, nitrogen and sulfur-containing compounds. Aromatic compounds also vary due to the diversity in these chemical structures (Van Ba et al., 2012). A number of studies have been carried out on various fermented meat products in order to examine aroma compounds. Volatile compounds have been identified as a result of the analyses performed by these studies.

In a study performed by Gök (2006), some quality characteristics of sausage were examined. In sausage samples, 47 volatile aromatic compounds were found in the fermentation stage, while 54 volatile compounds were found in the storage phase. The main ones of these compounds are aldehydes, ketones, esters, alcohols, acids, sulfur compounds and terpenes, and among these compounds, terpenes were the most detected ones.

In a study by Rotsatchakul et al. (2009), a total of 113 volatile compounds were identified in the Nham samples. These included 9 hydrocarbons, 12 aldehydes, 9 ketones, 19 alcohols, 25 esters, 29 sulphur compounds, 2 acids, 1 terpene, 1 furan, 2 halogens, and 4 miscellaneous

compounds. The most prominent aroma compounds in Nham are ethyl butanoate (buttery, ripe fruit note) and sulphur-containing compounds from garlic. Ethyl butanoate had the greatest influence on Nham aroma and was associated with the fermented aroma attribute. Ethyl 2-methyl butanoate (fruity), ethyl 2-methyl propanoate (fruity), 3-hydroxy-2-butanone (yoghurt-like), octanal (fatty-fruity), and hexanal (green) also contributed to the aroma of Nham.

In the study conducted by Kaban (2010) on sausage samples supplied from 5 different companies, a total of 92 volatile compounds, including 5 acids, 7 esters, 10 aliphatic hydrocarbons, 7 alcohols, 5 aldehydes, 11 sulfur compounds, 2 ketones, 7 aromatic hydrocarbons, 27 terpenes, 2 nitrogen compounds, 3 phenols and 6 compounds of butyrylcholine, were identified. It was determined that terpenes (56.11% - 76.32%) were the most common compounds in the products of 4 companies out of the 5 companies, while acids (31.59%) were the most common compounds in one company's products. Other important compounds were acids (especially acetic acid), sulfur compounds (diallyl, disulfide, 1-propene, 3-thiobis, disulfide methyl 2-phenyl) and aldehydes (p-cumic aldehyde). Significant differences were identified between brands, and these differences in the volatile profiles of sausage samples can be explained by the differences in raw materials, spices, other ingredients and production conditions.

Kaban and Kaya (2011) identified volatile compounds of pastrami produced with traditional technology. As a result of this study, 10 aldehydes, 13 aliphatic hydrocarbons, 9 sulfur compounds, 6 esters, 10 alcohols, 4 ketones, 4 aromatic hydrocarbons, 2 acids and 4 terpenes were identified as volatile compounds in pastrami. The volatile compounds of pastrami were mainly formed due to lipid oxidation. In general, aldehydes (17.21% - 43.80%) were found to be predominant in pastrami, and hexanal was determined as the main compound among them.

In their study, Olivares et al. (2011) investigated the effect of fat content and maturing time on sensory properties, lipolysis, lipid oxidation and production of volatile compounds in dry fermented sausages with different fat content (10%, 20% and 30%). High fat sausages showed the highest lipolysis and lipid oxidation determined by free fatty acid content, respectively, and a total of 95 volatile compounds were identified. When the oil ratio decreased, the formation of lipid-derived volatile compounds during processing also decreased, while the formation of volatile compounds produced from bacterial metabolism increased, although it was in the early stages of processing. In addition, for the aroma and overall quality of high and medium fat dry sausages associated with hexanal, 2-

nonenal, 2,4-nonadienal, ethyl butanoate and 1-octen-3-ol flavored compounds, they reported a consumer preference in which a green herbal, oily, fruity and mushy aroma was perceived.

Corral et al. (2013) examined the effect of salt reduction on dry sausage aroma and pointed to a decrease in aroma acceptance that could not be corrected by the addition of KCl. Aroma is affected by an increase in aldehyde compounds and a decrease in sulfur and acids. In short, the flavor of fermented meats varies depending on the processing parameters and raw materials used during production.

Liu et al. (2014) identified a total of 81 aroma-active compounds were identified in Jinhua ham. These include acids (e.g., acetic acid, butanoic acid, and 3-methylbutanoic acid), saturated aldehydes (e.g., hexanal, heptanal, octanal, and 3-methylbutanal), benzene derivatives (e.g., benzeneacetic acid), esters, and lactones (e.g., γ-nonalactone and γ-decalactone) were identified as critical compounds in Jinhua ham aroma. The results also indicated that the type and content of the odorants increased significantly with the duration of the fermentation period.

In a study conducted by Ünal et al. (2017), the aroma and other quality properties of Turkish dry fermented sausage were investigated. The samples were stored for a period of 2, 4 and 6 months. The physicochemical, microbiological, aromatic and sensory properties of the sausage were checked after each storage period. In sausage samples, a total of 60 aroma compounds were identified, including 6 aldehydes (hexanal, octanal, nonanal, hexadecanal, benzaldehyde and ethyl benzaldehyde), 9 acids, 5 alcohols, 4 esters, 3 volatile phenols, two sulfur compounds, and 31 terpenes. The amounts of these compounds were found between 9964.46 and 45135.3 μg / kg. Regarding the effect of the storage period, after the 4th month, total aroma compounds in sausage samples decreased.

In a study conducted by Wang et al. (2017), proteolytic changes in Suanyu, a fermented fish product of China, were determined during a 6-week fermentation period. The findings showed that due to intense proteolysis in Suanyu, a large number of small peptides and free amino acids were formed, and these contributed to Suanyu's flavor and aroma.

Around 100 aroma compounds have been described in fermented sausages, including different chemical classes (aldehydes, ketones, terpenes, aromatic hydrocarbons, acids, alcohols, esters, sulfur and nitrogen compounds). Consequently, the differences between fermented meats in terms of aromatic compounds are due to variations in the abundance of volatile compounds. That is, differences in fermented meat result from the processing parameters and the use of additives (smoking

and seasoning), and the variety of aroma active compounds, such as the presence of phenolic and terpene compounds (Flores and Olivares, 2015).

3.1 Aldehydes

Aldehydes are one of the most important chemical groups in fermented sausage aroma and are formed as a result of the breakdown of hydroperoxides. Aldehydes formed by fatty acid oxidation have a great influence on the overall aroma of meat products due to the typical aroma and low scent threshold. In fermented meat products, mainly hexanal, and generally pentanal, octanal and 2-nonanal compounds are detected (Ercoşkun et al., 2004; Marco et al., 2007). As the fermentation period extends, the amount of aldehyde increases, and this compound has an effect on the aroma of meat even at low concentrations (Kaban and Kaya 2007). Aldehydes generally add scents of green plants, cut grass and greasy to foods (Kesen et al., 2014). While 2-heptenal in meat products causes a dense mold scent, while nonanal, 4-heptenal, 2,4 decadienal lead to oily, stale, and unpleasant scents. Benzaldehyde compounds support the desired fermented meat flavor (Ercoşkun and Ertaş, 2003; Flores and Olivares, 2015; Gandemer, 2002; Gök, 2006). The aromatic compounds included in the aldehydes group in fermented meat products and their sensory descriptions are given in Table 1 (Flores and Olivares, 2015).

Table 1 The aromatic compounds included in the aldehydes group in fermented meat products and their sensory descriptions

Aldehyde	**Sensory descriptors**
Hexanal	Vegetables, fresh-cut grass, green
2-Hexenal	Cooked potatoes, salty meat, meat broth
Pentanal	Synthetic, green leaf, rancid
Octanal	Geranium, floral, citrus, nettle, dry
Nonanal	Herbal, geranium, nettle, dry, soap
2-Nonenal	Cucumber, herbal, wood, caramel
2-Heptenal	Rancid, dirty
4-Heptenal	Nasty bread
2,4-Decadienal	Fried, rancid, greasy
Benzaldehyde	Fresh, pine, herbal, spices
Acetaldehyde	Green
2-Methyl-butanal	Bitter cheese, fruity, caramel, rancid
2-Methyl-propanal	Fresh
Butanal	Sweet, snacks

3.2 Ketones

Ketones formed by lipid oxidation are mainly methyl ketones. Possible origins of methyl ketones are β-oxidation of free fatty acids by bacteria. Therefore, the choice of starter culture affects the balance between the oxidation products formed as a result of autoxidation of fatty acids and β-oxidation. Ketones formed as a result of the oxidation of fats also significantly affect the aroma in fermented meat products. Besides the butter aroma produced by 2,3-butanedione (diacetyl), ketones exhibit very variable flavor characteristics such as fruity, buttery or cheesy. In addition, the formation of 1-octen-3-one in sausage increases during fermentation. These compounds also create a metallic or mushroom-like flavor (Ercoşkun and Ertaş, 2003; Ercoşkun et al., 2004; Flores and Olivares, 2015). The aromatic compounds included in the ketones group in fermented meat products and their sensory descriptions are given in Table 2 (Flores and Olivares, 2015).

Table 2 The aromatic compounds included in the ketones group in fermented meat products and their sensory descriptions

Ketones	**Sensory descriptors**
2-Heptanone	Nettle, fruity, medicinal
2,3-butanedione (diacetyl)	Butter, cheese
2,3-Pentanedione	Butter
3-Hydroxy-2-butanone	Slight buttery
1-Octen-3-one	Mushroom
3-Octen-2-one	Mushroom, metali
2-Nonanone	Herbal, mushroom, slight fruity

3.3 Terpenes

Terpenes produce herbal aromas such as resin, pine and herb. Limonene is often found in fermented sausages that contain spices such as peppers, and among them, linalool has also been described as a strong flavor active compound. α-terpinen, which is included in the terpenes group and found in pepper and some other spices, has also been identified in sausage samples. Other terpenes identified in sausage are α-terpineol, β-pinene, β-mircene, linalool, α-pinene, felandrene and 3-carene. It is stated that terpenes constitute a significant part and even more than 50% of the aromatic compounds obtained in some fermented meat products. For example, Kaban (2010) states that the proportion of terpenes in sausage samples varies between 56.11% and 76.32%. As a result of a study conducted by Sezer Çelebi (2012), 34 terpenic compounds were detected in sausage samples, and terpenes were found to be higher than other total

volatile compounds. The ratio of terpenes varies depending on the sausage formulation. These differences may arise from the variety and amount of spices used in production, as well as from the feed the animals eat (Demirel and Gürler, 2017; Flores and Olivares, 2015; Kaban and Kaya, 2007; Kaban, 2010). The aromatic compounds included in the terpenes group in fermented meat products and their sensory descriptions are given in Table 3 (Flores and Olivares, 2015).

Table 3 The aromatic compounds included in the terpenes group in fermented meat products and their sensory descriptions

Terpenes	**Sensory descriptors**
Limonene	Menthol, herbal, fresh, citric, orange
Linalool	Intense floral, rose
Terpinene	Herbal
Terpineol	Green
β-Pinene	Pungent
β-Mircene	Lemon, fruity, green, herbal, spice
Felandrene	Lemon, fruity, green
3-Carene	Unpleasant

3.4 Aromatic Hydrocarbons

Phenolic compounds are characteristic in fermented smoked meats. For this reason, most of the phenolic compounds have been detected in Hungarian smoked salami. These 2-methoxy phenol (guaiacol) and 4-methyl phenol are the strongest aromas (Flores and Olivares, 2015).

In fermented sausages, volatile phenol compounds can be of spice origin. As a result of a study, it was determined that the sausage samples contained volatile phenols such as methyl eugenol, eugenol and 2,4-bis-1,1-dimethyl phenol, and their amounts varied between 143.51 and 2338.48 µg / kg (Ünal et al., 2017).

Aliphatic and aromatic hydrocarbons constitute another group of volatile compounds identified in fermented sausages. In a study by Kaban (2010), 10 aliphatic (0.14-8.03%) and 7 aromatic hydrocarbons (0.91-12.17%) were determined in sausage samples. The sources of these compounds vary widely. Aliphatic hydrocarbons, which are secondary products of lipid oxidation, do not make a significant contribution to the aroma due to their high sensory threshold. Aromatic hydrocarbons, on the other hand, are more effective on aroma. Among aromatic hydrocarbons, toluene (methyl benzene) can be caused by compounds formed as a result of lipid breakdown. This compound is also found in herbs used as animal

feed. Styrene is also found in herbs used in animal feeding (Kaban and Kaya, 2007; Kaban, 2010). The aromatic compounds included in the aromatic hydrocarbons group in fermented meat products and their sensory descriptions are given in Table 4 (Flores and Olivares, 2015).

Table 4 The aromatic compounds included in the aromatic hydrocarbons group in fermented meat products and their sensory descriptions

Volatile phenols	**Sensory descriptors**
2-Metoxyphenol (guiaicol)	Cooked sausage, smoky, sweet
4-Methyl-phenol	Stable, musty, smoky
3-Methyl-phenol	Smoke, phenolic
Eugenol	Smoky, spice, clove
Isoeugenol	Clove

3.5 Acids

Many acids such as acetic acid, butanoic acid, 3-methyl butanoic acid, propanoic acid, pentanoic acid, hexanoic acid, decanoic acid, octanoic acid have been identified in fermented meat products. In addition, carboxylic acids also contribute to the vinegar and cheesy aroma in fermented sausages (Kaban and Kaya, 2007; Flores and Olivares, 2015). While these compounds are mostly produced by microorganisms as a result of carbohydrate fermentation, they can also be formed by lipid oxidation. These fatty acids may be precursors of different compounds that affect aroma, but due to their high scent threshold values, acids do not directly contribute to the overall flavor of sausage (Ercoşkun and Ertaş, 2003; Ünal et al., 2017). The aromatic compounds included in the acids group in fermented meat products and their sensory descriptions are given in Table 5 (Flores and Olivares, 2015).

Table 5 The aromatic compounds included in the acids group in fermented meat products and their sensory descriptions

Acids	**Sensory descriptors**
Acetic acid	Vinegar, sharp, sour
Butanoic acid	Strong cheese, sweaty
3-methyl-butanoic acid	Cheese, feet, dirty shocks, sweaty
Propanoic acid	Slight sour, sweaty, cheese
Pentanoic acid	Sweaty
Hexanoic acid	Sweaty, rotten
Decanoic acid	Pungent
Octanoic acid	Rancid, wood, toasted

3.6 Alcohols

Alcohols in fermented meats are usually caused by lipid oxidation. However, they can also occur as a result of carbohydrate metabolism and amino acid catabolism. In general, alcohol compounds have not been identified as important aromatic contributors in fermented sausages. This may be due to the high detection threshold of alcohol compounds. In his study, Kaban (2010) detected seven different alcohols in sausage, and the only alcohol determined in all of the samples examined was benzenemethanol, 4- (1-methylethyl). Aliphatic linear alcohols generally are formed by degradation of lipid hydroperoxides. Branched alcohols can be formed from amino acids by Strecker degradation (Flores and Olivares, 2015; Kaban and Kaya, 2007; Kaban, 2010; Ünal et al., 2017). The aromatic compounds included in the alcohols group in fermented meat products and their sensory descriptions are given in Table 6 (Flores and Olivares, 2015).

Table 6 The aromatic compounds included in the alcohols group in fermented meat products and their sensory descriptions

Alcohols	**Sensory descriptors**
Ethanol	Baker's bread, yeast
1-Propanol	Fresh, herbal
1-Pentanol	Toasted, toasted meat, pine
1-Octen-3-ol	Mushroom
1-Hexanol	Green grass, plastic
2-Heptanol	Plastic, pork scratchings

3.7 Esters

Many ester compounds have been identified as responsible for fruity and caramel aromas in fermented sausages. Most of the esters are ethyl esters. Among them, the ones with the strongest aromas are ethyl butanoate, ethyl 2-methyl-butanoate and ethyl pentanoate. The formation of esters in fermented meat products depends more on microbial factors compared to other reactions. Due to their low scent thresholds and well-known effects on the overall flavor of food products, esters are remarkable aroma compounds that provide sausage samples with a fruity and pleasant aroma (Ercoşkun and Ertaş, 2003; Flores and Olivares, 2015; Ünal et al., 2017). The aromatic compounds included in the esters group in fermented meat products and their sensory descriptions are given in Table 7 (Flores and Olivares, 2015).

Table 7 The aromatic compounds included in the esters group in fermented meat products and their sensory descriptions

Esters	Sensory descriptors
Ethyl butanoate	Fruity, caramel, pineapple, strawberry
Ethyl 2-Methyl-butanoate	Sweet, pineapple, fruity, strawberry
Ethyl Pentanoate	Fruity, strawberry
Ethyl 2-Methyl-propanoate	Pineapple, strawberry, fruity, caramel
Propyl acetate	Apple, caramel, fruity, floral
Methyl butanoate	Fruity, floral
2-methyl-propyl acetate	Fruity

3.8 Sulfur and Nitrogen Compounds

Sulfur compounds are characterized by low threshold values and the characteristic aroma defined as garlic, onion, cooked potatoes and sometimes cooked meat. The strongest scents reported in fermented meats are diallyl sulfide, diallyl disulfide, dimethyl disulfide, methional (3-methylthiopropanal) and methanethiol (Flores and Olivares, 2015). Compounds containing different proportions and types of sulfur have been identified in fermented meat products. Kaban (2010) identified 11 sulfur compounds in sausage in his study and stated that most of these compounds originated from the spices used in the formulation, especially garlic (Kaban and Kaya, 2007; Kaban, 2010). The aromatic compounds included in the sulfur group in fermented meat products and their sensory descriptions are given in Table 8 (Flores and Olivares, 2015).

Table 8 The aromatic compounds included in the sulfur group in fermented meat products and their sensory descriptions

Sulfur compounds	Sensory descriptors
Diallyl sulfide	Garlic
Diallyl disulfide	Garlic
Dimethyl disulfide	Garlic, caramel, toasted
Methional	Cooked potato, brothy, rancid
Methanethiol	Rotten eggs, coliflower, unpleasant
Methyl-allyl sulfide	Onion, unpleasant, garlic
2-Methyl-3-furyl disulfide	Cooked meat

Nitrogenous compounds are commonly defined as small flavor compounds in cooked meat due to their characteristic fried and nut aroma. Also, 2-acetyl-pyrroline has been described as one of the strongest aromas in fermented sausages. Among the nitrogenous compounds, there are

chemical groups such as nitriles and nitroalkanes. These compounds originate from the addition of proteolysis and amino acid degradation products in the lipid oxidation reaction and nitrate and nitrite added to the product (Ercoşkun and Ertaş, 2003; Flores and Olivares, 2015). The aromatic compounds included in the nitrogen group in fermented meat products and their sensory descriptions are given in Table 9 (Flores and Olivares, 2015).

Table 9 The aromatic compounds included in the nitrogen group in fermented meat products and their sensory descriptions

Nitrogen compounds	**Sensory descriptors**
2-Acetyl-pyrroline	Toasted, popcorn, toasted nuts
Dimethyl pyrazine	Toasted coffee, toasted bread
Tetramethyl pyrazine	Toasted sugar
1-Methyl-pyrrol	Toasted, brothy

4. CONCLUSION

The fermentation and maturation stages cause the typical organoleptic properties of fermented meat products to take shape, such as color, flavor, aroma and texture. Especially the aroma is perhaps one of the most important sensory properties of fermented meats, as it persuades the consumer to buy the product. As in all foods, aroma in fermented meat products is not dependent on a single ingredient and is formed as a result of the combination of different ingredients in certain proportions. These aromatic compounds that make up the product aroma are formed by the breakdown products of proteolysis and lipolysis reactions, especially by microbial and endogenous enzymes.

Aldehydes, ketones, terpenes, aromatic hydrocarbons, acids, alcohols, esters, sulfur and nitrogen compounds are commonly found in fermented meat products as aromatic compounds. These aromatic compounds vary depending on the properties of raw meat used in fermented meat products, the amount and type of aromatic compounds, starter cultures and maturing conditions, additives used and production conditions.

In this study, some of the aromatic compounds formed in fermented meat products were compiled in accordance with the literature. Hundreds of volatile compounds have been identified in fermented meat products in various studies, but very few of them have been studied to elucidate the flavor active compounds. Moreover, more information is needed on the sources of aroma active compounds, their formation pathways and suitable conditions to impart enhanced flavor to fermented meat products.

References

Başyiğit, G., Karahan, A.G. and Kılıç, B. (2007). Functional starter cultures and probiotics in fermented meat products. *Turkish Journal of Hygiene and Experimental Biology*, 64 (2), 60-69.

Casaburi, A., Di Monaco, R., Cavella, S., Toldrá, F., Ercolini, D. and Villani, F. (2008). Proteolytic and lipolytic starter cultures and their effect on traditional fermented sausages ripening and sensory traits. *Food Microbiology,* 25(2), 335-347.

Corral S, Salvador A. and Flores, M. (2013). Salt reduction in slow fermented sausages affects the generation of aroma active compounds. *Meat Science*, 93, 776–785.

Demirel, N.Y. and Gürler, Z. (2017). Investigation of the effect of microorganism combinations used in fermented sausage production on flavor development. *Eurasian Journal of Veterinary Sciences*, 33 (1), 34-39.

Ercoşkun, H. and Ertaş, A.H. (2003). Flavor components and formation of fermented meat products. *Journal of Food Engineering*, 7 (16), 38-44.

Ercoşkun, H., Kiralan, M. and Işıksal, S. (2004). Lipid reactions in fermented meat products. *Food Engineering Journal*, 8 (18), 38-46.

Flores, M., Soler, C., Aristo, M.C. and Toldra, F. (2006). Effect of brine thawing/salting for time reduction in spanish dry cured ham manufacturing on proteolysis and lipolysis during salting and post-salting periods. *Eur. Food Res. Technol.,* 222, 509-515.

Flores, M. and Olivares, A. (2015). Flavor. F. Toldrá, Y. Hui, I. Astiasarán, J. Sebranek, R. Talon, *Handbook of Fermented Meat and Poultry* (s.217-225), Wiley Online Library.

Gandemer, G. (2002). Lipids in muscles and adipose tissues, changes during processing and sensory properties of meat products. *Meat Science*, 62(3), 309-321.

Gök, V. (2006). Effects of antioxidant use on some quality properties of fermented sausages (*Doctoral Thesis*). Ankara University, Institute of Science, Ankara.

Gökalp, H.Y., Ercoşkun, H. and Çon A.H. (1998). Some biochemical reactions and effects on aroma in fermented meat products. *Pamukkale University Faculty of Engineering, Journal of Engineering Sciences,* 3 (4), 805-811.

Kaban, G. and Kaya, M. (2007). Volatile compounds in fermented sausages. Atatürk University, Faculty of Agriculture, 38 (2), 225-230.

Kaban, G. (2010). Volatile compounds of traditional turkish dry fermented sausage (sucuk). International *Journal of Food Properties*, 13(3),525-534.

Kaban, G. and Kaya, M. (2011). Volatile compounds of traditionally produced pastırma. *Fleıschwırtschaft*, 91(4),112-116.

Kesen, S., Kelebek, H. and Selli, S. (2014). Characterization of the key aroma compounds in Turkish olive oils from different geographic origins by application of aroma extract dilution analysis (AEDA). *Journal of Agricultural and Food Chemistry*, 62(2), 391-401.

Laslo, É., György, É. and Czikó, A. (2019). Meat starter cultures: Isolation and characterization of lactic acid bacteria from traditional sausages. *Acta Universitatis Sapientiae Alimentaria*, 12(1), 54-69.

Liu, X.S., Liu, J.B., Yang, Z. M., Song, H.L., Liu, Y. and Zou, T.T. (2014). Aroma-active compounds in jinhua ham produced with different fermentation periods. *Molecules*, *19*(11), 19097-19113.

Macedo, R.E.F., Luciano, F.B., Cordeiro, R.P. and Udenigwe, C.C. (2017). Sausages and other fermented meat products. Starter Cultures in Food Production, Ed: Speranza, B., Bevilacqua, A., Corbo, M. R., Sinigaglia, M. Wiley-Blackwell, Chichester, 324-354.

Marco, A., Navarro, J.L. and Flores, M. (2007). Quantification of selected odor-active constituents in dry fermented sausages prepared with different curing salts. *Journal of Agricultural and Food Chemistry*, 55(8), 3058–3065.

Martín-Sánchez, A.M., Chaves-López, C., Sendra, E., Sayas, E., Fenández-López, J. and Pérez-Álvarez, J. Á. (2011). Lipolysis, proteolysis and sensory characteristics of a Spanish fermented dry-cured meat product (salchichón) with oregano essential oil used as surface mold inhibitor. *Meat Science*, 89(1), 35-44.

Olivares, A., Navarro, J.L. and Flores, M. (2011). Effect of fat content on aroma generation during processing of dry fermented sausages. *Meat Science*, 87(3), 264-273.

Ojha, K.S., Kerry, J.P., Duffy, G., Beresford, T. and Tiwari, B.K. (2015). Technological advances for enhancing quality and safety of fermented meat products. *Trends in Food Science & Technology*, 44(1), 105-116.

Öziş, G. (2014). The Effects of some organic acids and their salts on some properties of fermented sausage (*Master Thesis*). Abant İzzet Baysal University, Institute of Science, Bolu.

Öztan, A. (1999). Meat Science and Technology, 3rd Edition, Hacettepe University Publications, Ankara.

Resconi, V.C., Escudero, A. and Campo, M.M. (2013). The development of aromas in ruminant meat. *Molecules*,18(6), 6748-81.

Rotsatchakul, P., Visesanguan, W., Smitinont, T. and Chaiseri, S. (2009). Changes in volatile compounds during fermentation of nham (Thai fermented sausage). *International Food Research Journal*, 16, 391-414.

Serdaroğlu, M. and Tömek, S. (1995). The importance of proteolytic enzymes in fermented meat products. Pamukkale University Faculty of Engineering, *Journal of Engineering Sciences*, 3(1), 89-94.

Sezer Çelebi, Y. (2012). Determination of the potential use of some lactic acid bacteria isolated from fermented sausage as starter culture (*Master Thesis*). Erciyes University, Institute of Science, Kayseri.

Şanes, A. (2006). Production of functional (diet) sausage with reduced calories and fat (*Master Thesis*). Istanbul Technical University, Institute of Science, Istanbul.

Toldra, F. (1998). Proteolysis and lipolysis in flavour development of dry-cured meat products. *Meat Science*, 49(1), 101-110.

Toldra, F., Sanz, Y. and Lores, M. (2001). Meat Fermentation Technology, In Hui, Y.H. Ed.. Meat Science Applications. Marcel Dekker Incorporated, New York, USA.

Ulusoy, B.H. (2007). Production of fermented sausage with kefir culture (*PhD Thesis*). Istanbul University, Institute of Health Sciences, Istanbul.

Ünal, E., Erginkaya, Z. and Selli, S. (2017). The effect of microencapsulated Lactobacillus rhamnosus and storage period on aroma properties of Turkish dry-fermented sausage (sucuk). *Journal Of Food Measurement And Characterızatıon*, 1(1),1-11.

Van Ba, H., Hwang, I., Jeong, D. and Touseef, A. (2012). Principle of meat aroma flavors and future prospect. Latest research into quality control, Ed: Akayar, I. Intech Open Access Publisher, London, 145–176.

Wang, W., Xia, W., Gao, P., Xu, Y. and Jiang, Q. (2017). Proteolysis during fermentation of Suanyu as a traditional fermented fish product of China. *International Journal of Food Properties*, 20(1), S166-S176.

Yetim, H. (2013). Isolation, identification and determination of important technological and functional properties of yeast in traditional fermented sausages for use as starter culture. Erciyes University Scientific Research Projects Coordination Unit, Kayseri.

Yılmaz, İ. and Velioğlu, H.M. (2009). Fermented meat products. *Quality of Meat and Meat Products*. Transworld Research Network, 99-114.

Zanardi, E., Ghidini, S., Battaglia, A. and Chizzolini, R. (2004). Lipolysis and lipid oxidation in fermented sausages depending on different processing conditions and different antioxidants. *Meat Science*, 66 (2), 415-423.

CHAPTER IX

BUILDING SCIENCE I EXPERIENCES AS AN APPLIED COURSE ON EMERGENCY REMOTE TEACHING (ERT) OF ARCHITECTURE

Seher GÜZELÇOBAN MAYUK

(Asst. Prof. Dr.); Gebze Technical University, Kocaeli, Turkey; sgmayuk@gtu.edu.tr; Orcid: 0000-0002-2676-4784

Elif ÖZER YÜKSEL

(Asst. Prof. Dr.); Gebze Technical University, Kocaeli, Turkey; e.yuksel@gtu.edu.tr; Orcid: 0000-0002-1041-8748

N. Özge ESENER

(Res. Asst.); Gebze Technical University, Kocaeli, Turkey; ozgeesener@gtu.edu.tr; Orcid: 0000-0002-3949-068X

Gizem ASLAN

(Res. Asst.); Gebze Technical University, Kocaeli, Turkey; gaslan@gtu.edu.tr; Orcid: 0000-0002-0430-5106

Merve ÖZDOĞAN

(Res. Asst.); Gebze Technical University, Kocaeli, Turkey; mozdogan@gtu.edu.tr; Orcid: 0000-0002-6643-1749

Çetin SÜALP

(Res. Asst.); Gebze Technical University, Kocaeli, Turkey; cetinsualp@gtu.edu.tr; Orcid: 0000-0002-1227-7774

1. Introduction

The Covid-19 pandemic emerged in mid-March 2020 in Turkey when were the early days of the spring semester. After this time, all schools and universities were being announced to close and the rapid transition of education has started to online and digital education formats for adopting remote modes of teaching and learning (Green et al., 2020). Well-planned online learning experiences are meaningfully different from courses offered online in response to a crisis or disaster (Hodges et al., 2020). As a frontline emergency service, this educational transition method with

remote learning and educational technologies repositioned is named as an emergency remote teaching (ERT) method (Green et al., 2020).

Yıldırım (2020) said that the remote education had started with letters in the 1700s. It shows that the embedding of digital technologies as part of educational practices is neither new nor unique to the global pandemic (Green et al., 2020). However, it can be said that the use of ERT in architecture education has no longer time. When the literature is reviewed, many studies are encountered on subjects such as emergency remote teaching and distance education (Dikmen and Bahçeci, 2020; Durak et al., 2020; Green et al., 2020; Hodges et al., 2020; Keskin and Özer Kaya, 2020; Whittle et al., 2020; Yıldırım, 2020; Yılmaz İnce et al., 2020). Kauser (2020) can be reached as a resource on emergency remote teaching (ERT) of architecture. In this sense, it can be said that there is a deficiency in the literature about teaching with ERT in architecture.

Conventionally architecture education is going by interactive ways. Especially at design studios, it includes a group working with collaborative teaching and learning for developing students' creative skills. Because of this, the students need to interact or discuss together with their teachers and other students (Kauser, 2020). For this reason, examining the use of ERT in architecture education is necessary for these Covid-19 pandemic conditions. In addition to this, it can be also said that the use of ERT in applied courses is a difficult method. Building science courses in architecture education, which are applied courses, have two main parts. One of them is theory and the other is practice. It can be said that the ERT method is more suitable for the theory part rather than practice.

On the other hand, the features of the generation gain importance in the methods to be used in today's learning environment (Güzelçoban Mayuk and Coşgun, 2020). Generation Z individuals, who were born after 2000s, take part as learners in building science courses nowadays. Generation Z is also referred to by various names such as "internet generation, digital generation, millennium generation" because of their born age's features. They are said to be individuals who integrate technology with their lives, have social network affiliations, have a fondness for virtual games, have an interest in global issues and have high adaptability. It is also mentioned that they are open to innovation, optimistic, talented, goal-oriented, well-educated, self-confident, easily bored and capable of performing multiple skills simultaneously (Erden, 2017). The individuals of this generation are stated as individuals who learn knowledge fast, prefer graphic expression, prioritize winning and are competitive (Ardıç and Altun, 2017). Based on these features, it can be said that digital learning brought about by the Covid-19 period is compatible with the educational methods of generation

Z. It is known that one of these education methods is learning by doing method (Güzelçoban Mayuk and Coşgun, 2020). Learning by doing is a method to facilitate learning activity. In this method, all educational periods need to look, feel and be done as they are in real life (Erkan Yazıcı and Töre, 2014).

Within the scope of the study, the methods for the functioning of the Building Science I (BS I) course in the Covid-19 period were explained. BS I is a compulsory course in the curriculum of Gebze Technical University (GTU) Department of Architecture in the spring term and generation Z individuals take part as learners at this course on 2020 spring term. For this reason, the learning by doing method is used in this course on spring. The survey results at the end of the 2020 spring term conducted with the students taking the course were included in the study and the opinions of the students about the period and method were evaluated by this way. About GTU BS I course, the methodology of the course in the Covid-19 period and the evaluation survey and its results are given as parts of the study. It is completed with the conclusion part in accordance with the findings and discussion part.

2. About GTU Building Science I Course

Building Science I (BS I) is an ARCH 142 coded and compulsory undergraduate course, maintained in the second semester (spring) of the first year in architecture education at GTU. As of the 2017-2018 academic year, according to the updated course plan; BS I has 5 ECTS credits and 4 hours (2 hours of theory + 2 hours of practice + 0 hours of laboratory) a week. The requirement for the student attendance at the course is consisting of both theory and practice as 80 percentage.

The course requires face-to-face interaction. In the first two hours of the course, the lecturer gives theoretical information about building elements. Then he/she gives information about the homework or assignment (in-class practice work) of the week. Afterwards, the research assistants of the course help students with drawings and models during the in-class practice phase of the course. Assignments (in-class works), homeworks, exams, term projects (models, research projects) done during the semester are evaluated for the final gradation of course.

BS I is one of the fundamental courses of architectural education in GTU. In this course, the student learns the building components and the integration principles of components. Application assignments are significantly useful in this learning period. Through these assignments, the student learns to solve the structural problems encountered in project production phases.

The course includes that the explanations and applications of the basic principles of building science. It also includes the headings of the design of sub-systems, building foundations, walls, floors and joinery building elements. In addition to the theoretical explanations on reinforced concrete skeletal system and masonry building construction systems, wood and steel structural systems are included in the last weeks of the course.

The course continues with the course of Building Science II in the following semester at GTU. In BS II, theoretical information and various application assignments about vertical circulation tools and roof systems are given.

2.1 The Methodology of the BS I Course

In the past, mainly drawing and model assignments were used in GTU building science courses, but recently, education has been adapted for generation Z. In this period, the student is directed to do lots of research. Considering the close relationship of generation Z with technology, it is useful to push the student to find the right up-to-date information in the light of the knowledge he/she gained in the course and let him/her figure out how to solve the problem. In this way, it is hoped that the student will be able to develop creative architectural solutions for the problems he/she encounters in business life with his/her research skills and knowledge.

To adapt the education system to generation Z, the 'learning by doing' method has been prioritized. In this method, students are provided to develop their work with research based on the information they have acquired in the course and to produce models in desired scales. In this way, it is aimed for them to learn the theory and practice by experiencing. The models produced are considered as term projects. Model deliveries are completed with daily detail workshops. In this way, it is aimed that students will develop their integrated thinking skills in a more flexible production environment (Güzelçoban Mayuk and Coşgun, 2020).

Students who have developed problem-solving and integrated thinking skills can use the knowledge and skills they have learned in the BS I course in other undergraduate courses as well. Thus, it has been ensured that the BS I course is also integrated into the Architectural Design Studio course. For a holistic architectural education, importance has been placed on the synchronization of these two courses and their feeding each other.

2.2 The Methodology of the Course in the Covid-19 Period at 2019-20 Spring Semester

Arch 142 Building Science I was conducted in the 2019-2020 Spring Semester with Covid-19 conditions. The courses are conducted with a

group of faculty members, which vary according to the semesters. In the lessons, theoretical information is conveyed mostly by the lecturer and the courses are completed with the applications carried out by the research assistants. The BS I course in the spring semester of 2019-2020 was conducted with two faculty members and four research assistants; a total of 78 students attended to the course.

In this context, the education, which was carried out face-to-face in the first four weeks of the term, was carried out with emergency remote education until the end of the term after a two-week break due to Covid-19 measures. BS I courses, which consist of theory and practice sections, were carried out simultaneously and asynchronously with the MS Teams program during the emergency remote education period. For this reason, the total number of applications and assignments during the term has been reduced. The updated workplan for the spring term of the course is included in Table 1.

The theory section of the course carried out with the presentations made by lecturers. Meanwhile, presentations were recorded. Thus, in addition to being able to follow the presentations by students simultaneously and students were provided to access the theoretical information of the concerned course at the end. For this purpose, course folders were created in the general channel where simultaneous courses are conducted in MS Teams. By this way, the access of all course documents was provided.

The application section of the course was carried out under the control of research assistants. Before the concerned week of the course, the theoretical presentation and application files of that week were uploaded to the application group channels opened in MS Teams by the research assistant of each group and the students were made ready for the course. In the education before Covid-19, the applications which in face-to-face were continued in the class after the theoretical presentations were turned into weekly assignments during the emergency remote teaching period. At the end of each simultaneous course, the assessment of the previous week's application stage was made and then the desired criteria were explained on the application of that week. In this stage, it is expected from students to upload the applications given as an assignment to the concerned folders of the group channels in MS Teams on the specified day and time. The assignments of the concerned week were graded in written explanations according to the required criteria by the research assistants carrying out each application group and announced to the students through the same channel. No restrictions were placed on the method of the application drawings of the students. They were expected to upload photographs of

their hand drawings or drawings made by using the other digital platforms to concerned MS Teams channel in desired formats.

Table 1 The workplan of the course in 2019-20 spring semester.

ARCH 142 BUILDING SCIENCE I

2019-2020 SPRING SEMESTER PLAN

WEEKS	CONTENTS	METHODS
Week 1	Introduction and general information about the method and the scope of the lecture, conceptual definitions.	Face-to-Face Teaching
Week 2	Foundation systems **Practice 1** **Assignment 1**	Face-to-Face Teaching
Week 3	Carcass system foundations **Practice 2** **Assignment 2**	Face-to-Face Teaching
Week 4	Raft foundation, insulation against water and humidity, the elements of carcass system **Practice 3**	Face-to-Face Teaching
Week 5	**Break of Covid-19**	No Course
Week 6	**Break of Covid-19**	No Course
Week 7	**Online Trial Course** Wall sytems **Practice 4 // Assignment 4**	Emergency Remote Teaching (ERT)
Week 8	Floor systems **Term Project:** Assignment of Research Project and Groups **Practice 5 // Assignment 5**	ERT
Week 9	Arch, vault, dome systems **Practice 6 // Assignment 6** **Assessment for the Term Project**	ERT
Week 10	Door and window system components **Practice 7 // Assignment 7**	ERT
Week 11	Door and window system components **Practice 8 // Assignment 8**	ERT
Week 12	Wood and steel construction systems **Practice 9 // Assignment 9** **Assessment for the Term Project review**	ERT
Week 13	**Term Project Presentations- Project Delivery**	ERT
Week 14	No Course (because of the date)	No Course

In addition to drawing the applications given as assignment during the application period in consultation with the concerned research assistant, it

was aimed that the students to research and make a literature review individually. It is aimed for students to turn the period into an opportunity and improve their learning skills with this application method emerged due to Covid-19. In this respect, it was ensured that students experienced the digital technology as a learning tool, which they started to use in the early stage of architecture education with the BS I course during the Covid-19.

In the exam stages, that could not carry out face to face, are integrated into emergency remote teaching in this period, and solutions have been applied to increase research, experience, and integration. Exams were conducted as follows:

In the mid-term exam, a research assignment was given to students to question, consolidate, and develop the information, which they achieved as a result of theoretical and applied training. In the related assignment; the students were expected to prepare a report by examining and analyzing from the site plan to the system details of a building, which they chose, in groups of 3-5, using the literature review method. In the report, the examination of the buildings has been requested to be made within the titles such as; general information about the building, site plan and layout decisions, construction system, structural elements, evaluation and result and bibliography. In addition to this report, students were expected to submit the results of their research as a five-minute video in which they presented as a group. The prepared video was watched simultaneously, and an environment was created in which the students would answer the questions to be asked. Assignments, which submitted on the online platform until the specified date, were evaluated with the criteria of the video and simultaneous presentation, the submitted reports and the suitability of the reports for the assignment.

In the final assignment, it is aimed that the students consolidate the knowledge they have acquired in the BS I course through the projects which they produce in the Architectural Design studios. In the assignment to be done individually, the students were asked to draw a part of their projects, carried out in the Architectural Design studios in the spring semester of 2019-2020, at 1/20 scale. Within the extent of the assignment, it is expected that the site plan, floor plans, sections and elevations will be submitted to understand their projects designed in studios. In the project of BS I final assignment, it was requested to submit 1/20 system detail drawings including plan-section-elevation of the partial sections which are selected with the lecturers. Grading of the assignments was made according to the evaluation criteria such as project submission, page layout and the conformity of the plan-section-elevations in the system detail to 1/20 scale.

As a make-up assignment, it was requested to submit a revised and detailed version of the assignment which made according to the critics given in the final assignment evaluation. The make-up assessment criteria were the same as those specified in the final assignment.

3. The Evaluation Survey and Its Results

70 students passed successfully of Arch 142 Building Science I course from the registered 78 students in the term of spring 2020. At the end of the semester, an evaluation survey was prepared over MS Teams in order to identify the deficiencies in lectures and also, to increase the quality of the course. The acquisitions, positive and negative aspects of the course, and their suggestions, if any, as well as their satisfaction level and their remote or face-to-face training preferences were also asked by this survey. 33 students participated that the attendance of 42% in this 6-questioned survey, which had 4 open-ended and 2 closed-ended questions. One of the closed-ended questions was a rating scale and the other one was a nominal question shown in Table 2.

Table 2 Ouestions of the evaluation survey for the BS I Course in Spring 2020

Question number	Question
1.	Can you convey your ACQUISITIONS from the Spring 2020 term of Arch 142 Building Science I course in three (3) words? (For example: research skill, teamwork, program planning…etc.)
2.	Could you tell us about the POSITIVE aspects of Arch142 Building Science I course about Spring 2020 term in three (3) words? (For example: lively, actual, lifelike)
3.	Could you tell us about the NEGATIVE aspects of Arch 142 Building Science I course about Spring 2020 term in three (3) words? (For example: none :))
4.	Are you satisfied that Arch 142 Building Science I course has been conducted with remote education in Spring 2020? (5 very satisfied, 4 satisfied, 3 neutral, 2 unsatisfied, 1 very unsatisfied)
5.	Arch 142 Building Science I course will be more efficient for Fall 2020 semester as ..... a. Face-to-face education b. Remote education c. Both
6.	What are your SUGGESTIONS, if any, of Arch 142 Building Science I course for Spring 2021?

The first open-ended question was replied with a rate of 70% by 32 students with 67 of 96 (32x3) statements. ‘Research & report skill’ was the prevalent opinion with 34% for the first question as an acquisition. ‘Teamwork’, ‘program planning’ and ‘digital drawing skill’ were the following answers with respectively 21, 16 and 11%. The second open-ended question was answered with a rate of 54% by 29 students with 47 of 87 (29x3) statements. ‘Instructive and technical’ was the common answer as a positive aspect with 23%. ‘Attractive and enjoyable’, ‘realistic’ and ‘lecturers taking care of students’ were the following answers with respectively 13, 11 and 11%. The third open-ended question was replied with a rate of 48% by 28 students with 40 of 84 (28x3) statements. ‘Info confusion / can't reach correct info’ was the common answer as a negative aspect with 20%. ‘Too much course load’, ‘thinks he/she got an undeserved grade’ and ‘none’ were the following answers with respectively 15, 13 and 10%. Some of the remarkable answers among the others were ‘to be able to repeat lessons at any time thanks to the recording of lessons’ and ‘Remote education caused a fair environment because of the absence of the noise in the classroom’.

The fourth open-ended question (the sixth one) was replied by 22 students with 32 suggestions. ‘Applied education should be increased’ was a common suggestion with 22%. ‘The system that includes both training methods should be widespread’, ‘syllabus should be updated’ and ‘course load should be reduced’ were the following answers with respectively 13, 13 and 9%. Additionally, some of them have suggested that ‘online submissions should be continued’ and ‘final, which was a research and report homework, should be continued (Fig. 1).

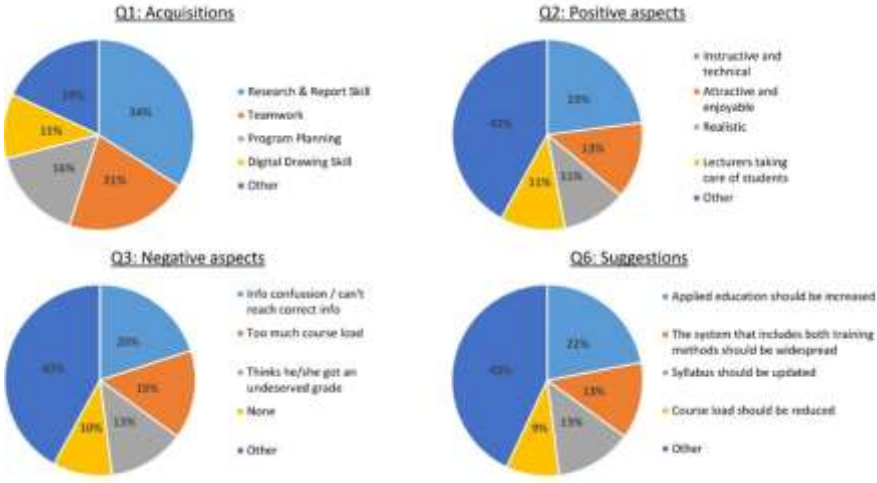

Figure 1 Illustration of the open-ended questions data.

The last two close-ended questions were replied by all the participants. The rating scale question that to evaluate the satisfaction of the remote education was gathered as 1 to 5 scoring. The students were very satisfied, who gave 5 points with a rate of 24%. They were satisfied, who gave 4 points with a rate of 21%. 28% of them were neutral, who gave 3 points. The unsatisfied and very unsatisfied groups were 21% and 6% of the participants respectively, who gave 2 and 1. Distribution of the feedbacks has been interpreted as a steady state from 2 to 5 that within the range of 20-30% each, except from 1 point with 6% whilst the satisfaction was seen as 73%. Also, face-to-face' method was selected as an efficient education method with a rate of 46% of the attendees. The following choices 'remote' and 'both' were chosen by 27% for each of them. According to the survey, it is seen that the 'face-to-face' education option is preferred almost twice by the students, comparing with the others (Fig. 2).

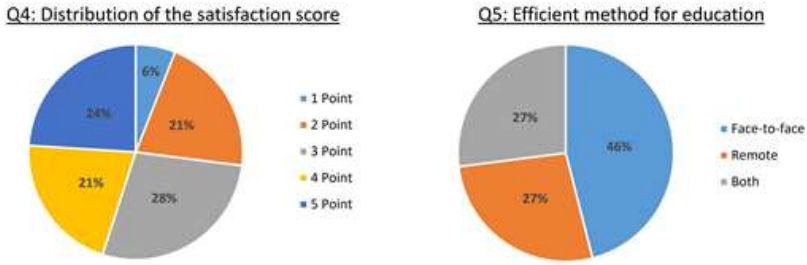

Figure 2 Illustration of the closed-ended questions.

4. Discussion and Conclusion

When the evaluation survey and its results are examined, the acquisitions from the Spring 2020 term of Arch 142 Building Science I course are seen as 'Research and report skill', 'teamwork', 'program planning' and 'digital drawing skill'. These achievements in this period, where students are aimed to learn by doing (experiencing) on their own, show that the Covid-19 period has turned into an opportunity for the BS I course.

When the positive aspects of the BS I course in the Covid-19 period are asked, 'instructive and technical', 'attractive and enjoyable', 'realistic' and 'lecturers taking care of students' are seen as the answers. In this sense, it is possible to say that the BS I course, which consists mostly of generation Z, has passed interesting despite all the difficulties of the period.

The negative aspects of the BS I course in this period are aligned as 'info confusion / can't reach correct info' 'too much course load' and 'thinks he/she got an undeserved grade'. Here, it can be said that such negative views are likely to occur during the rapid adaptation of ERT to

the period. At this point, efforts would be made for the solutions. In addition, it is pleasing to receive the answer of none in the survey as a negative opinion for the teachers.

The survey and its results show that there is a satisfaction generally with the BS I course conducted in the period. In this sense, 73% of students who score 3 and above appear to be. Some of the notable answers for this satisfaction were 'to be able to repeat lessons at any time thanks to the recording of lessons' and 'remote education caused a fair environment because of the absence of the noise in the classroom'. However, it is concluded that 46% of the class preferred face-to-face training. It is thought that the reason for this ratio may be the difficulties experienced in the period, related to the negative aspects mentioned in the previous questions.

Some suggestions of the students in the evaluation survey for the other BS courses in this Covid-19 period were specified as: 'Applied education should be increased', 'the system that includes both training methods should be widespread', 'syllabus should be updated' and 'course load should be reduced'. Additionally, 'online submissions should be continued' and 'final, which was a research and report homework, should be continued because of quite instructive' were some other suggestions. According to these suggestions and also this study results, new work plans for BS II courses in the fall term 2020 had been done.

It is also seen from the survey and results that the open-ended questions asked to the students were answered less. It shows that the generation Z members respond to optional questions and prefer to report their suggestions quickly. It can be seen that this situation coincides with the easily bored feature of generation Z. In order to solve this feature, it may be useful to direct questions to students.

In conclusion, it can be said that it was determined that the BS I course was conducted efficiently in the emergency remote teaching period. On the other hand, face-to-face teaching was preferred by students more in applied courses. In the Covid-19 period, which is expected to continue, it is important to receive a lot of feedback as in this study to carry out the applied lessons more efficiently.

Acknowledgements

We would like to thank all the students who participated to the Building Science I course and evaluation survey in the 2019-20 spring term at Gebze Technical University Department of Architecture.

Unless otherwise stated, the figures and tables used in the article belong to the authors.

References

Ardıç, E, & Altun, A. (2017). Dijital Çağın Öğreneni. International Journal of New Aproaches in Social Studies-IJONASS. 1 (1), pp.12-30. Retrieved from: https://dergipark.org.tr/tr/pub/sbyy/issue/34271/374055

Dikmen, S, & Bahçeci, F. (2020). Covid-19 Pandemisi Sürecinde Yükseköğretim Kurumlarının Uzaktan Eğitime Yönelik Stratejileri: Fırat Üniversitesi Örneği. Turkish Journal of Educational Studies, 7 (2), pp.78-98. Retrieved from: https://dergipark.org.tr/tr/pub/turkjes/issue/54378/721685

Durak, G., Çankaya, S., & İzmirli, S. (2020). Examining the Turkish Universities' Distance Education Systems during the Covid-19 Pandemic. Necatibey Faculty of Education, Electronic Journal of Science and Mathematics Education (EFMED). 14 (1), pp.787-809. Retrieved from: https://dergipark.org.tr/tr/download/article-file/1187187

Erden, N. S. (2017). Yeni Nesillere Yeni Öğretim Yöntemleri: Z kuşağının Öğrenme Stilleri ve Yükseköğrenim için Öneriler. International Journal of Academic Value Studies (Javstudies). 3 (12), pp.249-257. Retrieved from: https://dergipark.org.tr/tr/pub/usaksosbil/issue/49807/606096

Erkan Yazıcı, Y., & Töre, E. (2014). Mimarlık Eğitiminde Yaparak Öğrenme: Kentsel Tasarımdan Mimari Tasarıma Yenikapı-İnebey Örneği. Journal of Education and Science. 39 (175), pp.296-308. Retrieved from: http://egitimvebilim.ted.org.tr/index.php/EB/article/view/2534

Green, J. K., Burrow, M. S., & Carvalho, L. (2020). Designing for transition: Supporting teachers and students cope with emergency remote education. Springer Nature Postdigital Science and Education. Retrieved from: https://link.springer.com/article/10.1007/s42438-020-00185-6

Güzelçoban Mayuk, S., & Coşgun, N. (2020). Learning by Doing in Architecture Education: Building Science Course Example. International Journal of Education in Architecture and Design (IJEAD). 1 (1), pp. 2-15. Retrieved from: https://dergipark.org.tr/tr/pub/ijead/issue/53504/681120

Hodges, C., Moore, S., Lockee, B., Trust, T. & Bond, A. (2020). The difference between Emergency Remote Teaching and Online Learning. EDUCAUSE Review. Retrieved from:

https://er.educause.edu/articles/2020/3/the-difference-between-emergency-remote-teaching-and- online-learning

Kauser, N. (2020). Rethinking Architecture Pedagogy in the Era of Pandemics. Charrette. pp.1-6. Retrieved from: https://www.researchgate.net/publication/343904568_Rethinking_architecture_pedagogy_in_the_era_of_pandemics

Keskin, M., & Özer Kaya, D. (2020). Covid-19 Sürecinde Öğrencilerin Web Tabanlı Uzaktan Eğitime Yönelik Geri Bildirimlerinin Değerlendirilmesi. İzmir Katip Çelebi University Faculty of Health Science Journal. 5 (2), pp. 59-67. Retrieved from: https://dergipark.org.tr/en/pub/ikcusbfd/issue/55773/754174

Whittle, C., Tiwari, S., Yan, S., & Williams, J. (2020). Emergency Remote Teaching Environment: A Conceptual Framework for Responsive Online Teaching in Crises. Emerald Insight. Retrieved from: https://www.emerald.com/insight/content/doi/10.1108/ILS-04-2020-0099/full/pdf?title=emergency-remote-teaching-environment-a-conceptual-framework-for-responsive-online-teaching-in-crises

Yıldırım, K. (2020). Lessons from an Exceptional Distance Education Experience. Critical Reviews in Educational Sciences (CRES). 1 (1), pp. 7-15. Retrieved from: https://www.researchgate.net/publication/343737392_Istisnai_Bir_Uzaktan_Egitim-Ogretim_Deneyiminin_Ogrettikleri

Yılmaz İnce, E., Kabul, A., & Diler, İ. (2020). Distance Education in Higher Education in the Covid-19 Pandemic Process: A case of Isparta Applied Sciences University. International Journal of Technology in Education and Science (IJTES). 4 (4), pp. 343-351. Retrieved from: https://ijtes.net/index.php/ijtes/article/view/112

CHAPTER X

RISK ANALYSIS IN MARITIME LOGISTICS OPERATION PROCESS BY APPLYING DEMATEL METHOD

Sibel BAYAR

(Asst. Prof. Dr.); Istanbul University- Cerrahpasa, Engineering Faculty Department of Maritime Transportation Management Engineering, Istanbul, Turkey
email: sibelb@iuc.edu.tr, Orcid: 0000-0002-9169-935X

Ercan AKAN

(Asst. Prof. Dr.); Iskenderun Technical University, Barbaros Hayrettin Naval Architecture and Maritime Faculty Department of Maritime Transportation Management Engineering, Iskenderun, Turkey
email: ercan.akan@iste.edu.tr, Orcid: 0000-0003-0383-8290

1. Introduction

Maritime transportation is frequently used in international trade for large volumes of cargo due to its suitable cost advantage. Volume of international maritime trade occurred 11.08 billion ton in 2019. (UNCTAD, 2020). However, in order to decrease the transportation costs, the ships' size increases and with the technology, the duration of the ships and cargoes at the port decreases. For such reasons, maritime logistics complicates the operational processes and this process needs to be managed quickly. The complexity and speed of the process also bring risks in maritime logistics operation processes.

Maritime logistics encompasses maritime transport (shipment and seaports), traditional logistics functions (e.g., warehousing, providing distribution center services) and activities of integrated logistics (e.g., repair, labeling, assembly) (Nam and Song, 2011). A maritime logistics occurs primary and secondary activities. The primary activities define core activities of maritime operators such as shipping lines, port/terminal operators and freight forwarders. Secondary activities are activities that assist their primary activities (Radhika, 2014). In this context logistic risks in CIF (Cost-Insurance-Freight) transportation process, which is one of the priority activities, were determined and the order of importance of

these risks and how they affect each other was analyzed by DEMATEL (Decision Making Trial and Evaluation Laboratory) method in the study. In the CIF (Cost-Insurance-Freight) contract, which is an INCOTERMS agreement to define regulations of responsibilities of buyers and sellers operating in the international trade system, the goods are deemed to have been delivered after getting on board. According to the CIF agreement, the seller is responsible for arranging and paying insurance for the goods and for all export transactions (Seredyuk, 2017).

2. Literature review

The emergence of the risk management discipline in terms of academic studies dates back to late 1950; even if risk management dates back to ancient times, such as the Bottomry method of handling Babylon's international trade risks in 2250 BC and the Phoenician merchant marine insurance regulations 3,000 years ago (Mokhtari and Ren,2014). As in many sectors, risk management is an important issue in maritime logistics, which includes complex processes. Maritime logistics and supply chain involves many risks which are operational, financial, cyber, environmental, social, business etc. in maritime industry such as seaport, shipping, shipyards (Papastergiou and Polemi, 2017). Therefore, there are many studies on the risks of maritime logistics processes (Grant and Elliot, 2018; Kalogeraki et al, 2018; Liu et al, 2019; Roh et al, 2018; Vilkoa et al, 2019; Yin et al, 2019).

Many methods such as Bayesian, FMEA, Simulation, Kaiser Normalization, FAHP, DEMATEL have been used in studies on risk management (Ganguly and Kumar, 2019; Govindan and Chaudhuri, 2016; Laudares et al, 2019; Zimon and Madzik, 2020). Rahman et al. (2020) analyzed a maritime logistics risk model with a Bayesian network (BN) at an offshore facility operating. Nguyen (2020) aimed to improve a quantitative model of operational risks in the context of container transportation. The risks were then evaluated according to a Fuzzy Rule Bayes Network (FRBN) model with a 2-level parameter structure before a meaningful interpretation was obtained with a new risk mapping approach. Faghih-Roohi et al. (2020), the TOPSIS-based FMEA approach proposed in an intuitive blurry environment offers the opportunity to collect the risk assessments of different experts in a practical and efficient way. Roh et al. (2018) analyzed the maritime supply chain safety risk in Malaysia's ports and waterways by applying a risk assessment matrix by developing a risk / loss exposure matrix.

In addition, Govindan and Chaudhuri (2016) analyzed the relationship between the risks by third-party logistics service providers (3PL) and one of their customers using DEMATEL. In the study, selection of the

appropriate methodology was followed to analyze the input from experts about the relationship between different logistics risk categories and the relationship between risk categories was analyzed. Du et al. (2019) analyzed the risk factor of cross-border e-commerce SMEs and developed a hybrid method for risk assessment and ranking called Kano-fuzzy DEMATEL. Different from those studies; in our study, the preferred logistics risks in maritime transportation were determined according to CIF (Cost-Insurance-Freight), and the order of importance of these risks and the risks that affect each other were analyzed with the DEMATEL method.

3. Risk management in maritime logistics

Both the large/rapid changes in the business environment and the complex structure of the logistics processes require an effective risk management of the process. Risk management is a fundamental element that affects the activities of the businesses excessively. They cause different risk situations, due to their complex structure (Nikolov and Tcholakova, 2015). In this context, risk is defined as the product of the damage potential and the probability of an uncertain future event (Habegger, 2008).

In the process of risk management, first of all, the scope, context and criteria of the risk are determined, then the risk assessment phase is started and risk definition analysis and risk identification are performed. After the risks are identified, the process of risk treatment is started. Later, after the monitoring and review phase, recording and reporting are made at the last stage in risk management (ISO, 2018).

In the risk management process, the organization must first identify the scope of activities of risk management. The scope should be clear about the relevant objectives to be considered and the risk management process in line with corporate objectives. The organization should indicate the risk type and amount to take or not in relation to the objectives. It should also identify criteria to assess the importance of risk and processes of support decision. Risk criteria must reflect the values, goals and resources of organization and be steady with policies and statements regarding risk management (ISO, 2018).

Risk assessment consists risk definition, risk analysis and risk assessment processes. Risk assessment should be done in a systematic, iterative and collaborative manner, drawing on stakeholders' knowledge and opinions. The goal of risk identification finds, distinguishes, and identifies risks' helping and preventing an organization from achieving. Risk analysis involves consideration of uncertainties, sources of risk,

results, possibilities, events, scenarios, controls and their effectiveness in detail. The aim of risk analysis understands the nature and characteristics of risk. Risk assessment includes comparing risk analysis results with defined risk criteria to determine where additional actions are required (ISO, 2018).

The selection of risk treatment options, another step, should be realized according to the goals, risk criteria and available resources of organization. The goal of risk treatment is to select and implement options to address risk (ISO, 2018).

Continuous monitoring and periodic review and its results is a planned part of the risk management process in which responsibilities are clearly defined. The goal of monitoring and review ensure and develop the effectiveness, and quality of process design, implementation and results. At the last stage, the risk management process and its results must be documented and reported (ISO, 2018).

Looking at the risk classification in terms of the logistics sector; risks can be examined in three parts. These are supply risk, production risk and transportation risk. Procurement risk (contract) is associated with the uncertainties that arise during the application process and the implementation of procurement operations. Production risk is associated with the decision-making process in the transportation and handling of material resources between enterprises in the region and in the creation of industrial infrastructure in the region. Transport risks in the logistics sector are characterized by the possibility of losses associated with the production of transport and logistics services, and the possibility of unmet demand for transport and logistics services undertaken by regional transport structures (Freydman, 2011).

In this context, the study aimed to analyze the transportation risks in the logistics sector, and the risks of the CIF (Cost, Insurance & Freight Prepaid) which mode of transportation of a maritime freight according to the Incoterms delivery methods were discussed. Incoterms are the rules that set out the responsibilities of buyer and seller, including the delivery methods and their status, determined by the International Chamber of Commerce and last updated in 2020. Incoterms 2020 sets out the rules for a total of 11 delivery types, 7 for all modes of transport and 4 for maritime and waterways transportation. In this context, the study requires the seller to deliver the products on board the ship, and the cost-insurance freight belongs to the seller, in the form of CIF transportation used only in maritime and waterways transportation. All risks and responsibilities before the delivery of the goods on board belong to the seller, and from this point on, they pass to the buyer (ICC, 2019). The operation processes

of CIF and which one is responsible for cost and risk in each of these processes are shown in Table 1 (Seredyuk, 2017).

The export company, which is a seller, firstly contracts with a logistics or freight forwarder company to make the transportation contract. In case of using CIF mode of transport; the company in question assumes the responsibilities of the seller and serves all logistics operations during this transportation process. Therefore; the risks of the processes under the responsibility of the seller are discussed in the study. In this context pre-transport, export customs, loading, main transport, as well as risks that may occur during the documentation process and the reservation stage of the logistics company are also discussed.

Table 1 CIF processes and responsibilities (Seredyuk,2017)

Process	**Costs**	**Risks**
Pre-Transport (including package)	Seller	Seller
Export Customs	Seller	Seller
Handling (Loading to ship)	Seller	Seller &Buyer
Main Transport (Maritime Transportation)	Seller	Buyer
Shipping Insurance	Seller	Buyer
Handling (Unloading to ship)	Buyer	Buyer
Import Customs	Buyer	Buyer
Last-Transport	Buyer	Buyer

The logistics firm that the seller has agreed with a CIF transport contract receives the cargo that needs to go to the port from the seller first, and perform the pre-packing process according to the agreement. After being loaded on the front transport vehicle, the vehicle moves towards the port and is loaded onto the ship after passing through the export customs clearance process at the port. The cargo is then transported on the ship. The seller company which is the logistics company is responsible for all transactions, documentation and cost-insurance and freight costs in this process. However, the buyer is responsible for the unloading of the cargo from the ship arriving at the destination port, import customs clearance and final transportation processes. Therefore, the risks that may occur in the event of a CIF transport were determined and the efficiency percentages of the risks were found by applying the DEMATEL method, and the risks affecting each other were also determined in the study.

4. DEMATEL method

The DEMATEL method is a method that performs its analysis by establishing a relationship between the criteria in a structural problem in

the context of causality (Wu and Lee, 2007). The DEMATEL method was developed within the Genoa Battele Institute in 1972-1976 to analyze the solution of complex problems (Huang et al., 2007). The DEMATEL method is a method that includes the cause-effect causality relationships between the criteria and is used to analyze these causality relationships (Aksakal and Dağdeviren, 2010; Karaoğlan, 2016). In this method, the comparison of the criteria is performed by the decision-makers, and then the relationships between the criteria are translated into local priorities. The weights of the criteria can be calculated, and prioritization can be made according to the order of importance of these criteria with DEMATEL method. Among the criteria, the high impact criteria are in an affecting position and have high priority.

While these criteria are expressed as affecting criteria, they are expressed as criteria that are affected criteria. Diagrams are used to better express the causal relationships of the relevant criteria (Seyed-Hosseini et al., 2006; Liou el al., 2008).

The stages of the DEMATEL method are listed as follows: (Li, 1999; Tzeng et al., 2007; Wu and Lee; 2007; Karaoğlan, 2016; Tzeng and Huang, 2011).

Step 1: Determining the criteria and creating the evaluation scale. In order to determine affecting and affected factors, meaningful relationships between these factors must be established by experts. In this step, first of all, the evaluation criteria for the problem are determined by the decision-makers. The evaluation scale is used in Table 2 for comparing the relationship between decision makers and criteria.

Table 2 Evaluation scale.

Numeric Value	Linguistic Variables
0	No Effect – (No)
1	Very Little Effective – (VL)
2	Less Effective – (L)
3	High Impact – (H)
4	Very High Impact – (VH)

Step 2: Set up a direct relationship matrix. In order to determine the levels of i $C = \{C_i \mid i = 1,\ 2,\ ...,\ n\}$ relationships between the criteria of decision makers, a pairwise comparison matrix is created by decision makers using the scale *Table* 2. *The equation* is expressed by (*1).* If the decision makers evaluating the binary comparison criteria are from the decision maker, the arithmetic average is taken in the scoring of the

comparisons. The resulting direct relationship matrix is X expressed by Equation *(2).*

$$X = \left(\frac{X^{(1)} + X^{(2)} + \cdots + X^{(p)}}{p} \right),\ k = (1,\ 2,\ ...,\ p),\ \forall k \in \mathrm{N} \qquad (1)$$

$$X = \begin{bmatrix} X_{11} & X_{12} & \cdots & X_{1n} \\ X_{21} & X_{22} & \cdots & X_{2n} \\ \vdots & \vdots & \ddots & \vdots \\ X_{n1} & X_{n2} & \cdots & X_{nn} \end{bmatrix} \qquad (2)$$

Step 3: Determining the normalized direct relationship matrix. Normalization process is performed with Equation (3) and Equation (4). Then a normalized Direct Relationship Matrix (T) is created.

$$T = rX \qquad (3)$$

$$r = \min_{1 \le i \le n} \left(\frac{1}{\max \sum_{i=1}^{n} a_{ij}},\ \frac{1}{\max \sum_{j=1}^{n} a_{ij}} \right) \qquad (4)$$

Step 4: Creating the total relationship matrix. The Total Relationship Matrix (F) is calculated by Equation (5), which includes the Normalized Direct Relationship Matrix (T) and the Unity Matrix (I). F matrix expresses the total relationship between the system factor pair.

$$F = \lim_{w \to oo} \left(T + T^2 + ... + T^w \right) = T\left(I - T \right)^{-1},\ \forall w \in \mathrm{N} \qquad (5)$$

Step 5: The effectiveness and degree of influence of the criteria are determined. By determining the affecting and affected criteria groups, the total relationship matrix (F) is determined to calculate the net impact degrees and the row and column totals are found. D_i; means that each criterion's line total affects other criteria. R_i; refers to the effect of each criterion on the row total, other criteria. D_i+R_i; expresses the importance of the criterion in the system by expressing the total impact value sent and received for each criterion. Alive; by expressing the total effect of each criterion on the system; if it is positive, it is indicated as affecting or if it is negative, it is indicated as affected.

Step 6: Finding the weights. Using Equation (6) and Equation (7), the weight of each criterion is calculated.

$$w_i = \left[\left(D_i + R_i \right) + \left(D_i - R_i \right) \right]^{1/2}, \ \forall \ i > 0, \ i \in R \tag{6}$$

$$W_i = \frac{w_i}{\sum_{i=1}^{n} w_i}, \ \forall \ n > 0, \ n \in R \tag{7}$$

Step 7. Set threshold value and obtain the Network Relation Map by using Equation (8). N is the elements's total number in matrix T. (Chiu et al. 2006, Liou et al. 2007).

$$\alpha = \frac{\sum_{i=1}^{n} \sum_{j=1}^{n} \left[t_{ij} \right]}{N} \tag{8}$$

Step 8: Impact directional scatter graph is drawn. Criteria above the threshold are determined as affecting. The situation that any criterion affects itself is also shown in the diagram.

5. An Application

In this study, according to the CIF (Cost, Insurance & Freight Prepaid) agreement, the importance levels of the risks and risks in the DEMATEL method during the marine logistics operation are determined by the decision makers.

The risks identified are given within the scope of the category in Table 3. Risk criteria were evaluated and determined by expert decision-makers working in the logistics sector. In the study, the risks were identified as the dangers that would delay, cancel and endanger the maritime logistics operation.

Risk criteria were evaluated by 5 expert decision-makers working in the logistics sector using the binary comparison scale given in Table 2.

Table 3 Risks in the sea logistics operation.

Classification	Code	Risks Definition
Reservation	R_1	Risk of not being able to find a place in the booking process
	R_2	Risk of not being able to find empty containers after booking confirmed
Internal Transport	R_3	Risk of not being able to find a vehicle after the empty container is provided
	R_4	Risk of being held at the loading dock after the vehicle and empty container are taken
	R_5	Risk of not being able to enter the port if the factory has not received a shipment at the exit
	R_6	Risk of not being able to land in port from heavy tonnage if overloaded

Clearance	R_7	Risk of not being able to load it on board if it doesn't finish customs clearance by cut off
Loading Port	R_8	Risk of a back-up if it enters the port early
	R_9	Risk of not having scales and VGM
	R_{10}	At the port, the loaded container risks not being able to load the ship for any reason while waiting for its ship (the ship may be shifted, there may be a tonnage problem on board, or it may be shifted by the agent to the next ship)
Ship's departure	R_{11}	Risk of transferring or dropping the container at the port and subsequent delay of the cargo after the ship leaves the port
Documentation	R_{12}	Risk of documentation (Once loaded onto the ship, there may be problems with document tracking or problems with documents)

The direct relationship matrix between the criteria indicating the risk importance levels for the 1st decision-maker is given in Table 4.

Table 4 1st direct relationship matrix of the decision maker

	R_1	R_2	R_3	R_4	R_5	R_6	R_7	R_8	R_9	R_{10}	R_{11}	R_{12}
R_1	0	0	0	0	0	0	0	0	0	1	2	0
R_2	4	0	4	0	0	0	0	0	0	0	0	0
R_3	3	4	0	0	0	0	0	0	0	0	0	0
R_4	2	4	4	0	1	0	0	0	0	0	0	0
R_5	0	2	2	3	0	0	0	0	0	1	0	0
R_6	0	2	2	1	0	0	0	0	0	1	2	0
R_7	3	3	3	4	4	4	0	0	2	1	0	3
R_8	2	2	2	0	0	0	0	0	0	0	0	0
R_9	2	2	2	3	3	4	3	0	0	1	2	2
R_{10}	1	0	0	1	2	3	3	0	0	0	2	3
R_{11}	2	0	0	0	0	0	0	0	2	2	0	4
R_{12}	0	0	0	0	0	0	0	0	2	4	4	0

The direct relationship matrix between the criteria indicating the risk importance levels for the 2nd decision-maker is given in Table 5.

Table 5 2nd direct relationship matrix of the decision maker

	R_1	R_2	R_3	R_4	R_5	R_6	R_7	R_8	R_9	R_{10}	R_{11}	R_{12}
R_1	0	0	0	0	0	0	1	0	2	1	0	0
R_2	0	0	0	0	0	0	1	0	1	1	0	0
R_3	0	0	0	0	0	0	0	0	0	0	0	0
R_4	0	0	0	0	0	0	2	0	0	0	0	3
R_5	0	0	0	0	0	0	0	0	0	0	0	3
R_6	0	0	0	0	0	0	2	0	0	0	0	1

R_7	0	2	2	2	3	0	0	0	2	2	0	3
R_8	0	0	0	0	0	0	0	0	0	0	0	0
R_9	0	0	0	0	2	0	0	0	0	1	0	0
R_{10}	0	0	0	0	3	3	2	0	3	0	0	3
R_{11}	0	0	0	0	0	3	0	0	2	0	0	0
R_{12}	0	0	0	0	3	2	1	0	2	0	1	0

The direct relationship matrix between the criteria indicating the risk importance levels for the 3rd decision-maker is given in Table 6.

Table 6 3rd direct relationship matrix of the decision maker

	R_1	R_2	R_3	R_4	R_5	R_6	R_7	R_8	R_9	R_{10}	R_{11}	R_{12}
R_1	0	0	0	0	0	0	0	0	0	0	0	0
R_2	4	0	0	0	0	0	0	0	0	0	0	0
R_3	4	1	0	0	0	0	0	0	0	0	0	0
R_4	4	4	3	0	0	0	0	0	3	0	0	4
R_5	0	0	0	0	0	0	0	0	0	0	0	0
R_6	0	0	0	0	0	0	0	0	3	0	0	0
R_7	4	0	3	3	3	3	0	0	3	0	0	3
R_8	0	0	0	0	0	0	0	0	0	0	0	0
R_9	0	0	0	0	0	0	0	0	0	0	0	0
R_{10}	0	0	0	0	0	3	4	0	0	0	0	3
R_{11}	0	0	0	0	0	2	0	0	0	0	0	3
R_{12}	0	0	0	0	0	0	0	0	0	0	0	0

The direct relationship matrix between the criteria indicating the risk importance levels for the 4th decision-maker is given in Table 7.

Table 7 4th direct relationship matrix of the decision maker

	R_1	R_2	R_3	R_4	R_5	R_6	R_7	R_8	R_9	R_{10}	R_{11}	R_{12}
R_1	0	0	0	0	0	0	0	0	0	0	0	0
R_2	4	0	0	0	0	0	0	0	0	0	0	0
R_3	4	3	0	0	0	0	0	0	0	0	0	0
R_4	4	3	3	0	0	0	0	0	0	0	0	0
R_5	4	3	3	4	0	0	0	0	0	0	0	0
R_6	4	3	3	4	4	0	0	0	4	0	0	0
R_7	4	3	3	4	4	4	0	0	4	3	0	0
R_8	4	3	3	0	1	3	0	0	0	4	0	0
R_9	4	3	3	4	1	3	1	1	0	1	0	0
R_{10}	4	1	3	1	0	1	3	0	3	0	0	0
R_{11}	4	0	0	0	0	0	1	0	0	3	0	0
R_{12}	1	1	1	0	0	0	0	0	0	0	1	0

The direct relationship matrix between the criteria indicating the risk importance levels for the 5th decision-maker is given in Table 8.

Table 8 5th direct relationship matrix of the decision maker

	R_1	R_2	R_3	R_4	R_5	R_6	R_7	R_8	R_9	R_{10}	R_{11}	R_{12}
R_1	0	3	3	1	0	0	0	0	0	0	0	3
R_2	4	0	3	1	0	0	0	0	0	0	0	0
R_3	4	3	0	1	0	0	0	0	0	0	0	0
R_4	4	2	3	0	0	0	0	0	0	0	0	0
R_5	4	3	4	3	0	0	3	2	3	0	0	3
R_6	4	3	4	4	4	0	3	3	3	3	0	3
R_7	3	3	3	4	3	3	0	3	3	3	0	3
R_8	3	3	2	3	3	3	3	0	3	3	0	3
R_9	3	3	2	3	3	3	3	3	0	3	3	3
R_{10}	3	3	3	3	3	3	3	3	3	0	3	3
R_{11}	3	3	3	3	3	3	3	3	3	3	0	3
R_{12}	3	3	4	4	3	3	3	3	3	3	4	0

As a result of the evaluations of the decision-makers, the Direct Relationship Matrix (X) given in Table 9 is acquired. The Direct Relationship Matrix (X) obtained was calculated with the arithmetic average by means of Equation (1) with the scores given by the decision-makers.

Table 9 Direct relationship matrix (X)

	R_1	R_2	R_3	R_4	R_5	R_6	R_7	R_8	R_9	R_{10}	R_{11}	R_{12}
R_1	0,00	0,60	0,60	0,20	0,00	0,00	0,20	0,00	0,40	0,40	0,40	0,60
R_2	3,20	0,00	1,40	0,20	0,00	0,00	0,20	0,00	0,20	0,20	0,00	0,00
R_3	3,00	2,20	0,00	0,20	0,00	0,00	0,00	0,00	0,00	0,00	0,00	0,00
R_4	2,80	2,60	2,60	0,00	0,20	0,00	0,40	0,00	0,60	0,00	0,00	1,40
R_5	1,60	1,60	1,80	2,00	0,00	0,00	0,60	0,40	0,60	0,20	0,00	1,20
R_6	1,60	1,60	1,80	1,80	1,60	0,00	1,00	0,60	2,00	0,80	0,40	0,80
R_7	2,80	2,20	2,80	3,40	3,40	2,80	0,00	0,60	2,80	1,80	0,00	2,40
R_8	1,80	1,60	1,40	0,60	0,80	1,20	0,60	0,00	0,60	1,40	0,00	0,60
R_9	1,80	1,60	1,40	2,00	1,80	2,00	1,40	0,80	0,00	1,20	1,00	1,00
R_{10}	1,60	0,80	1,20	1,00	1,60	2,60	3,00	0,60	1,80	0,00	1,00	2,40
R_{11}	1,80	0,60	0,60	0,60	0,60	1,60	0,80	0,60	1,40	1,60	0,00	2,00
R_{12}	0,80	0,80	1,00	0,80	1,20	1,00	0,80	0,60	1,40	1,40	2,00	0,00

The value of r is calculated by means of Equation (4) by using the value of the totals of the rows and columns of the Direct Relationship Matrix (X). Then, by using these r value and Direct Relationship Matrix (X) values, the Normalized Direct Relationship Matrix (T) is acquired by means of Equation (3) in Table 10.

Table 10 Normalized direct relationship matrix (T)

	R_1	R_2	R_3	R_4	R_5	R_6	R_7	R_8	R_9	R_{10}	R_{11}	R_{12}
R_1	0,00	0,02	0,02	0,01	0,00	0,00	0,01	0,00	0,02	0,02	0,02	0,02
R_2	0,13	0,00	0,06	0,01	0,00	0,00	0,01	0,00	0,01	0,01	0,00	0,00
R_3	0,12	0,09	0,00	0,01	0,00	0,00	0,00	0,00	0,00	0,00	0,00	0,00
R_4	0,11	0,10	0,10	0,00	0,01	0,00	0,02	0,00	0,02	0,00	0,00	0,06
R_5	0,06	0,06	0,07	0,08	0,00	0,00	0,02	0,02	0,02	0,01	0,00	0,05
R_6	0,06	0,06	0,07	0,07	0,06	0,00	0,04	0,02	0,08	0,03	0,02	0,03
R_7	0,11	0,09	0,11	0,14	0,14	0,11	0,00	0,02	0,11	0,07	0,00	0,10
R_8	0,07	0,06	0,06	0,02	0,03	0,05	0,02	0,00	0,02	0,06	0,00	0,02
R_9	0,07	0,06	0,06	0,08	0,07	0,08	0,06	0,03	0,00	0,05	0,04	0,04
R_{10}	0,06	0,03	0,05	0,04	0,06	0,10	0,12	0,02	0,07	0,00	0,04	0,10
R_{11}	0,07	0,02	0,02	0,02	0,02	0,06	0,03	0,02	0,06	0,06	0,00	0,08
R_{12}	0,03	0,03	0,04	0,03	0,05	0,04	0,03	0,02	0,06	0,06	0,08	0,00

By means of Equation (5), the Normalized Direct Relationship Matrix (T) is subtracted from the Unit Matrix (I) and the obtained result is multiplied by the Normalized Direct Relationship Matrix (T), and the Total Relationship Matrix (F) is obtained in Table 11. Highlighted value was compared Equation (8) in order to define cause-effect relationship in Table 11.

Table 11 Total relationship matrix (F)

	R_1	R_2	R_3	R_4	R_5	R_6	R_7	R_8	R_9	R_{10}	R_{11}	R_{12}
R_1	0,02	0,04	0,04	0,02	0,01	0,01	0,02	0,00	0,02	0,02	0,02	0,03
R_2	0,14	0,01	0,07	0,01	0,00	0,00	0,01	0,00	0,01	0,01	0,00	0,01
R_3	0,14	0,09	0,01	0,01	0,00	0,00	0,00	0,00	0,00	0,00	0,00	0,01
R_4	0,16	0,13	0,13	0,02	0,02	0,01	0,03	0,00	0,04	0,01	0,01	0,07
R_5	0,11	0,10	0,10	0,10	0,01	0,01	0,04	0,02	0,04	0,02	0,01	0,07
R_6	0,14	0,12	0,12	0,11	0,09	0,03	0,06	0,03	0,11	0,05	0,03	0,07
R_7	0,24	0,18	0,20	0,20	0,18	0,15	0,05	0,04	0,16	0,11	0,03	0,15
R_8	0,13	0,10	0,09	0,05	0,05	0,07	0,04	0,01	0,05	0,07	0,01	0,05
R_9	0,16	0,12	0,12	0,12	0,11	0,11	0,08	0,04	0,04	0,07	0,06	0,08
R_{10}	0,16	0,11	0,12	0,10	0,12	0,15	0,15	0,04	0,13	0,04	0,06	0,15
R_{11}	0,13	0,07	0,07	0,06	0,06	0,09	0,06	0,04	0,09	0,09	0,02	0,11
R_{12}	0,10	0,08	0,09	0,07	0,08	0,07	0,06	0,04	0,09	0,08	0,09	0,04

After obtaining the Total Relationship Matrix (F), D_i, R_i, D_i+R_i and D_i-R_i are calculated and shown in *Table 12*. Criteria weights were found and criteria were sorted according to priority degree.

Table 12 Criteria weights and sorted priority degree

	D	*R*	*D+R*	*D-R*	*W*	*W*	*Rank*	*Identify*
R_1	0,24	1,62	1,86	-1,38	2,32	0,11	2	Effect
R_2	0,30	1,14	1,45	-0,84	1,67	0,08	8	Effect
R_3	0,28	1,16	1,43	-0,88	1,68	0,08	7	Effect
R_4	0,62	0,86	1,48	-0,24	1,50	0,07	9	Effect
R_5	0,64	0,73	1,37	-0,10	1,37	0,07	10	Effect
R_6	0,96	0,71	1,67	0,25	1,68	0,08	6	Cause
R_7	1,68	0,60	2,28	1,08	2,53	0,12	1	Cause
R_8	0,72	0,28	1,00	0,44	1,09	0,05	12	Cause
R_9	1,12	0,78	1,90	0,33	1,93	0,09	4	Cause
R_{10}	1,33	0,59	1,91	0,74	2,05	0,10	3	Cause
R_{11}	0,90	0,35	1,25	0,55	1,36	0,07	11	Cause
R_{12}	0,87	0,82	1,69	0,05	1,69	0,08	5	Cause

The cause-and-effect diagram of the criteria is drawn at the last stage of the DEMATEL method and presented in Figure 1.

Figure 1 Diagram of the1 cause and effect of the criteria

The risk group in the logistics activities of the DEMATEL method is shown in Figure 2.

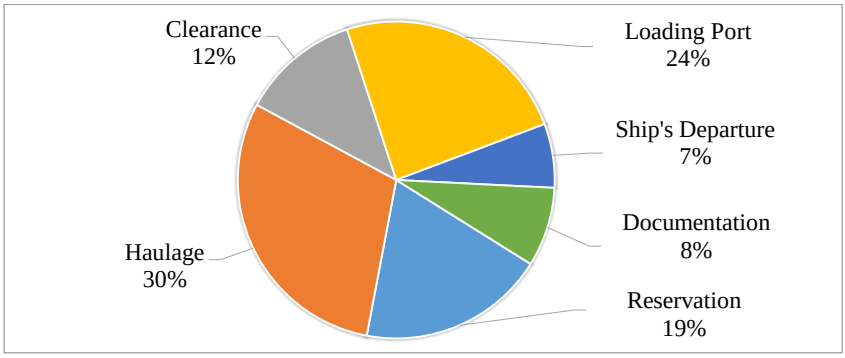

Figure 2 Distribution of risk groups of criteria.

DEMATEL analysis results in the adjustment:

- The most important 3 risk rankings in logistics risks are R_7 (Risk of not being able to load it on board if it doesn't finish customs clearance by cut off) at the rate of 12%, R1 (Risk of not being able to find a place in the booking process) at the rate of 11% and R_{10} (At the port, the loaded container risks not being able to load the ship for any reason while waiting for its ship (the ship may be shifted, there may be a tonnage problem on board, or it may be shifted by the agent to the next ship)) at the rate of 10%. The three most unimportant risk rankings in logistics risks are; R_8 (Risk of a back-up if it enters the port early) at the rate of 5%, R_{11} (Risk of transferring or dropping the container at the port and subsequent delay of the cargo after the ship leaves the port) at 7% and R_5 (Risk of not being able to enter the port if the factory has not received a shipment at the exit) at 7%.
- The importance level ratios of the risk groups in logistics activities are 30% internal transport risks, 24% loading port risks, 19% reservation risks, 12% customs clearance risks, 8% documentation risks, and 7% ship departure risks.
- According to the cause-and-effect diagram of the risks from logistics activities, the affecting risks are R_6, R_7, R_8, R_9, R_{10}, R_{11}, and R_{12}, and the affected risks are; R_1, R_2, R_3, R_4, and R_5. The most affecting risk is R_7 and the most affected risk is R_1.

6. Conclusion

The borders in trade have also widened, parallel to technological developments. In this context, transportation is an important link in the entire supply chain process; the undeniable majority of freight transportation is done by maritime transportation. Shipping involves a serious logistics process. Therefore, in the study; the risks that may occur

during the CIF maritime logistics process, which the seller frequently chooses in maritime transportation, were determined and the importance of the risks and the level of impact on each other were determined. In order to achieve this goal, analyzes were made with the DEMATEL method, and expert opinions were used to determine the risks and their importance. While there are many studies on risk management in the literature, this study contributed to the application area of the literature.

The weights of the risks considered were listed between 5% and 12% in the study. The highest risk was found to be R_7 (Risk of not being able to load it on board if it doesn't finish customs clearance by cut off) with 12%. The least important risk in logistics risks; it is R_8 (Risk of a back-up if it enters the port early) with a rate of 5%. Ratios of importance level of risk groups in logistics activities; internal transport risks have a share of 30%; ship departure risks have the lowest share with 7%. According to the cause-and-effect diagram of the risks arising from logistics activities; the risk most impacting is R7 (Risk of not being able to load it on board if it doesn't finish customs clearance by cut off) and the risk most impacted is R_1 (Risk of not being able to find a place in the booking process).

It was ensured that the risks in the operation processes of the logistics enterprises were determined, their importance levels were listed and their relations with each other were evaluated with the proposed model. In future studies, similar approaches can be applied to different application areas, other operations or other processes of logistics enterprises.

References

Aksakal, E., and Dağdeviren, M., ANP ve DEMATEL Yöntemleri ile Personel Seçimi Problemine Bütünleşik Bir Yaklaşım, Gazi Üniversitesi Mühendislik Mimarlık Fakültesi Dergisi, Cilt. 25, No. 4, (2010), ss. 905-913.

Chiu, Y. J., Chen, H. C., Tzeng, G. H., and Shyu, J. Z., Marketing strategy based on customer behaviour for the LCD-TV, International Journal and Decision Making, Vol. 7 No. 2/3 (2006), pp. 143–165.

Du, S., Li, H., and Sun, B., Hybrid Kano-fuzzy-DEMATEL model based risk factor evaluation and ranking of cross-border e-commerce SMEs with customer requirement, Journal of Intelligent & Fuzzy Systems, Vol. 37 No.6 (2019), pp. 8299-8315.

Faghih-Roohi S., Akcay A., Zhang Y., Shekarian E., and Jong E., A group risk assessment approach for the selection of pharmaceutical product shipping lanes, International Journal Production Economics, Vol. 229 (November 2020) 107774.

Freydman, O., The role of risk management of the logistic processes in economic development of the region, Studies of the Industrial Geography Commission of the Polish Geographical Society, No. 18 (2011), pp. 139-147.

Ganguly K. K., and Kumar G., Supply chain risk assessment: A fuzzy AHP approach, Operations and Supply Chain Management, Vol. 12 No. 1 (2019), pp. 1 – 13.

Govindan K. and Chaudhuri A., Interrelationships of risks faced by third party logistics service providers: A DEMATEL based approach, Transportation Research Part E Vol. 90 (2016), pp. 177–195.

Grant, D. B., and Elliott, M., A proposed interdisciplinary framework for the environmental management of water and air-borne emissions in maritime logistics, Ocean & coastal management, Vol. 163 (2018), pp. 162-172.

Habegger B., Risk analysis and management in a dynamic risk landscape, International Handbook on Risk Analysis and Management Professional Experiences Edited by Beat Habegger, (2008), pp. 13-32, ISBN 3-905696-18-5.

Huang, C.Y., Shyu, J.Z.,and Tzeng, G.H., Reconfiguring the innovation policy portfolios for Taiwan's SIP Mall industry, Technovation, Vol. 27 No. 12 (2007), pp. 744–765.

ICC., Incoterms 2020, by The International Chamber of Commerce, (2019), ISBN: 978-92-842-0511-0.

ISO, BS ISO 31000:2018 BSI standards publication risk management — Guidelines, Second edition (2018) Reference number ISO 31000:2018(E)

Kalogeraki E.M., Papastergiou S., Mouratidis H., and Polemi N. A., Novel risk assessment methodology for SCADA maritime logistics environments, Applied Sciences (2018), 8, 1477.

Karaoğlan S., DEMATEL ve VIKOR Yöntemleriyle Dış Kaynak Seçimi: Otel İşletmesi Örneği. Akademik Bakış Uluslararası Hakemli Sosyal Bilimler Dergisi, Sayı.55 (Mayıs Haziran 2016), ss. 9-24.

Laudares A.C., Ricco M.F.F., and Santos R.A.S., When does it end? Monte Carlo simulation applied to risk management indefense logistics' procurement processes, Brazilian Journal of Operations ve Production Management, Vol.16 No. 1 (2019), pp. 149-156.

Li, R. J., Fuzzy method in group decision making, Computers and Mathematics with Applications, Vol. 38 No.1 (1999), pp. 91–101.

Liou, J. H., Yen, L., and Tzeng, G. H., Building an effective safety management system for airlines, Journal of Air Transport Management, Vol.14, No.1 (2008), pp. 20-26.

Liou, J.H., Tzeng, H.G., and Chang, H.C., Airline safety measurement using a Novel Hybrid Model, Journal of Air Transport Management, Vol. 13 No. 4 (2007), pp. 243-249.

Liu, J., Zhou, H., and Sun, H., A three-dimensional risk management model of port logistics for hazardous goods, Maritime Policy & Management, Vol. 46, No.6 (2019), pp. 715-734.

Mokhtari, K., and Ren, J., A risk management methodology for maritime logistics and supply chain applications, Ocean Systems Engineering, Vol. 4 No. 2 (2014), pp. 137-150.

Nam, H. S., and Song, D. W., Defining maritime logistics hub and its implication for container port, Maritime Policy & Management, Vol. 38 No. 3 (2011), pp. 269-292.

Nguyen S., A risk assessment model with systematical uncertainty treatment for container shipping operations, Maritime Policy & Management, Vol. 47 No. 6 (2020), pp. 778-796.

Nikolov, B., and Tcholakova, V., Aspects of risk management in logistics activities of enterprises, application of fault tree analysis (fta). Innovations, Vol. 3 No. 2 (2015), pp. 34-38.

Papastergiou, S., and Polemi, D., Securing maritime logistics and supply chain: the medusa and MITIGATE approaches, Maritime Interdiction Operation Journal, No.14 (2017), pp. 42-48.

Radhika, D., The role of knowledge management as an innovative strategy in maritime logistics management, International Journal of Humanities Social Sciences and Education, Vol.1 No. 9 (2014), pp. 52-57.

Rahman M. S., Khan F., Shaikh A., Ahmed S. and Imtiaz S., A conditional dependence-based marine logistics support risk model, Reliability Engineering & System Safety Vol. 193, (January 2020), 106623.

Roh S., Tam J., Lee S.W., and Seo Y. J., Risk assessment of maritime supply chain security in ports and waterways, International Journal of Supply Chain Management, Vol. 7, No. 6 (2018),pp. 300-307.

Seredyuk V., Incoterms in practice: hidden risks case study Glaston. Bachelor's thesis,Tampere University of Applied Sciences Degree Programme in International Business School of Business and Services, (Autumn 2017).

Seyed-Hosseini, S. M., Safaei, N., and Asgharpour, M. J., (2006). Reprioritization of failures in a system failure mode and effects analysis by decision making trial and evaluation laboratory technique eliability. Engineering and System Safety, Vol. 91 No. 8 (2006), pp. 872–881.

Tzeng, G. H., and Huang, J. J., Multiple Attribute Decision Making Methods and Applications. Boca Raton (USA): CRC Press, (2011) 159.

Tzeng, G. H., Chiang, C. H., and Li, C. W., Evaluating intertwined effects in e-learning programs: A novel hybrid MCDM model based on factor analysis and DEMATEL, Expert Systems with Applications, Vol.32 No. 4 (2007), pp. 1028–1044.

UNCTAD, Review of Maritime Transport 2020, (2020), New York: United Nations Publications. ISBN 978-92-1-112993-9.

Vilkoa J., Ritalaa P., and Hallikasa J., Risk management abilities in multimodal maritime supply chains: Visibility and control perspectives. Accident Analysis and Prevention, Vol. 123 (2019), pp. 469–481.

Wu, W. W., and Lee, Y.T., Developing global managers' competencies using the fuzzy DEMATEL method, Expert Systems with Applications, Vol. 32, No. 20 (2007), pp. 499-507.

Yin E., Chen Z., and Xiao Y., Risk perception affecting the performance of shipping companies: the moderating effect of China and Korea, Maritime Policy & Management, Vol. 46 No. 3 (2019), pp. 295-308.

Zimon D., and Madzík P., Standardized management systems and risk management in the supply chain, International Journal of Quality and Reliability Management Vol. 37 No. 2 (2020), pp. 305-327.